
HABILITATION THESIS

**HIERARCHICAL MODELING
OF MULTI-ION TRANSPORT THROUGH
POROUS MATERIALS**

HABILITATIONSSCHRIFT

**HIERARCHISCHES MODELLIEREN
VON IONENTRANSPORT DURCH
PORÖSE MATERIALIEN**

Vorgelegt zur Erlangung der Venia Legendi
im Fache "Kontinuumsmechanik und Biomechanik"

eingereicht an der Technischen Universität Wien
Fakultät für Bauingenieurwesen

von

Dipl.-Ing. Dr. techn. Peter Pivonka
2333 Leopoldsdorf, Niederösterreich, Österreich

Wien, im April 2007

Preface

This habilitation thesis comprises a series of papers in the field of hierarchical modeling applied to the description of transport phenomena through deformable porous materials including cement-based materials, geomaterials such as clayey soils, and biomaterials such as cartilage. This work has been made possible by gaining two very competitive scholarships. The first one is an “Erwin Schrödinger” fellowship granted from the Austrian Science Found in 2002, while the second one is an “Australian Postdoctoral (APD) Research Fellowship” granted by the Australian Research Council in 2004.

The Erwin Schrödinger scholarship has provided the basis for my stay in Australia. I first worked with Prof. H.B. Mühlhaus and the Exploration and Mining Group at the ARRC (CSIRO) in Perth. This CSIRO group is recognized as one of the top research institutions in Australia dealing with reactive transport processes through porous rocks and possessing excellent research infrastructure. After this stint, I joined Prof. David W. Smith and the Geomechanics Group at the University of Newcastle (NSW). The Geomechanics Group at the University of Newcastle is internationally recognized with several former group members now placed in prominent positions at various universities and industrial institutions. After this period, Prof. D.W. Smith was appointed as Head of the Department of Civil and Environmental Engineering at The University of Melbourne. Additionally, he was appointed to develop a new study program (Undergraduate and Postgraduate) of Biomedical Engineering at The University of Melbourne starting in 2004.

Prof. D.W. Smith invited me to join him in setting up this new undergraduate and postgraduate teaching program and to enter new research areas in Biomedical Engineering. Given the fact that The University of Melbourne is the leading research university in Australia and that Melbourne is the “hub” of Biomedical Science in Australia, and recognized world-wide, I used this fantastic opportunity to enter the field of Biomedical Engineering. With this challenging task of being involved with setting up a new Biomedical Engineering program, I gained knowledge on molecular biology, physiology, and mathematical biology.

In the following, I would like to mention two people who contributed in various ways to my research in the last five years. First I would like to mention Assoc. Prof. Christian Hellmich from the Institute for Mechanics of Materials and Structures (<http://www.imws.tuwien.ac.at/>, former Institute for Strength of Materials). Since our studies of Civil Engineering at Vienna University of Technology we both share a common interest in various scientific fields including mathematics, physics, mechanics, and biology. In many discussions during our time as students we already began to wonder if it would one day be possible to describe mechanical properties of materials such as stiffness, strength, and/or transport properties (including diffusion coefficients and permeabilities) from more fundamental quantities found at lower scales. What puzzled us most was the big gap between material science and continuum mechanics. Classical mechanics was then based solely on a macroscopic description using phenomenological equations. On the other hand, material scientists would look at inter-atomic forces and

arrangement of atoms to estimate energies etc. However, during our graduate studies mathematical tools now known as up-scaling or homogenization became available to introduce information from lower scales at higher levels (Zaoui 1997). More generally this approach is denoted as hierarchical- or multi-scale modeling approach (Cushman 1997).

Prof. C. Hellmich has gained detailed knowledge on this approach during his postdoctoral stay at M.I.T and he introduced me to some of his work on homogenization in 2002.

I first applied the homogenization approach to the description of chloride diffusion through cement pastes (Pivonka et al. 2004). Estimation of chloride diffusion through cement based materials is essential for durability assessment of concrete structures. In this paper we demonstrated that the effective diffusion coefficient of cement pastes only depends on the pore morphology (expressed as a function of the tortuosity) which is related to the water/cement (w/c) ratio and the chloride diffusion coefficient in the pore solution. The latter was found to strongly depend on the pore water viscosity which in general is quite different from the viscosity of a pure aqueous solution. Another, important aspect related to the estimation of chloride diffusion coefficients is related to the applied experimental testing method. Currently, two methods are commonly employed. The first method applies a concentration gradient across a diffusion cell test, i.e. two compartments filled with a sodium chloride solution of different concentration separated by a cement paste sample in the range of mm to cm. Whereas the second method additionally applies an electric field in order to drive chloride ions through the specimen. Experimental testing times are quite different for these two methods. Whereas the first method requires several months to years to reach steady state conditions, the second method only takes several weeks. However, a still unresolved problem in cement and concrete research is that effective diffusion coefficients based on these two methods have a large variation. In a recent paper (Narsilio et al. 2007), I outline underlying theoretical assumptions for evaluation of migration tests and also discuss possible inconsistencies related to the experimental design such as background electrolyte concentration, pore solution composition and applied voltage gradients.

The second person who has been very influential in my research career is Professor David W. Smith from the Center of Biomedical Engineering at The University of Melbourne and current Associate Dean for Biomedical Engineering (<http://www.bme.unimelb.edu.au/about/index.html>). I met Prof. D.W. Smith during my Schrödinger Fellowship in Australia and he became a friend and mentor ever since. Working on reactive transport processes in porous media there was no way that one wouldn't come across the innovative work of Prof. D.W. Smith which is well known internationally in the geotechnical and geo-environmental research community. Apart from his activity in the geotechnical and geo-environmental sciences, David has a very strong interest in Medical science in which he did a Bachelor degree. One of his beliefs is that Engineers and in particular Biomedical Engineers have much to contribute to the medical field. Medical science up-to-day is solely based on experimental observations without applying a theory for interpretation of results and formulation of hypotheses. Given the complexity of biological systems it is very unlikely to gain a complete understanding of processes involved without applying a particular theory for testing of

hypotheses (Cassman et al. 2005). Physics and Engineering on the other hand, have a long standing tradition over centuries where experiments and theory were always developed hand in hand and mutually supported each other. Motivated by David's ideas I entered the exciting field of Biomedical Engineering four years ago. As one can imagine there is a very steep learning curve in order to become well versed in medical terminology. However, in order to establish close collaborations between medical scientist and (biomedical) engineers speaking the same language is essential for research collaborations and team formations. Over the last four years I entered many challenging areas in Biomedical Engineering including cartilage mechanics, bone signal transduction, bone remodeling, developmental biology, and modeling of signalling pathways related to cancer.

In the following, I will concentrate on the geo-environmental and cartilage mechanical aspects of my research as they are thematically most closely related. For both topics we apply both microscale and macroscale approaches. The common thread in both themes is the transport of solutes through a porous material. Whereas for cement based and clay materials solutes are generally denoted as contaminants and are a major concern for the designing engineer, in the field of cartilage mechanics solutes are commonly denoted as nutrients such as growth factors which nurture the cartilage cells embedded in the cartilage matrix and are a desired product. Depending on the stiffness of the porous material and the applied load the deformation of the material may be an important aspect in the transport process of solutes. Such materials are generally referred to as deformable porous materials.

From a detailed literature review on multi-ion transport through porous materials it became clear that a major part of this literature does not consider electrochemical interactions between charged solutes (i.e., ions). Solute are usually treated the same as uncharged species, together with consideration of various reaction terms in the diffusion equations (i.e., Fick's first and second law). However, fundamental physical chemistry clearly shows that ions are coupled by means of electrochemical forces (Helfferich 1962). In the case of a binary salt solution such as sodium chloride (NaCl) this leads to simultaneous diffusion of sodium and chloride ions (at the same speed) although the individual self-diffusion coefficients of these ions differ by almost a factor of two (Atkins and de Paula 2002). This electrochemical coupling leads to the development of an electric potential (i.e., diffusion potential) which accelerates the slower ion and slows down the faster ion. Another fact which further complicates multi-ion transport is that many materials (including clays and cartilage) contain surface charges on their particles which will interact with ions moving through the pore space leading to the formation of diffusive double layers (DDL). These interactions are well known from the colloidal science literature and give rise to so-called electrokinetic phenomena such as streaming potentials and electro-osmosis (Hunter 2002). However, treatment of these phenomena in colloidal science is mainly made using analytical equations which are strongly simplified in order to obtain closed form solutions (Evans and Wennerstroem 1999).

So our first major goal was to introduce these principles of colloidal science into the geo-environmental research literature. This was accomplished by fully coupling the Nernst-

Planck (NP) equations describing ion transport driven by electrochemical forces and the Poisson equation of electrostatics which couples the electric potential to the electric charges in the porous material – this equation system is commonly denoted as the PNP system of equations. We then applied these equations at the microscale to ion transport through platy clay soils and demonstrated numerically anion exclusion effects encountered in negatively charged materials (Smith et al. 2004). In particular, we could show for the first time numerically that cations and anions are taking different transport pathways in charged porous materials depending on the charges on particles. This phenomenon has been described previously only in a qualitative way (Sen 1989) (Revil 1999).

In a second paper I then extended the electro-diffusion equations by taking into account also advective transport of ions (Pivonka and Smith 2005). This so-called electrohydrodynamic transport of ions can be accurately described by coupling of an extended version of the Navier-Stokes equations with the Poisson equation of electrostatics. With the applied new theory we could calculate the power which is dissipated due to fluid viscosity and the power which is dissipated due to ions held in diffusive double layers, and so differentiate between these two phenomena. The fluid velocity profiles obtained for a charged porous slit clearly indicated that in the case of zero surface charge on the slit walls the well known parabolic curve was obtained. On the other hand, for high surface charges a transition of this parabolic curve to a flattened velocity profile was obtained.

After having gained insight into multi-ion transport on the microscale the next step in my research was the upscaling of the microscopic equations in order to obtain macroscopic transport equations and associated macroscopic transport coefficients. Most engineering applications deal with the investigation of ion transport behavior in the range of cm to m. For materials lying in this length scale, it is impossible to apply the microscopic PNP equations to the entire structure, as computer resources are insufficient to model this level of detail. Additionally, detailed information of ion concentration and voltage distribution obtained from the microscale governing equations are usually not needed for the entire structure. For these reasons macroscopic governing equations are commonly employed for materials in the above mentioned scale. However, macroscopic equations require the knowledge of macroscopic transport properties such as effective diffusion coefficients, effective conductivities, and effective permittivities of the material.

Macroscopic transport properties generally have to be estimated from experiments. The most commonly used method for investigating electro-diffusive ion transport through membranes and porous materials is the "diffusion cell test". In this experiment a (charged) porous material is clamped between two compartments containing different concentrations. For steady-state conditions one can measure the flux of solutes, ion concentration gradients, and the electric potential. Based on these measured quantities and the underlying macroscopic equations the respective transport quantities can be estimated.

There are various alternatives to describe diffusive transport of solutes through porous materials at the macroscale. Most often macroscopic governing equations are empirically derived. In this case they are referred to as 'phenomenological equations'. On the other hand, if the underlying behaviour of the system is understood at a deeper level, these

equations can be derived through a mathematical process known as up-scaling or homogenization. Commonly employed up-scaling schemes are ‘asymptotic expansion’ (Auriault and Lewandowska 1996) and ‘volume averaging’ (Bear and Bachmat 1991), (Zaoui 1997), (Whitaker 1999).

I first investigated the case of electrochemical equilibrium of an electrolyte solution and a charged porous material, which is a special case of the kinetic equations (Pivonka et al. 2007). Due to the surface charges on the material, the pore solution concentration of electrolyte is different from the outside solution, giving rise to an electric potential across the interface. This potential is commonly denoted as the ‘Donnan potential’ and the associated equilibrium as ‘Donnan equilibrium’ (Helfferich 1962). In this paper I derive generalized equilibrium equations (based on volume averaging), which link the electric potential with so-called *effective concentrations* (which turn out to be logarithmic volume averages of actual ion concentrations). The proposed theory also includes the classical equilibrium equations which are based on the assumption that particle charges are homogeneously distributed across the material and so represents a true generalization of classical phase equilibrium equations.

Having resolved the equilibrium problem I started with the much more elaborate kinetic case, i.e. electro-diffusion of ions. We had already published one conference paper on this topic (Pivonka et al. 2005) and just recently submitted a paper on the “Upscaling of the Poisson-Nernst-Planck system of equations”. It turns out that the macroscopic governing equations derived in this way differ significantly from classical macroscopic electro-diffusion equations. Again the derived equations are a generalization of the classical equations taking into account the non-homogeneous distribution of charge in porous material. We also demonstrated that effective diffusion coefficients in charged porous materials not only depend on the ion self-diffusion coefficient and tortuosity of the pore space, but also on the concentration of background electrolyte and surface charge on particles. The latter are expressed as a factor representing the ratio of effective to actual ion concentrations.

Parallel to the abovementioned models, which describe solute transport in porous materials without taking into account material deformations, I have also formulated coupled transport and deformation models at various scales. Deformation of porous materials can be caused by mechanical loading or by electrochemical effects such as for example the swelling of charged porous materials when saturated with an electrolyte solution (Mitchell and Soga 2005). Swelling is caused by repulsion of electric double layers which induces a pressure in the pore fluid commonly referred to as a ‘disjoining pressure’ which leads to expansion of the material (Grodzinsky 2000). Currently, our group works on both macroscale and microscale formulations which in the near future will be bridged in order to accurately estimate macroscopic material properties.

It has been postulated that soil deformations of contaminant barriers may be responsible for early breakthrough times of contaminants leading possibly to ground water contamination. We have formulated a sophisticated coupled large deformation contaminant transport model which allows us to investigate this hypothesis (submitted paper). This new model is a generalization of a large number of models found in the literature describing soil consolidation and contaminant transport (including the diffusion only model which is commonly used for clay liner design). In a recent study we showed

in what way commonly employed assumptions may influence the numerical results and could so identify conservative and non-conservative models. Additionally, we performed a comprehensive parametric study which indicated that a certain combination of soil and transport parameters are required in order to obtain the worst case scenario for contaminant break through (i.e., to minimize the breakthrough time of contaminants). Another research area related to contaminant transport is the development of remediation strategies. Here I was involved in a project developing a geochemical model for fluoride adsorption onto alumina (Fletcher et al. 2006). Combination of contaminant transport models and geochemical models provides a powerful tool for environmental design such as design of contaminant barrier systems.

Cartilage is a porous material, somewhat like clay soils, and so modeling strategies developed in one area may be productively applied in another. One key question in cartilage research (similar to the question in geo-environmental engineering about the design of engineered clay-barrier systems): “Can the deformation of cartilage enhance the transport of growth factors, which in turn leads to cartilage matrix biosynthesis?”

Articular cartilage is a complex tissue that covers the ends of long bones at freely movable joints (Grodzinsky 2000). In young animals, the tissue is glistening, smooth and intact, but in preclinical disease states, it looks dull and roughened. In osteoarthritis, the tissue frays and tears, eventually forming deep fissures, and in advanced osteoarthritis, the entire covering of cartilage may be lost and then bone scrapes painfully on bone. Due to the extraordinary complexity of the tissue, very little of what is currently known has translated into practical outcomes in terms of preventative advice or interventions, repair strategies for damaged tissues, or post-surgical patient management. Our research is concerned with developing mathematical models to describe how various molecules (e.g. tissue growth factors, oxygen) are transported into cartilage to keep it healthy, as well as how cartilage minimizes wear and friction (we are also developing a unique theory that explains McCutcheon’s weeping lubrication theory, and reconciles this theory with alternate theories).

There are no blood vessels in cartilage to transport nutrients and growth factors to chondrocytes (i.e., cartilage cells) dispersed throughout the cartilage matrix. Insulin-like growth factor-I (IGF-I) is a large molecule with an important role in cartilage growth and metabolism, however, it first must reach the chondrocytes to exert its effect. While diffusion of IGF-I through cartilage is possible, it has been speculated that cyclic loading may enhance the rate of solute transport within the cartilage. To better understand this process, we derive a coupled small deformation and solute transport model formulated in axisymmetric coordinates to examine transport of solutes through a cylindrical plug of cartilage undergoing cyclic deformation in the range of 10^{-3} -1 Hz (Gardiner et al. 2007). This study revealed the role of timescales in interpreting transport results in cartilage. We showed that dynamic strains can either enhance or inhibit IGF-I transport at small timescales (<20 min after onset of loading), depending on the loading frequency. However, on longer timescales it is found that dynamic loading has negligible effect on IGF-I transport. Most importantly, in all cases examined the steady state IGF-I concentration did not exceed the fixed boundary value, in contrast to previous predictions (Mauck et al. 2003).

The second paper on cartilage biology deals with reactive transport, i.e., the effects of solute binding on transport (which hasn't been taken into account appropriately in previous research). For this purpose we developed a reactive transport model (based on previous work of our group (Gardiner et al. 2007)) to describe the potential role of binding of solutes within cyclically deformed cartilage. Our results show that binding now does have a significant effect on transport, particularly for the low IGF-I concentrations typical for synovial fluid. A dynamic loading regime of high strain magnitudes (up to 10%) in combination with high frequencies (e.g. 1 Hz) was seen to produce the most dramatic results in enhanced total uptake ratio as high as 25% averaged over the first 5 h of cyclic loading.

P. Pivonka, Ch. Hellmich, and D. Smith. Microscopic effects on chloride diffusivity of cement pastes – a scale transition analysis. *Cement and Concrete Research*, **34** (12), pp 2251-2260, 2004.



Microscopic effects on chloride diffusivity of cement pastes—a scale-transition analysis

Peter Pivonka^{a,*}, Christian Hellmich^b, David Smith^a

^aDepartment of Civil and Environmental Engineering, School of Engineering, The University of Melbourne, Victoria 3010, Australia

^bInstitute for Strength of Materials, Vienna University of Technology, Karlsplatz, 13/202, A-1040 Vienna, Austria

Received 12 June 2003; accepted 2 April 2004

Abstract

For estimation of the durability of structures, it is highly desirable to quantify and simulate the chloride diffusion process in concrete. To this end, diffusion–cell experiments delivering the chloride diffusivity of cement pastes with different water–cement ratios (related to different microporosities) are evaluated in a scale-transition analysis. For prediction of the apparent chloride diffusivity, cement paste can be modelled by means of a differential homogenization scheme involving nondiffusive spherical inclusions in a diffusive matrix. As a result, chloride diffusivity of cement paste is obtained as a function of the microporosity and the chloride diffusivity in the micropore solution. Remarkably, the latter turns out to be one order of magnitude smaller than the chloride diffusivity in a pure salt solution system. The smaller diffusivity is probably caused by structuring of water molecules along the pore surface of cement paste.

© 2004 Elsevier Ltd. All rights reserved.

Keywords: Chloride diffusion; Cement paste; Molecular water structuring; Scale transition; Multispecies transport

1. Introduction

One of the most severe durability problems in civil engineering is the deterioration of reinforced concrete structures through corrosion of the reinforcing steel. This process is accelerated by the possible presence of chloride which may be transported from the concrete surfaces (where it typically occurs as part of sea water or deicing salts on bridges) to the reinforcing steel. Thereby, chloride can be transported either together with water through the micropore space, driven by differences in the pore water pressure (advective transport), or chloride can diffuse through the pore water, driven by differences in the chloride concentration. Herein, we focus on the second form of transport. For estimation of the durability of structures, it is highly desirable to quantify and simulate this diffusion process. However, the chloride diffusivity through concrete and cement paste is characterized by a large variation, which depends strongly on the water–cement ratio [1–5]. Explan-

ations for this large variation and its chemophysical origin are still a matter of debate. The possible significance of an electric (diffuse) double layer on the one hand [6–8], and of multispecies ionic transport on the other [9–11], have been discussed, but no commonly accepted view has been established so far.

In this paper, we want to contribute to an explanation for the variation and the magnitude of chloride diffusivity in cement pastes. We evaluate numerous experimental data from cell–diffusion tests published in the open literature [1–5,12,13], in the framework of a scale-transition analysis [14,15] between the micropore-space scale and the cement-paste scale.

2. Diffusion–cell experiments for determination of chloride diffusivity of cement pastes

Steady-state chloride diffusion through water-saturated concrete and cement pastes is usually described by Fick's first law [1–5,13,16], e.g., in the form [17]:

$$\mathbf{J}_{\text{paste}} = -\mathbf{D}_{\text{paste}} \cdot \nabla c_{\text{paste}}, \quad (1)$$

where $\mathbf{J}_{\text{paste}}$, $\mathbf{D}_{\text{paste}}$, and ∇c_{paste} are the molar flux, the second-order diffusivity tensor, and the concentration gra-

* Corresponding author. Tel.: +61-3-8344-4050; fax: +61-3-8344-4616.

E-mail addresses: Pivonka@civenv.unimelb.edu.au (P. Pivonka), Christian.Hellmich@tuwien.ac.at (C. Hellmich), David.Smith@unimelb.edu.au (D. Smith).

URL: <http://www.fest.tuwien.ac.at>.

dient of sodium chloride in cement paste. Cement paste can be considered as isotropic material, $\mathbf{D}_{\text{paste}} = \mathbf{1}D_{\text{paste}}$, with the diffusion coefficient D_{paste} , and the second-order unity tensor $\mathbf{1}$. D_{paste} is commonly determined by diffusion–cell tests, where two cells, filled with solutions characterized by different salt concentrations, are separated by a cylindrical cement-paste sample with cross-sectional area A_{sample} and thickness t_{sample} (Fig. 1a). The concentration in the upstream (source) compartment, $c_{\text{sol},1}$, is kept constant during the experiment. In addition, $c_{\text{sol},1}$ is chosen much larger than the salt concentration in the downstream (collector) compartment, $c_{\text{sol},2}$, i.e., $c_{\text{sol},1} \gg c_{\text{sol},2}$. At the beginning of the test (see Fig. 1b), $c_{\text{sol},2}$ is chosen to be virtually zero. The chloride ions need a certain time span to move into the downstream compartment. The end of this time span is indicated by an increase of $c_{\text{sol},2}$ in the downstream compartment (see Fig. 1b). Monitoring $c_{\text{sol},2}$ over time allows for estimation of the chloride flux,

$$J_{\text{paste}} = \frac{V_{\text{cell},2} \Delta c_{\text{paste},2}}{A_{\text{sample}} \Delta t} \quad (2)$$

where $V_{\text{cell},2}$ denotes the volume of the downstream cell. First, $\Delta c_{\text{sol},2}/\Delta t$ is changing (Fig. 1b), so that transient conditions prevail. The duration of transient conditions increases with increasing thickness of the specimen. Afterwards, steady-state conditions (i.e., $\Delta c_{\text{sol},2}/\Delta t = \text{const}$) are observed. They allow for estimation of the chloride diffusion coefficient, based on the discrete 1D specification of Fick’s first law for the diffusion–cell test,

$$J_{\text{paste}} = -D_{\text{paste}} \cdot \frac{\Delta c_{\text{paste}}}{\Delta x} = -D_{\text{paste}} \cdot \frac{c_{\text{paste},2} - c_{\text{paste},1}}{t_{\text{sample}}} \quad (3)$$

D_{paste} can be expressed from Eq. (3) and Eq. (2), in the form:

$$D_{\text{paste}} = \frac{V_{\text{cell},2} \Delta c_{\text{paste},2}}{A_{\text{sample}} \Delta t} \frac{t_{\text{sample}}}{c_{\text{paste},1} - c_{\text{paste},2}}. \quad (4)$$

The chloride concentrations adjacent to the circular surfaces of the cement-paste sample, $c_{\text{paste},i}$, $i = 1, 2$, can

Table 1

Curing conditions of cement paste diffusion experiments (P81 [1], Y91 [2], N95 [3], TN92 [4], Mc95 [5], ACP01 [51], C01 [12], H95 [13])

Number	Description of curing condition
i	Air curing at room temperature (90–100% relative humidity)
ii	Immersed in saturated Ca(OH) ₂ solution at room temperature
iii	Immersed in NaOH solution at room temperature
iv	Immersed in H ₂ O at room temperature

be determined from the chloride concentrations in the solutions of the upstream and the downstream cell, $c_{\text{sol},i}$, $i = 1, 2$, and from the microporosity ϕ of the cement-paste sample, through

$$c_{\text{paste},i} = \phi \cdot c_{\text{sol},i} \quad \text{with } i = 1, 2 \quad (5)$$

Insertion of Eq. (5) into Eq. (4) provides a relation for the determination of the diffusion coefficient of cement pastes from the physical properties accessible in diffusion–cell tests:

$$D_{\text{paste}} = \frac{V_{\text{cell},2} \Delta c_{\text{sol},2}}{A_{\text{sample}} \Delta t} \frac{t_{\text{sample}}}{c_{\text{sol},1} - c_{\text{sol},2}} \quad (6)$$

D_{paste} is commonly referred to as apparent (or cement paste) diffusion coefficient, or more properly, as mass transfer coefficient [17]. In the literature dealing with chloride diffusion through cement paste, this coefficient is also denoted as ‘effective diffusion coefficient’ of cement paste (see, e.g., Refs. [1,5,12]). However, in geo-environmental engineering, a distinction is made between the effective and the apparent diffusion coefficient (see Ref. [18] for details). In the following, to avoid any confusion, D_{paste} will be referred to as apparent diffusion coefficient of cement paste.

Diffusion–cell tests are typically performed to explore the effects of variations of (i) the water–cement ratio [1,5], (ii) the curing conditions [19,20], and (iii) the sodium chloride concentration [1,5] (Tables 1, 2, and 3 and Fig. 2).

Whereas the influence of different curing conditions and of the sodium chloride concentration turns out to be of

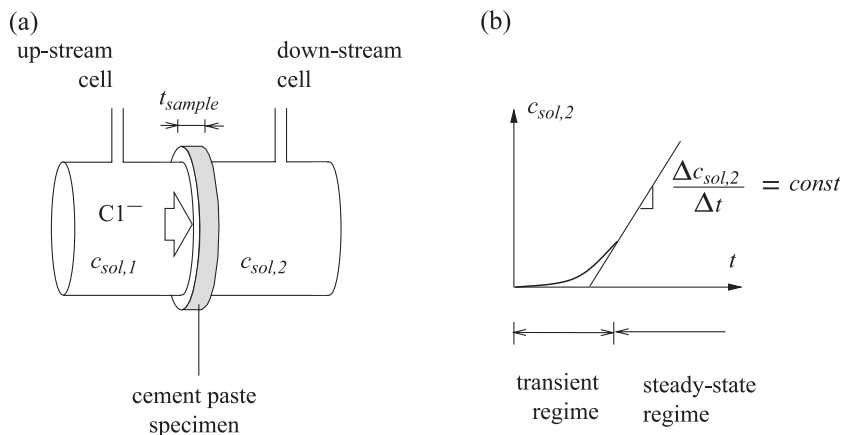


Fig. 1. Diffusion cell test: (a) schematical sketch; (b) time-dependent evolution of chloride concentration in downstream cell.

Table 2

Boundary conditions of cement-paste diffusion experiments (P81 [1], Y91 [2], N95 [3], TN92 [4], Mc95 [5], ACP01 [51], C01 [12], H95 [13])

Source	$c_{sol,1}$ [mol/l]	$c_{sol,2}$ [mol/l]	t_{cure} [days]	t_{test} [days]
P81	1 NaCl, Ca(OH) ₂	Ca(OH) ₂	60 ⁱ	21
Y91	1 NaCl, Ca(OH) ₂	Ca(OH) ₂	90–270 ⁱⁱ	21
N95	1 NaCl, 0.035 NaOH	0.035 NaOH	70 ^v	21
TN92	0.5 NaCl, Ca(OH) ₂	Ca(OH) ₂	90 ⁱⁱ	30
Mc95	0.5–4 NaCl	distilled H ₂ O	56 ⁱ	125
ACP01	1 NaCl, 0.035 NaOH	0.035 NaOH	84 ⁱⁱⁱ	
C01	1 NaCl, Ca(OH) ₂	Ca(OH) ₂	28 ^{iv} , 30 ⁱⁱ	21
H95	0.58 NaCl		60 ^{iv}	120

secondary importance, the strong functional dependence between water–cement ratio $(w/c)_i$ and apparent diffusion coefficient D_{paste} is striking (Fig. 2 and Table 3). The chemo-physical origin of this dependence will be elucidated next, by performance and interpretation of a scale-transition analysis.

3. Evaluation of experiments by a scale-transition analysis

Diffusive transport of chloride (see Table 4 for ionic diameters) in a porous medium typically takes place in the pores of the material. For cement paste, different characteristic pore sizes motivate the distinction between micropores (‘capillary pores’ and ‘air pores’) on the one hand, and nanopores (‘gel pores’) on the other (Table 4). The rather large ratio of micropore diameter to the diameter of the ions encountered in cement paste (see Table 4) allows for a

Table 3

Experimental determination of composition and diffusivity of cement pastes: $(w/c)_i$ =initial water–cement ratio (before curing), given in the literature; $(w/c)_c$ =water–cement ratio after curing, $(w/c)_c \geq 0.42$; ϕ =solution-saturated porosity of cement paste; D_{paste} =apparent diffusion coefficient

Source	$(w/c)_i$ given	$(w/c)_c$ given (≥ 0.42)	ϕ Eq. (17)	D_{paste} [10^{-12} m ² /s] given or Eq. (6)	
P81	0.40	0.42	0.065	2.600	
	0.50	0.50	0.157	4.470	
	0.60	0.60	0.249	12.35	
Y91	0.35	0.42	0.065	1.200	
	0.50	0.50	0.157	5.430	
	0.60	0.60	0.249	7.300	
N95	0.40	0.42	0.065	3.950	
	0.50	0.50	0.157	7.800	
	0.60	0.60	0.249	12.60	
	0.70	0.70	0.323	21.46	
TN92	0.40	0.42	0.065	2.900	
	0.60	0.60	0.249	9.400	
	0.80	0.80	0.384	21.00	
Mc95	0.40	0.42	0.065	2.353	2.549
	0.50	0.50	0.157	6.412	6.745
	0.60	0.60	0.249	12.29	12.57
	0.70	0.70	0.323	18.73	21.57
ACP01	0.35	0.42	0.065	0.40	
C01	0.40	0.42	0.065	3.646	
H95	0.55	0.55	0.206	11.25	

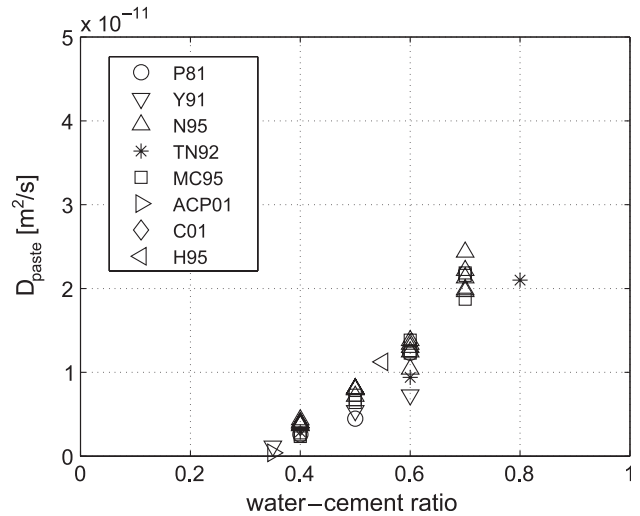


Fig. 2. Dependence of chloride diffusion coefficients of cement pastes D_{paste} on w/c ratio (P81 [1], Y91 [2], N95 [3], TN92 [4], Mc95 [5], ACP01 [51], C01 [12], H95 [13]).

continuum description of diffusive transport of chloride through the (saturated) pores. In cement paste, the diffusive transport of chloride ions takes place in the micropores [21] as long as they percolate, i.e., as long as they form a continuous pathway [22]. This is the common situation to which we refer herein. However, in case the micropores close off, diffusive transport of ions is accomplished through the much smaller nanopores [22].

We consider cement paste as a porous medium defined on a representative volume element (RVE) of some millimeters characteristic length ℓ (Fig. 3).

This medium consists of two phases, schematically indicated in Fig. 3, a sodium-chloride-solution-filled micropore space and a solid phase consisting of aluminosilicate hydrates. While the solid phase is regarded as nondiffusive ($D_{solid} \equiv 0$), we assign an average diffusion coefficient $D_{poresol}$ to the pore fluid containing sodium chloride, presuming at this point the validity of Fick’s first law in the micropore space

$$j_{poresol} = -D_{poresol} \nabla c_{poresol} \tag{7}$$

This equation holds at the length scale which is considerably smaller than that of the micropores, d in Fig. 3, and which is, at the same time, significantly larger than that of the

Table 4

Characteristic length scales of pores in cement paste and ions in solution

Pore type	ϕ Pores cement paste	Ion type	ϕ Ion unhydrated	ϕ Ion hydrated
Capillary	10 nm–100 μ m [53]	Na ⁺	2×102 pm [41]	2×250 –330 pm [45]
	<1 μ m [21]	K ⁺	2×138 pm [41]	2×180 –200 pm [45]
Gel	<10 nm [53]	Cl ⁻	2×181 pm [41]	2×200 pm [45]
	<2 nm [21]	OH ⁻	2×25 pm [41]	2×30 pm [45]
Air	<300 μ m [53]	H ₂ O	–	0.28 nm [41]

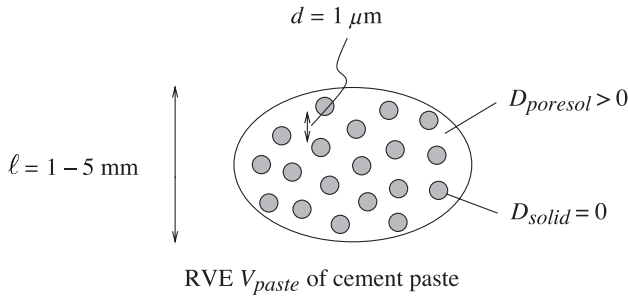


Fig. 3. Representation of cement paste as a two-phase material.

hydrated ions (see Table 4). At this scale, we are not aware of any measurement techniques for the estimation of $D_{poresol}$. As a first guess (the validity of which will be discussed later), $D_{poresol}$ may be assumed to match the sodium chloride diffusion coefficient of a pure solution system, i.e., $D_{poresol} = 1.61 \times 10^{-9} \text{ m}^2/\text{s}$ [23] (see also Tables 5 and 6).

A micro–macro transition law relating $D_{poresol}$ and D_{paste} is standardly given in the form [15,24] (pp. 1268, Eq. (9))

$$\mathbf{D}_{paste} = \phi D_{poresol} \mathbf{T}, \tag{8}$$

where $\phi = V_{pore}/V_{paste}$ is the microporosity of cement paste (V_{pore} is the volume of micropores in the RVE with volume V_{paste}); and the second-order ‘tortuosity tensor’ \mathbf{T} , capturing geometrical information about the pore shape and arrangement (pore morphology). Accounting for the isotropy of the material, $\mathbf{D}_{paste} = \mathbf{1}D_{paste}$, Eq. (8) can be recast in the simpler form

$$D_{paste} = \phi D_{poresol} T \tag{9}$$

with the (dimensionless) tortuosity factor T . Alternatively, a (dimensionless) pore space topology factor (formation factor) $\bar{F} = 1/(\phi T)$ is commonly introduced [25], resulting in a micro–macro transition law of the form

$$D_{paste} = \frac{D_{poresol}}{\bar{F}} \tag{10}$$

Without any further knowledge about the pore space except its porosity ϕ and its isotropic nature, the tortuosity tensor \mathbf{T} can be suitably estimated using the so-called differential scheme of continuum micromechanics [15,26,27]. Based on Eshelby’s matrix inclusion problem [28], an infinitesimal amount of solid spherical inclusions is introduced into a matrix with $D_{poresol}$. The solid–fluid mixture is homogenized into a material with a well-defined diffusivity. This material serves as the matrix for the next infinitesimal amount of solid inclusions. This procedure is

Table 5
Salt diffusion (1:1 electrolytes, i.e., $z_+ = +1$, $z_- = -1$) and self-diffusion coefficients (infinite dilute solution, according to Ref. [23])

Electrolyte	$D_{sol} [10^{-9} \text{ m}^2/\text{s}]$	$D_+ [10^{-9} \text{ m}^2/\text{s}]$	$D_- [10^{-9} \text{ m}^2/\text{s}]$
HCl	3.336	9.31	2.03
NaCl	1.610	1.33	2.03
KCl	1.994	1.96	2.03

Table 6
Salt diffusion coefficients at various concentrations at 25 °C (according to Ref. [23])

Concentration [mol/l]	$D_{sol} [10^{-9} \text{ m}^2/\text{s}]$		
	NaCl	KCl	HCl
0.05	1.507	1.864	3.07
0.1	1.483	1.844	3.05
0.2	1.475	1.838	3.06
0.5	1.474	1.850	3.18
1.0	1.484	1.892	3.43
1.5	1.495	1.943	3.74
3.0	1.565	2.112	4.65

repeated until the actual solid volume fraction $(1 - \phi)$ is reached, leading to the result [15]

$$\mathbf{T} = \phi^{1/2} \mathbf{1}, \tag{11}$$

$$\mathbf{D}_{paste} = \phi^{3/2} D_{poresol} \mathbf{1} \rightarrow D_{paste} = \phi^{3/2} D_{poresol} \tag{12}$$

Exactly the same result can be achieved by a differential effective medium approach for an assemblage of perfectly spherical grains [14], leading namely to $\bar{F} = \phi^{-3/2}$ in Eq. (10).

Having thus gained confidence in the relevance of the micro–macro transition law Eq. (12), we want to confront this relation to experimental data. This requires determination of the water-saturated microporosity ϕ from experiments.

Acker [29] has given the composition of cement pastes as a function of the water–cement ratio and the degree of hydration ξ (Fig. 4), reading as

$$\bar{V}_{cem}(\xi) = 1 - \xi \tag{13}$$

$$\bar{V}_{H_2O}(\xi) = \frac{\rho_{cem}}{\rho_{H_2O}} \langle w/c - 0.42\xi \rangle \tag{14}$$

$$\bar{V}_{hyd}(\xi) = \frac{\rho_{cem}}{\rho_{hyd}} \xi. \tag{15}$$

Here, $\langle \cdot \rangle$ represents the McAuley brackets, $\langle x \rangle = 1/(2(x + |x|))$. $\rho_{cem} = 3.15 \text{ kg}/\text{dm}^3$, $\rho_{H_2O} = 1.0 \text{ kg}/\text{dm}^3$, and $\rho_{hyd} =$

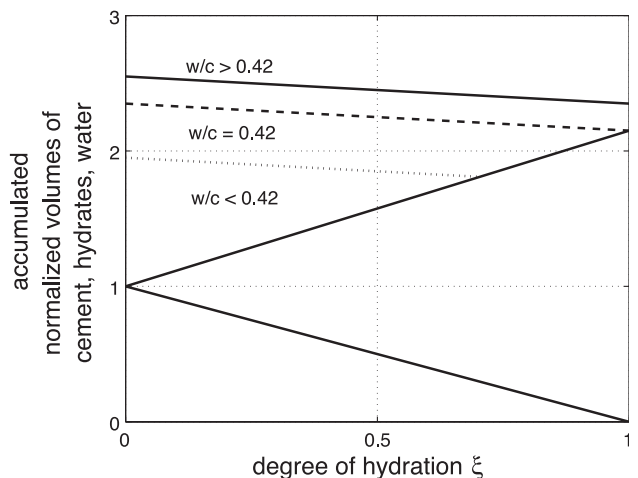


Fig. 4. Volumes of cement-paste components as a function of the degree of hydration, estimated according to Ref. [29].

1.46 kg/dm³ [29] are the real mass densities of cement, water, and hydrates. \bar{V}_i stands for the volume of component i normalized with respect to the volume of cement at $\xi=0$ (i.e., at the beginning of the hydration);

$$\bar{V}_i = V_i/V_{\text{cem}}(\xi = 0) \rightarrow \bar{V}_{\text{cem}}(\xi = 0) = 1 \quad (16)$$

(see also Fig. 4).

For $w/c < 0.42$, lack of water causes part of the cement to remain unhydrated ($\xi_\infty < 1$; see dotted line in Fig. 4). However, all considered pastes with initial water–cement ratio $(w/c)_i < 0.42$ (Fig. 4 and Table 2) were cured in water baths for at least 28 days (Table 2), so that they most probably attained a water–cement ratio of $(w/c)_c = 0.42$ during curing. The duration of the curing period of all considered pastes, ranging between 28 and 270 days (Table 2), also suggests a complete hydration of the pastes at the end of the curing time, $\xi_\infty = 1$. Furthermore, water curing implies the filling of all original air pores (occupying normalized volume \bar{V}_{air}) with water. This renders the volume fraction of the water-saturated micropores (or porosity ϕ) as the following function of the water–cement ratio:

$$\phi(w/c) = \frac{\bar{V}_{\text{air}}(\xi = 1, w/c \geq 0.42) + \bar{V}_{\text{H}_2\text{O}}(\xi = 1, w/c \geq 0.42)}{[\bar{V}_{\text{air}} + \bar{V}_{\text{H}_2\text{O}} + \bar{V}_{\text{hyd}} + \bar{V}_{\text{cem}}](\xi = 1, w/c \geq 0.42)}, \quad (17)$$

where we make use of the relationships Eqs. (13)–(15). Respective porosity values for the data base depicted in Fig. 2 range between 7% and 38% (Table 3).

Experimentally determined data pairs (ϕ, D_{paste}) (Table 3) are largely overestimated by the theoretical relationship Eq. (12) if $D_{\text{poresol}} = 1.61 \times 10^{-9} \text{ m}^2/\text{s}$ is assumed (see Fig. 5); that is, the simple guess of setting the pore solution

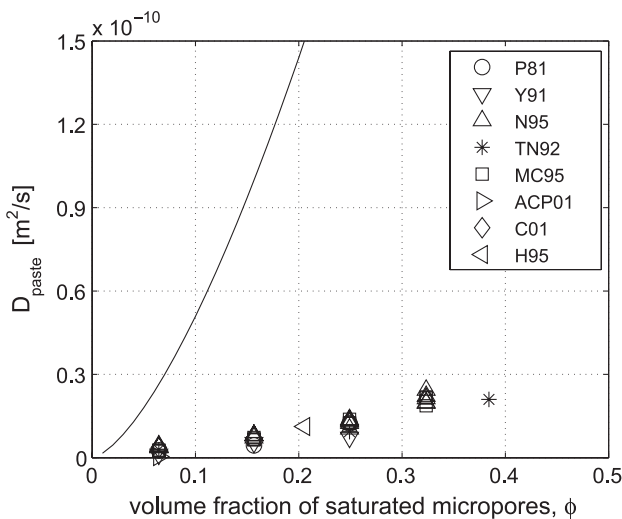


Fig. 5. Chloride diffusivity as a function of water-saturated porosity: comparison of experimental data (Table 3) and diffusion coefficients obtained by means of homogenization, Eq. (12) and $D_{\text{poresol}} = 1.61 \times 10^{-9} \text{ m}^2/\text{s}$.

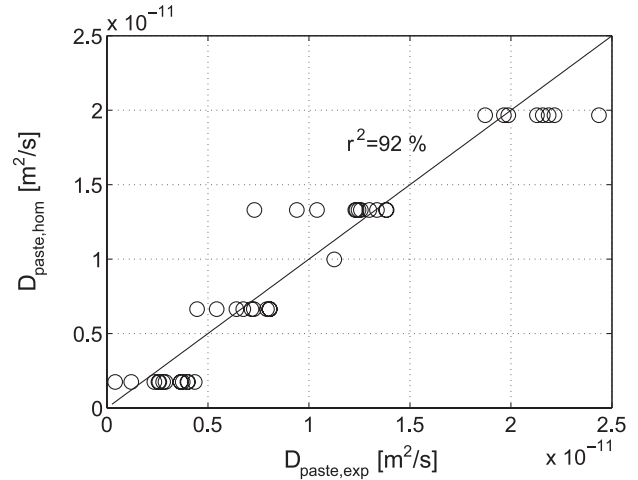


Fig. 6. Correlation of experimental data (Table 3) and diffusion coefficients obtained by means of homogenization, Eqs. (12) and (18).

diffusivity equal to the salt diffusivity in a pure solution system, $D_{\text{NaCl}} = 1.61 \times 10^{-9} \text{ m}^2/\text{s}$, turns out to be wrong.

However, what can also be seen is that the trend (shape) of the theoretical relationship fits very well with the one of the experiments. In fact, using a pore diffusion coefficient $D_{\text{poresol,opt}} = 1.07 \times 10^{-10} \text{ m}^2/\text{s}$, we get a high correlation coefficient of $r^2 = 0.92$ (Fig. 6), between D_{paste} and $D_{\text{paste,exp}}$. This is an extraordinary correlation given the simplicity of the micro–macro transition law and of the relation for the estimation of the water-saturated porosity Eq. (17). $D_{\text{poresol,opt}}$ was determined by minimizing the mean relative error between $n = 28$ experimental values $D_{\text{paste},i}$ (Table 3) and homogenization results $D_{\text{paste}}(\phi_i)$ from Eq. (12) (see Table 3 for the n values of ϕ_i)

$$\bar{e} = \frac{1}{n} \sum \frac{D_{\text{paste},i} - (\phi_i)^{3/2} D_{\text{poresol}}}{D_{\text{paste},i}} \rightarrow \text{Min} \Rightarrow D_{\text{poresol,opt}} \quad (18)$$

In other words, using this optimized diffusion coefficient to describe the diffusive transport in the pore solution of cement paste results in an excellent agreement between experimental data and values of the homogenized diffusion coefficients (see Fig. 7). It is noteworthy that models not formulated in the framework of micromechanics generally merge information on the pore morphology and on the transport properties into a single parameter (see, e.g., Refs. [30,31]). This parameter must then be repeatedly determined for different experiments, characterized by, e.g., different w/c values (porosity values) and different pore solution compositions. The choice of D_{poresol} for this parameter, i.e., substituting $\phi^{3/2}$ by ϕ in Eq. (12), implies assumption of straight transport pathways of ions through the pores. Respectively determined paste diffusivity may be classified as Voigt upper bounds. As a rule, they strongly overestimate experimentally obtained apparent diffusion coefficients.

The surprising result in Figs. 6 and 7 is that the various experimental data could be reproduced well using a single

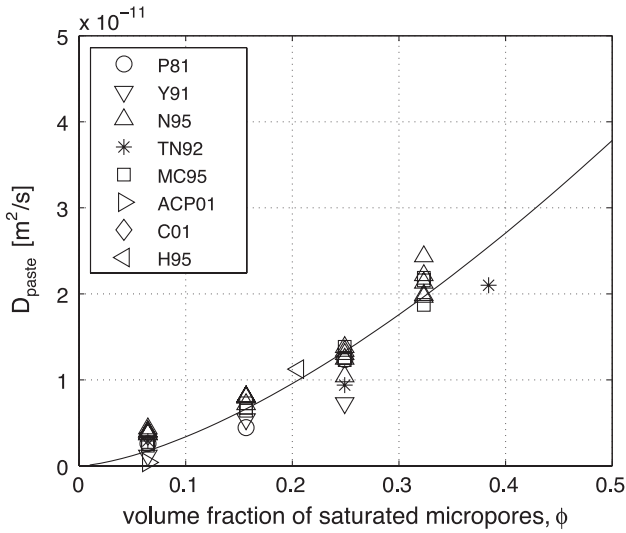


Fig. 7. Chloride diffusivity as a function of water-saturated porosity: comparison of experimental data (Table 3) and diffusion coefficients obtained by means of homogenization, Eqs. (12) and (18).

diffusion coefficient, i.e., $D_{\text{poresol,opt}}$ of the pore solution. The question now raised is, why the pore diffusion coefficient, $D_{\text{poresol,opt}}$, differs from the sodium chloride diffusion coefficient D_{NaCl} by a factor of 1/15. This question is addressed in the next section, but to this, some background understanding of multi-ion diffusion through a charged porous medium is first required.

4. Discussion of chloride diffusion in the micropore space of cement pastes

To suggest a reasonable explanation for the magnitude of the pore space diffusion coefficient $D_{\text{poresol,opt}}$ we determined previously, we have to precisely define the physical meaning of the diffusion coefficients D_{paste} (Eq. (1)) and D_{poresol} (Eq. (7)). For this reason, we give a short review of diffusive transport in pure liquids and charged porous media.

In a system consisting exclusively of a solution (pure solution system), four types of diffusion are commonly distinguished [18] (see Fig. 8): (i) self-diffusion, (ii) tracer diffusion, (iii) salt diffusion, and (iv) counterdiffusion.

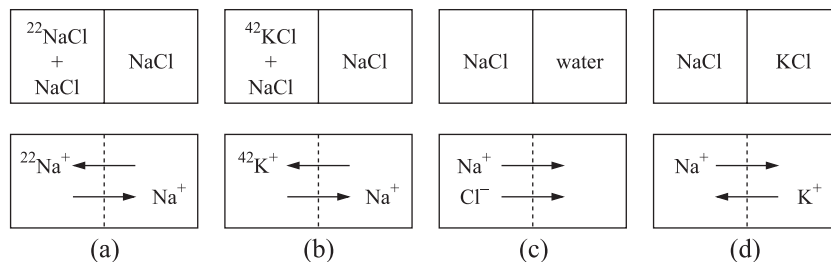


Fig. 8. Different types of diffusion: (a) self-diffusion, (b) tracer diffusion, (c) salt diffusion, and (d) counterdiffusion (according to Ref. [18]).

In case of dilute binary mixtures (one solute and one solvent), the first two types of diffusion (self-diffusion and tracer diffusion) can be described by Fick’s first law [17]:

$$\mathbf{J}_i = -D_i \nabla c_i, \tag{19}$$

where \mathbf{J}_i denotes the molar flux density, D_i is the diffusion coefficient of the ion, and c_i is the concentration of ionic species i . Self-diffusion coefficients for anions and cations in infinitely dilute solutions (Table 5) are computed from the Einstein relation, i.e., from $D_i = RTu_i$, where the experimental values for the mobility u_i are extrapolated to zero concentrations.

For the description of salt diffusion, i.e., diffusion of dilute binary electrolytes [two (charged) solutes and one solvent], the Nernst–Planck (N–P) equation is required [32], reading for individual ions as:

$$\mathbf{J}_i = -D_i \left(\nabla c_i + \frac{F}{RT} z_i c_i \nabla \psi \right), \tag{20}$$

where F is the Faraday constant, z_i and D_i are the charge number and the self-diffusion coefficient of the i th ion, R is the universal gas constant, T is the absolute temperature, and ψ is the electric potential. The N–P Eq. (20) expresses that the ionic species i may be driven by a gradient of the electric field $-\nabla \psi$ (migration) and/or by an ionic concentration gradient $-\nabla c_i$ (diffusion). In the absence of net current flow (electroneutrality), the gradient of the electric potential can be expressed as [32]:

$$\nabla \psi = -\frac{RT}{F} \frac{D_+ - D_-}{z_+ D_+ - z_- D_-} \frac{1}{c_{\text{sol}}} \nabla c_{\text{sol}}, \quad c_{\text{sol}} = \frac{c_+}{v_+} = \frac{c_-}{v_-}, \tag{21}$$

where the subscripts $+/-$ indicate cations and anions, respectively, and c_{sol} denotes the salt concentration. v_+ and v_- are the stoichiometric coefficients of the cations and anions. Integration of Eq. (21) leads the diffusion potential (liquid junction potential) for a binary electrolyte, reading as:

$$\Delta \psi_L = -\frac{RT}{F} \frac{D_+ - D_-}{z_+ D_+ - z_- D_-} \ln \left(\frac{c_{\text{sol},2}}{c_{\text{sol},1}} \right). \tag{22}$$

Insertion of Eq. (21) into the N–P Eq. (20) delivers a steady-state diffusion equation for salts;

$$\mathbf{J}_{\text{sol}} = -D_{\text{sol}} \nabla c_{\text{sol}}, \tag{23}$$

where \mathbf{J}_{sol} and c_{sol} are the molar flux density and the concentration of the respective salt; and the salt diffusion coefficient D_{sol} has the form:

$$D_{\text{sol}} = \frac{D_+D_-(z_+ - z_-)}{z_+D_+ - z_-D_-} \quad (24)$$

(see Table 5). The mathematical similarity between Eq. (23) and Eq. (19) indicates that a salt solved in water behaves like a single ionic species, because of the electroneutrality requirement. In more detail, different self-diffusion coefficients of the anion and cation result in separation of the species. This leads to creation of a minute dipole density which then prevents further separation. The dipole density creates a potential (diffusion potential, Eq. (22)) which acts to speed up the ion with the smaller self-diffusion coefficients and slow down the ion with the larger self-diffusion coefficient.

Experiments show a dependence of salt diffusion coefficients on different concentrations (see Table 6). However, the diffusion coefficients of concentrated solutions (Table 6) and dilute solutions (Table 5) reasonably agree for concentrations up to 3.0 mol/l as far as NaCl and KCl solutions are concerned, and up to 1.0 mol/l for HCl solutions. Because we considered in our scale-transition analysis nondilute concentrations in the micropore solution which are smaller than 3 mol/l, (Table 2), the use of Fick’s law Eq. (7) for the description of diffusive transport in the micropore space of cement paste is justified.

Still, with respect to pure solution systems, additional phenomena affect the diffusive transport in the micropores of cement, reducing the drift speed of chloride. The decrease of ionic drift speed in the pores may be attributed to (i) the presence of an (electrical) diffuse double layer (DDL) on particle surfaces, (ii) the presence of high concentrations of multiple ions in the pore solution, and (iii) changes of the viscosity of the pore solution caused by structuring of water. Let us more profoundly discuss these three possibilities:

(i) Zeta potential measurements of cement pastes [33,34] indicate negative surface charges on cement-paste particles. The region where ‘counterions’ balance this excess charge is generally called electrical DDL [25]. It may be described by double- or triple-layer models (see, e.g., Ref. [35]). However, the presence of a DDL has been shown to *increase* (rather than decrease) the salt diffusivity [25]. At low salinity and/or high cation exchange capacity, there is a large difference in permeability for counterions (Na) and co-ions (Cl), a phenomenon called permselectivity. For a charged porous material at low salinity, the permselectivity increases the (absolute) value of the diffusion potential until its upper bound, which corresponds to the potential of a perfect membrane. The membrane potential increases the velocity of the co-ions to avoid generation of electric current. It follows that the macroscopic

diffusion coefficient is increased by this effect [25]. Consequently, the retardation of chloride ions cannot be attributed to the DDL. The DDL seemingly does not have a discernible effect on the chloride diffusivity of cement pastes at all, probably because of its compression due to salt concentrations around 1 mol/l NaCl, as was shown for platy clay soil [54].

(ii) Experimental investigations of the cement pore solution have shown that the pore solution consists of multiple ions, such as Na^+ , K^+ , Ca^{2+} , OH^- , and SO_4^{2-} ions [21,36–39]. While in this case, the ionic flux of each species can still be quantified by the N–P Eq. (20), the electric potential does not follow any more from Eq. (22), but from the more complex Henderson formula [40]

$$\Delta\psi_L = -\frac{RT}{F} \frac{\sum_{i=1}^N z_i D_i (c_{i,2} - c_{i,1})}{\sum_{i=1}^N z_i^2 D_i (c_{i,2} - c_{i,1})} \ln \left(\frac{\sum_{i=1}^N z_i^2 D_i c_{i,2}}{\sum_{i=1}^N z_i^2 D_i c_{i,1}} \right) \quad (25)$$

This formula allows for quantification of the effect of multiple ions on the chloride diffusivity, e.g., for a NaCl concentration ratio of $c_{\text{sol},2}/c_{\text{sol},1} = 1:10$, addition of ions, such as Na^+ , K^+ , and OH^- in concentrations 150, 400, and 550 mol/m³ to a 1-mol NaCl solution, resulting in a multispecies solution typical for cement pastes [11], which leads to a decrease of the (absolute value of) the diffusion potential from $\psi_L = -12 \text{ mV}^1$ (for the NaCl solution Eq. (22)) to $\psi_L = -3 \text{ mV}$ (for the multispecies solution Eq. (25)). This decrease and specification of the N–P Eq. (20) for chloride, $z_{\text{Cl}} = -1$, show that the presence of Na^+ , K^+ , and OH^- leads to an acceleration (rather than to a retardation) of the chloride drift speed. Hence, judging from the diffusion potential, the decrease of chloride diffusivity in the saturated micropore space of cement pastes cannot be attributed to the presence of multiple ionic species.

A second characteristic of multispecies solutions is the smaller distance between ions, increasing the importance of ion–ion interactions. The presence of high concentrations of multiple ions in solution is standardly taken into account using activity coefficients [41] which describe the deviation of a solution from ideality. There are several theories for describing the relationship between activity coefficient and ionic concentration (strength) of the solution. Among these, the Pitzer model [42] and the extended Debye–Hückel model [43] are most commonly applied. However, application of the latter model for salt concentrations up to 1 mol/l at the pure solution level showed only a small variation of the salt diffusion coefficient,

¹ The diffusion potential is chosen as zero at the upstream side of the sample.

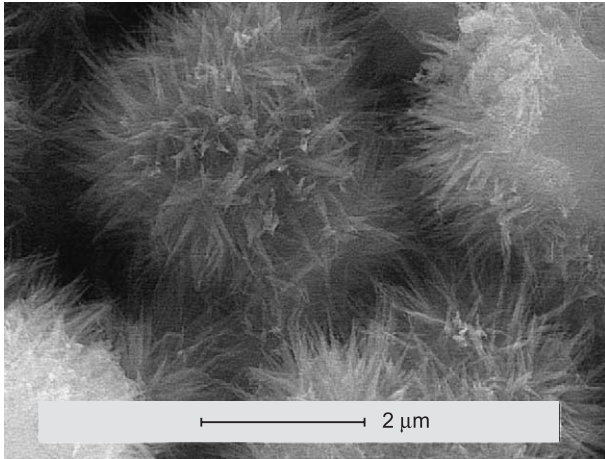


Fig. 9. Morphology of the cement-paste microstructure obtained from environmental scanning electron microscope (ESEM), 28 days after the onset of hydration (according to Ref. [52]).

typically between 4% (for NaCl and KCl solutions) and 8% (for LiCl solution, see Ref. [44] for details). Hence, the influence of additional ions in a multispecies solution seems inappropriate to explain the decrease of salt diffusivity in the micropores of cement pastes by the factor 1/15. This is in agreement with the numerical simulations of multispecies diffusion conducted in Ref. [11].

- (iii) Evidence has been put forward for almost one century that charged surfaces may imply structuring or layering of water (see Ref. [45] for a historical review). This phenomenon is known to occur in numerous materials, including, e.g., biopolymers [46]. In more detail, the polar nature of the water molecules leads to their absorption at the charged surfaces, constituting a first layer. Then, additional layers adhere one upon the other, forming a multilayered network. This layered network has physical properties which are distinctively different from standard liquid water; that is, the viscosity of layered water is significantly higher. Molecular dynamic (MD) simulations of a clay–salt water system show that the salt diffusion coefficient strongly depends on the viscosity of the pore solution [47,48]. While a viscosity of $\mu_w = 0.001$ kg/(m s) leads to a diffusion coefficient of $D_{\text{sol}} \approx 1.7 \times 10^{-9}$ m²/s, which is close to the one for a NaCl solution ($D_{\text{sol}} = 1.61 \times 10^{-9}$ m²/s, see Table 5), an increase of viscosity to $\mu_w = 0.007$ kg/(m s) leads to a diffusion coefficient of $D_{\text{sol}} \approx 2.5 \times 10^{-10}$ m²/s. The latter value is of the same order of magnitude as the chloride diffusivity we determined for the pore solution of cement paste ($D_{\text{poresol,opt}} = 1.1 \times 10^{-10}$ m²/s). The viscosity increase (and the diffusivity decrease, respectively) can be detected over a distance as large as several hundred nanometers [49]. The ‘spiny structure’ of cement paste at complete hydration (Fig. 9) [50] exhibits features of exactly this characteristic length.

This renders structuring of water as the prime candidate for the explanation of the decrease of chloride diffusivity in the micropore space of cement paste with respect to a pure salt solution.

5. Conclusions

For prediction of the apparent chloride diffusivity, cement paste can be modelled by means of a differential homogenization scheme involving nondiffusive spherical inclusions in a diffusive matrix. As a result, chloride diffusivity of cement paste is obtained as a function of the microporosity and the chloride diffusivity in the micropore solution. Remarkably, the latter turns out to be one order of magnitude smaller than the chloride diffusivity in a pure salt solution system. The smaller diffusivity is probably caused by a higher viscosity of the pore solution. This higher viscosity can be explained by the structuring of water molecules along the charged pore surfaces, a well-known phenomenon in clays and biological materials.

Acknowledgements

The first author gratefully acknowledge the financial support of this study by the ‘Austrian Foundation for the Promotion of Scientific Research (FWF)’ in the course of an Erwin Schrödinger scholarship.

Appendix A. Notation

The following notation is used in this paper

A_{sample}	Area of cement-paste sample [m ²]
c_i	Concentration of ions in pure solution [mol/m ³]
c_{sol}	Sodium chloride ion concentration [mol/m ³]
$c_{\text{sol},1}, c_{\text{sol},2}$	Sodium chloride ion concentration in upstream and downstream compartment [mol/m ³]
c_{paste}	Sodium chloride ion concentration in cement paste [mol/m ³]
c_{poresol}	Sodium chloride ion concentration in pore solution of cement paste [mol/m ³]
d	Characteristic pore size [m]
D_i	Self-diffusion coefficient of ion i [m ² /s]
D_{sol}	Salt diffusion coefficient [m ² /s]
D_{solid}	Sodium chloride ion diffusion coefficient of solid phase of cement paste [m ² /s]
D_{paste}	Sodium chloride ion diffusion coefficient in cement paste [m ² /s]
$D_{\text{paste,exp}}$	Experimentally determined sodium chloride ion diffusion coefficient in cement paste [m ² /s]
D_{poresol}	Sodium chloride ion diffusion coefficient in pore solution of cement paste [m ² /s]
$D_{\text{poresol,opt}}$	Sodium chloride ion diffusion coefficient in pore solution of cement paste obtained from optimization analysis [m ² /s]
D_{NaCl}	Sodium chloride diffusion coefficient [m ² /s]
$D_{\text{paste,hom}}$	Homogenized paste diffusion coefficient [m ² /s]
$\bar{\epsilon}$	Relative error between homogenized and experimental diffusion coefficients

Appendix A (continued)

F	Faraday constant $F=96,500$ [C/mol]
\bar{F}	Formation factor [–]
$\mathbf{j}_{\text{poresol}}$	Sodium chloride molar mass flux density in pore solution of cement paste [mol/(m ³ s)]
\mathbf{J}_i	Molar mass flux density of the i th ion [mol/(m ³ s)]
\mathbf{J}_{sol}	Sodium chloride molar mass flux density in pure solution [mol/(m ³ s)]
$\mathbf{J}_{\text{paste}}$	Sodium chloride molar mass flux in cement paste [mol/(m ³ s)]
ℓ	Characteristic length of representative volume element [m]
n	Number of experimental values of apparent diffusion coefficients
R	Universal gas constant $R=8.31$ [J/(K mol)]
t_{sample}	Thickness of cement-paste sample [m]
Δt	Time increment for diffusive transport [s]
T	Absolute temperature [K]
T, \mathbf{T}	Tortuosity factor, tortuosity tensor [–]
u_i	Ion mobility [(m ² mol)/(J s)]
w/c	Water–cement ratio [–]
$(w/c)_i$	Water–cement ratio before curing [–]
$(w/c)_c$	Water–cement ratio after curing [–]
$(w/c)_{\text{exp}}$	Experimental water–cement ratio [–]
V_{paste}	Volume of cement paste [m ³]
\bar{V}_{air}	Volume of air pores normalized with respect to volume of cement at $\xi=0$ [–]
$\bar{V}_{\text{H}_2\text{O}}$	Volume of water normalized with respect to volume of cement at $\xi=0$ [–]
\bar{V}_{hyd}	Volume of hydrates normalized with respect to volume of cement at $\xi=0$ [–]
\bar{V}_{cem}	Volume of cement normalized with respect to volume of cement at $\xi=0$ [–]
Δx	Space increment for diffusive transport (x -direction) [m]
z_i	Charge number of the i th ion [–]
ν_+, ν_-	Stoichiometric coefficients of cations and anions [–]
ξ	Degree of hydration [–]
ρ_{cem}	Mass density of cement [kg/m ³]
ρ_{hyd}	Mass density of hydrates [kg/m ³]
$\rho_{\text{H}_2\text{O}}$	Mass density of water [kg/m ³]
ϕ	Capillary porosity of cement paste [–]
ϕ_{exp}	Experimental capillary porosity of cement paste [–]
$\phi_{\text{exp},i}$	Experimental capillary porosity of i th experiment [–]
ψ	Electric potential [V]
$\Delta\psi_L$	Diffusion potential [V]

References

- [1] C. Page, N. Short, A. Tarras, Diffusion of chloride ions in hardened cement pastes, *Cem. Concr. Res.* 11 (3) (1981) 395–406.
- [2] S. Yu, C. Page, Diffusion in cementitious materials: 1. Comparative study of chloride and oxygen diffusion in hydrated cement pastes, *Cem. Concr. Res.* 21 (1991) 581–588.
- [3] V. Ngala, C. Page, L. Parrott, S. Yu, Diffusion in cementitious materials: 2. Further investigations of chloride and oxygen diffusion in well-cured OPC and OPC/20% PFA pastes, *Cem. Concr. Res.* 25 (4) (1995) 819–826.
- [4] L. Tang, L.-O. Nilson, Rapid determination of chloride diffusivity in concrete by applying an electrical field, *ACI Mater. J.* 89 (1) (1992) 49–53.
- [5] K. MacDonald, D. Northwood, Experimental measurements of chloride ion diffusion rates using a two-compartment diffusion cell: effects of material and test variables, *Cem. Concr. Res.* 25 (7) (1995) 1407–1416.
- [6] T. Zhang, O.E. Gjorv, Effect of ionic interaction in migration testing of chloride diffusivity in concrete, *Cem. Concr. Res.* 25 (7) (1995) 1535–1542.
- [7] J.-Z. Zhang, N. Buenfeld, Presence and possible implications of a membrane potential in concrete exposed to chloride solution, *Cem. Concr. Res.* 27 (6) (1997) 853–859.
- [8] S. Chatterji, Colloid electrochemistry of saturated cement paste and some properties of cement based materials, *Adv. Cem. Based Mater.* 7 (1998) 102–108.
- [9] E. Samson, G. Lemaire, J. Marchand, J. Beaudoin, Modeling chemical activity effects in strong ionic solutions, *Comput. Mater. Sci.* 15 (1999) 285–294.
- [10] E. Samson, J. Marchand, Numerical solution of the extended Nernst–Planck model, *J. Colloid Interface Sci.* 215 (1999) 1–8.
- [11] O. Truc, J. Ollivier, L. Nielsson, Numerical simulation of multi-species transport through saturated concrete during migration test—MsDiff code, *Cem. Concr. Res.* 30 (2000) 1581–1592.
- [12] M. Castellote, C. Alonso, C. Andrade, G. Chadbourn, C. Page, Oxygen and chloride diffusion in cement pastes as a validation of chloride diffusion coefficients obtained by steady-state migration tests, *Cem. Concr. Res.* 31 (2001) 621–625.
- [13] H. Hornain, J. Marchand, V. Duhot, M. Moranville-Regourd, Diffusion of chloride ions in limestone filler blended cement pastes and mortars, *Cem. Concr. Res.* 25 (8) (1995) 1667–1678.
- [14] P. Sen, C. Scala, M. Cohen, A self-similar model for sedimentary rocks with application to the dielectric constant of fused glass beads, *Geophysics* 46 (5) (1981) 781–795.
- [15] L. Dormieux, E. Lemarchand, Homogenization approach of advection and diffusion in cracked porous media, *ASCE J. Eng. Mech.* 127 (12) (2001) 1267–1274.
- [16] M. Castellote, C. Andrade, C. Alonso, Measurement of steady and non-steady-state chloride diffusion coefficients in a migration test by means of monitoring the conductivity in the anolyte chamber. Comparison with natural diffusion tests, *Cem. Concr. Res.* 31 (10) (2001) 1411–1420.
- [17] E. Cussler, *Diffusion Mass Transfer in Fluid Systems*, 2nd edition, Cambridge Univ. Press, New York, USA, 1997.
- [18] C. Shackelford, D. Daniel, Diffusion in saturated soil: I. Background, *Geotech. Eng.* 117 (3) (1991) 467–484.
- [19] C. Dehghanian, M. Arjemandi, Influence of slag blended cement concrete on chloride diffusion rate, *Cem. Concr. Res.* 27 (6) (1997) 937–945.
- [20] K. Ampadu, K. Torii, M. Kawamura, Beneficial effect of fly ash on chloride diffusivity of hardened cement paste, *Cem. Concr. Res.* 29 (1999) 585–590.
- [21] N. Buenfeld, G. Glass, A. Hassanein, J.-Z. Zhang, Chloride transport in concrete subjected to electric field, *ASCE J. Mater. Civ. Eng.* 10 (4) (1998) 220–228.
- [22] E. Garboczi, D. Bentz, Computer simulation of the diffusivity of cement based materials, *J. Mater. Sci.* 27 (1992) 2083–2092.
- [23] R. Robinson, R. Stokes, *Electrolyte Solutions*, 2nd edition, Butterworths, London, England, 1959.
- [24] J. Bear, Y. Bachmat, *Introduction to Modelling of Transport Phenomena in Porous Media*, vol. 4, Kluwer Academic Publishing, Dordrecht, Netherlands, 1991.
- [25] A. Revil, Ionic diffusivity, electrical conductivity, membrane and thermoelectric potentials in colloids and granular porous media: a unified model, *J. Colloid Interface Sci.* 212 (1999) 503–522.
- [26] A. Zaoui, Structural morphology and constitutive behavior of microheterogeneous materials, in: P. Suquet (Ed.), *Continuum Micromechanics*, CISM courses and lectures No. 377, International Centre for Mechanical Science, Springer, New York, USA, 1997, pp. 291–347.
- [27] E. Lemarchand, Contribution de la micromécanique à l'étude des phénomènes de transport et couplage poromécanique dans les milieux poreux: Application aux phénomènes de gonflement dans les géomatériaux, Ph.D. thesis, Ecole Nationale des Ponts et Chaussées, Paris, France, 2001.
- [28] J.D. Eshelby, The determination of the elastic field of an ellipsoidal inclusion, and related problems, *Proc. R. Soc. Lond., A* 241 (1226) (1957) 376–396.

- [29] P. Acker, Micromechanical analysis of creep and shrinkage mechanisms, in: F.-J. Ulm, Z. Bažant, F. Wittmann (Eds.), *Creep, Shrinkage, and Durability of concrete and other Quasi-brittle Material—Proceedings of the Sixth International Conference CONCREEP-6@MIT*, Elsevier, Amsterdam, 2001, pp. 15–26.
- [30] L. Tang, Concentration dependence of diffusion and migration of chloride ions: Part 1. Theoretical considerations, *Cem. Concr. Res.* 29 (1999) 1463–1468.
- [31] G. Glass, N. Buenfeld, Theoretical assessment of steady state diffusion cell test, *J. Mater. Sci.* 33 (1998) 5111–5118.
- [32] J. Newman, *Electrochemical Systems*, 2nd edition, Prentice-Hall, Englewood Cliffs, NJ, USA, 1991.
- [33] E. Nägele, The zeta potential of cement, *Cem. Concr. Res.* 15 (3) (1985) 453–462.
- [34] E. Nägele, The transient zeta potential of hydrating cement, *Chem. Eng. Sci.* 44 (8) (1989) 1637–1645.
- [35] P. Hiemenz, R. Rajagopalan, *Principles of Colloid and Surface Chemistry*, 3rd edition, Marcel Dekker, New York, USA, 1997.
- [36] S. Diamond, Effects of two Danish fly ashes on alkali contents of pore solutions of cement–fly ash pastes, *Cem. Concr. Res.* 11 (1981) 383–394.
- [37] C. Andrade, Calculation of chloride diffusion coefficients in concrete from ionic migration measurements, *Cem. Concr. Res.* 23 (1993) 724–742.
- [38] T. Zhang, O.E. Gjorv, An electrochemical method for accelerated testing of chloride diffusivity of concrete, *Cem. Concr. Res.* 24 (8) (1994) 1534–1548.
- [39] S. Chatterji, Evidence of variable diffusivity of ions in saturated cementitious materials, *Cem. Concr. Res.* 29 (1999) 995–998.
- [40] F. Helfferich, *Ion Exchange*, McGraw-Hill, New York, USA, 1962 (series in *Advanced Chemistry*).
- [41] P. Atkins, J. de Paula, *Atkins' Physical Chemistry*, 7th edition, Oxford Univ. Press, New York, USA, 2002.
- [42] K. Pitzer, Thermodynamics of electrolytes: I. Theoretical basis and general equations, *J. Phys. Chem.* 77 (2) (1973) 268–277.
- [43] U. Kunze, *Grundlagen der quantitativen Analyse*, 2nd edition, Georg Thieme, Stuttgart, Germany, 1986.
- [44] L. Tang, Concentration dependence of diffusion and migration of chloride ions: Part 2. Experimental evaluations, *Cem. Concr. Res.* 29 (1999) 1469–1474.
- [45] G. Pollack, *Cells, Gels and the Engines of Life: A New Unifying Approach to Cell Function*, Ebner and Sons, Seattle, WA, USA, 2001.
- [46] J. Israellachvili, H. Wennerström, Role of hydration and water structure in biological and colloidal interactions, *Nature* 379 (1996) 219–225.
- [47] Y. Ichikawa, K. Kawamura, M. Nakano, K. Kitayama, N. Fujii, Molecular behavior and micro/macro analysis of diffusion problem in bentonite, *CDROM Proceedings of the European Congress on Computational Methods in Applied Sciences and Engineering*, Barcelona, Spain, 2000.
- [48] Y. Ichikawa, K. Kawamura, N. Fujii, T. Nattavut, Molecular dynamics and multiscale homogenization analysis of seepage/diffusion problem in bentonite clay, *Int. J. Numer. Methods Eng.* 54 (2002) 1717–1749.
- [49] A. Szent-György, *The Living State. With Observations of Cancer*, Academic Press, New York, USA, 2001.
- [50] M. Ashby, D. Jones, *Engineering Materials*, vol. 2, Elsevier, New York, USA, 1994.
- [51] A. Asbridge, G. Chadbourn, C. Page, Effects of metakaolin and the interfacial transition zone on the diffusion of chloride ions through cement mortars, *Cem. Concr. Res.* 31 (2001) 1567–1572.
- [52] J. Tritthart, F. Häußler, Pore solution analysis of cement pastes and nanostructural investigations of hydrated C_3S , *Cem. Concr. Res.* 33 (2003) 1063–1070.
- [53] J. Stark, B. Wicht, *Dauerhaftigkeit von Beton*, 2nd edition, Birkhäuser, Basel, Schweiz, 2001.
- [54] D. Smith, P. Pivonka, C. Jungnickel, S. Fiytus, Theoretical analysis of anion exclusion and diffusive transport through platy-clay soils, *Trans. Porous Media* 55 (2004) 1–27.

D. Smith, **P. Pivonka**, Ch. Jungnickel, and S. Fityus. Theoretical analysis of anion exclusion and diffusive transport through platy-clay soils. *Transport in Porous Media*, **57** (3), pp 251-277, 2004.

Theoretical Analysis of Anion Exclusion and Diffusive Transport Through Platy-Clay Soils

DAVID SMITH^{1,*}, PETER PIVONKA¹, CHRISTIAN JUNGNICHEL²
and STEPHEN FITYUS²

¹*Department of Civil and Environmental Engineering, The University of Melbourne, VIC 3010, Australia*

²*School of Engineering, The University of Newcastle, Callaghan, NSW 2300, Australia*

(Received: 16 July 2002; in final form: 10 December 2003)

Abstract. Diffusive transport through geosynthetic clay liners and engineered compacted clay landfill liners is the primary mechanism for mass transport from well-engineered modern landfills. For this reason, accurate estimates of diffusion coefficients for clay soils are essential for the design of engineered liner systems. A long-standing theoretical problem is the role of *anion exclusion* on the estimation of diffusion coefficients for ionic solutes migrating through charged porous media. This paper describes the steady-state solution of a fully coupled set of transport equations modeling ion movement through a permanently charged platy-clay soil. The microscale analysis takes into account the actual diffusion coefficient for each ion species, ion-pairing (as required by electroneutrality of the solution), as well as *anion exclusion* and *cation inclusion*, arising from the permanent charge on clay particles. To render the problem tractable, the theoretical analysis focuses on an extremely small two-dimensional unit cell in an ideal, saturated, two-phase porous medium. The analysis presented here is limited to a particular geometrical example, but this example is sufficiently general for characteristic behaviours of systems of this kind to be identified. Most importantly, new insight is gained into the mechanism of ion migration through a charged platy-clay soil. The numerical results obtained from this study show that the identification of macroscopic transport quantities such as effective diffusion coefficients and membrane potentials from diffusion cell tests using *standard diffusion theory* only hold for a specific system. While *ion exclusion* behaviours are often referred to in the literature, as far as the authors are aware there has been no previous detailed microscale analysis of their role in steady-state diffusion through a charged platy-clay soil.

Key words: anion exclusion, multi-ion transport, Nernst–Planck equation, Gauss’s electrostatic theorem, effective porosity, effective diffusion coefficient, clay soils.

1. Introduction

Following intensive research by geoenvironmental engineers over the last twenty years, the engineering design of compacted clay liners for waste disposal facilities is now well established (see, e.g., Day and Daniel, 1985; Rowe

*Author for correspondence: Phone: +61-3-8344-4061; Fax: +61-3-8344-4616; e-mail: david.smith@unimelb.edu.au

et al., 1995; August *et al.*, 1997; Rowe, 2001). A key design aim is to minimize advective transport of solutes through the compacted clay liner by keeping the leachate mound height in the landfill small, and the permeability of the clay low. When this is successfully achieved and advective transport is minimized, the primary mechanism transporting chemicals from the landfill to the surrounding biological environment is diffusion of the chemicals along their electrochemical potential gradients. For this reason, considerable effort has been devoted to estimating diffusion coefficients for solutes transported through compacted and natural clay soils (Rowe *et al.*, 1988; Shackelford and Daniel, 1991a, b; Barone *et al.*, 1992; Rowe, 1998). Whereas experimental data on diffusive transport of uncharged solutes show reasonable good agreement between estimated diffusion coefficients reported from different laboratories, there is a large scatter of estimated diffusion coefficients for charged solutes. Developing a deeper understanding of ion migration through charged platy-clay soils like montmorillonite provides the primary motivation for the present paper.

Beginning with a presentation of the most common approach employed by geoenvironmental engineers for the estimation of diffusion coefficients (Subsection 1.1), we describe some arguments used by different researchers for explaining the observed experimental data. Based on these findings we state the objectives of the present approach (Subsection 1.2) and then describe some of the limitations of the model employed in this paper. Section 2 describes the governing equations, starting with the description of multi-ion transport at the microscale considering chemical and electrical couplings (i.e., the Nernst–Planck equation and the Poisson equation of electrostatics (Subsection 2.1)). The macroscopic governing equations are obtained by (volume) averaging of the microscopic governing equations (Subsection 2.2) leading to the definitions for the apparent and effective diffusion coefficient and membrane potential. The predictive capabilities of the model are investigated on a microscale unit cell representing an assembly of charged clay particles (Section 3). Three different subproblems related to the uncertainties in experimental interpretation (reported in Subsection 1.1) are investigated. The first (Subsection 3.1) deals with diffusive transport of uncharged solutes. The second (Subsection 3.2) investigates the commonly used concept of *effective porosity*. Finally, the third (Subsection 3.3) deals with steady-state diffusion of a binary electrolyte through a permanently charged platy-clay soil.

1.1. CONVENTIONAL APPROACH TO THE DESCRIPTION OF DIFFUSIVE MASS TRANSPORT AND IMPLICATIONS

In the following, only the essential results for the mathematical description of diffusive transport through soils are given. Steady-state diffusion of solutes through water-saturated soil samples is usually described by Fick's first law

(Dutt and Low, 1962; Gillham *et al.*, 1984; Shackelford and Daniel, 1991a; Kozaki *et al.*, 2001)

$$\langle \mathbf{j}_i \rangle = -\mathbf{D}_i \cdot \nabla \langle c_i \rangle, \quad (1)$$

whereas non-steady state conditions are described by Fick's second law (Robin *et al.*, 1987; Shackelford and Daniel, 1991a)

$$\frac{\partial(n\langle c_i \rangle)}{\partial t} = -\nabla \cdot \langle \mathbf{j}_i \rangle. \quad (2)$$

$\langle \cdot \rangle$ denote macroscopic (volume averaged) quantities obtained from a micro-macro transition method or experimental measurements (see Subsection 2 for details). $\langle \mathbf{j}_i \rangle$, \mathbf{D}_i , and $\nabla \langle c_i \rangle$ are the molar flux, the second-order diffusivity tensor, and the concentration gradient of solute i in the soil pore solution, respectively. Given an isotropic material with a diffusion coefficient D_i , the diffusivity tensor can be expressed as, $\mathbf{D}_i = \mathbf{1}D_i$, with $\mathbf{1}$ being the second order unity tensor. \mathbf{D}_i is commonly referred to as the *apparent (or soil) diffusion coefficient* and estimated by diffusion cell tests (see, e.g., Dutt and Low, 1962; Kemper and van Schaik, 1966; Gillham *et al.*, 1984; Rowe *et al.*, 1988; Shackelford and Daniel, 1991b; Rowe, 1998 for details). A relation between the apparent diffusion coefficient of the soil and the pore solution diffusion coefficient is given by (Bear and Bachmat, 1991; Dormieux and Lemarchand, 2001):

$$D_i = n\tau D_{0,i} \quad \text{with} \quad n = \frac{V_f}{V_T} = \frac{V_T - V_s}{V_T}, \quad (3)$$

where n denotes the soil porosity and $D_{0,i}$ is the self-diffusion coefficient of solute i in the pore fluid of the soil (see Table I for self-diffusion coefficient of chloride). V_f , V_s , and V_T are the volumes of the fluid phase, the solid phase and the total soil volume, respectively. The (dimensionless) quantity τ is known as the *tortuosity factor* (see Section 2.2 for details). It is noted that the product of τ and $D_{0,i}$ is often defined as the *effective diffusion coefficient*:

$$D_{\text{eff},i} = \tau D_{0,i}. \quad (4)$$

Experimentally observed effective diffusion coefficients for clay soils for some charged solutes are given in Table I (further effective diffusion coefficients of various species can be found in Rowe *et al.* (1995, pp. 223–228)). It should be noted that depending on the definition of diffusion coefficient (i.e., apparent or effective diffusion coefficient) different values may be tabulated. Hence, one must be careful which definition has been chosen for the evaluation of experimental data (see Shackelford and Daniel, 1991a, for further discussion). The theory described above is well established and has been applied with considerable success in geoenvironmental engineering applications (Rowe and Booker, 1984; Shackelford and Daniel, 1991a, b; Rowe *et al.*, 1995; Rowe, 1998, 2001). However, when attempting to estimate the diffusion coefficients

Table I. Experimental data on effective diffusion coefficients and tortuosity factors evaluated from Equation (4)

Species	Soil	D_{eff} (10^{10} m ² /s)	n	τ	References
³⁶ Cl	Clay	6.10	0.28	0.31	Clarke and Graham (1968)
	Montmorillonite	3.82	0.76	0.19	Kozaki <i>et al.</i> (2001)
	Clay	1.60	–	0.08	Robin <i>et al.</i> (1987)
NaCl	Montmorillonite	4.11	0.90	0.20	Dutt and Low (1962)
	Montmorillonite	3.13	0.85	0.15	Kemper and van Schaik (1966)
Cl ⁻	Silty clay	5.70	0.10	0.28	Rowe <i>et al.</i> (1988)
	Silty clay	5.60	0.10	0.28	Barone <i>et al.</i> (1992)
	Clayey till	3.00	0.29–0.41	0.15	Desaulniers <i>et al.</i> (1981)
	Silty clay	2.64–6.10	0.21	0.13–0.30	Crooks and Quigley (1984)
	Silty clay	2.03	–	0.10	Quigley <i>et al.</i> (1984)
	Silty clay loam;	1.62–4.47	–	0.08–0.22	Barracough and Tinker (1981)
	Sandy loam	–	–	–	–
	Kaolinite	2.44–10.2	–	0.12–0.5	Shackelford (1988)
	Smectic clay	1.42–4.87	–	0.07–0.24	Shackelford (1988)

The chloride self-diffusion coefficient was taken as $D_{0,\text{Cl}} = 2.03 \cdot 10^{-9}$ m²/s.

for charged solutes in charged porous media a problem is encountered because of so-called *ion exclusion*. Ion exclusion is produced by electrostatic repulsion of ions away from particle surfaces of like charge (for example, anions are typically repelled from the surfaces of clay particles, as the clay particles usually have a permanent negative charge). Because anions are repelled from the negatively charged surface, the *effective porosity* for anions in a clay soil is reduced. This phenomenon is known as *anion exclusion* (Dutt and Low, 1962). When dealing with charged solutes diffusing through a charged porous medium, Fick's first law (1) and Fick's second law (2)) are sometimes modified to account for electrical effects by using the concept of *effective porosity* (Thomas and Swoboda, 1970; Bresler, 1973; Appelt *et al.*, 1975; Bond *et al.*, 1982; Rowe *et al.*, 1995; Shukla *et al.*, 1999). It is usually believed that ion exclusion may be taken into account by replacing the soil porosity (n) in Equation (2) and Equation (3) by a so-called *effective porosity* (n_{eff}). The effective porosity is defined as (Bresler, 1973; Bond *et al.*, 1982; Sposito, 1989)

$$n_{\text{eff}} = \frac{V_f - V_{\text{ex}}}{V_T}, \quad (5)$$

where V_{ex} is the *excluded volume* of the anion. The excluded volume may be estimated by evaluating the integral (Sposito, 1989, pp. 158)

$$V_{\text{ex}} = \int_{V_i} \left(1 - \frac{c_i}{\bar{c}_i} \right) dV. \quad (6)$$

c_i is the concentration of the i th anion in a clay pore solution with a permanent charge and \bar{c}_i is the concentration of the i th anion in an identical clay soil without a permanent charge.

Practically, the effective porosity may be estimated in the laboratory by means of macroscopic measurements on a so-called *batch test*. For a batch test, c_i and \bar{c}_i may be estimated by first separating the solid from the supernatant liquid (for example, by spinning down the solid fraction in a centrifuge), and then measuring c_i in the solid fraction and \bar{c}_i in the supernatant liquid. Estimation of the excluded volume from Equation (6) and substitution of this value in Equation (5) yields an estimate of the effective porosity of the soil (see Sposito, 1989 for details).

In an alternative approach, (Rowe *et al.*, 1995) discusses the estimation of the effective porosity using a diffusion cell test and a conservative anion (i.e., an ion which has no sorption onto the solid phase during transport). In these tests the effective diffusion coefficient and effective porosity for potassium chloride diffusing through a natural clay soil were estimated by back-analysis (i.e., by solving the inverse problem). Rowe *et al.* (1995) concluded that the effective porosity for the chloride anion was close to the actual porosity of the soil (as estimated from the gravimetric moisture content of the soil). However, as a caveat on their finding, they noted that the soil in the test had a low activity (suggesting the permanent charge on the clay particles is small, and consequently the anion exclusion volume is small). However, Rowe *et al.* (1995) notes that other authors have shown the effective porosity to be significantly less than the actual porosity, and so imply that while in their case the effective porosity was close to the actual porosity, in other cases it maybe quite different.

It should be noted that different authors chose different ways of introducing the effective porosity into Equation (1) and Equation (2). While some authors substitute n_{eff} for n on the left hand side of Equation (2) while keeping the total porosity in the definition of D_i (see e.g., Bresler, 1973; James and Rubin, 1986), others use n_{eff} on both sides (see e.g., Shackelford and Daniel, 1991a; Rowe *et al.*, 1995). These discrepancies clearly introduces some additional uncertainties in interpretation of the theoretical results.

Experimental results on steady-state diffusion of different salts through montmorillonite were reported in Dutt and Low (1962) and Kemper and van Schaik (1966). For NaCl diffusing through the clay plug ($n \approx 0.9$) both obtained a nonlinear concentration distribution over the length of the specimen.

Using Equation (1) for estimation of apparent diffusion coefficients leads to a diffusion coefficient depending on the spatial coordinate (measured in the direction of diffusive transport) and, hence, on the salt concentration. According to these experiments the apparent diffusion coefficient increased with decreasing salt concentration (mean values of effective diffusion coefficients are given in Table I). Dutt and Low (1962) justified their findings by a rather elaborate argument based on the increase of the viscosity of the pore fluid in the vicinity of clay particles. On the other hand, Kemper and van Schaik (1966) explained the observed nonlinearity of the concentration distribution across the clay specimen by the development of an osmotically induced flow across the clay plug (from the low concentration side to the high concentration side).

1.2. OBJECTIVES OF THE PRESENT APPROACH

The uncertainties in interpretation of the experimental data described above may stem from measurement errors and/or using a theory based on assumptions which do not hold for the experiments under investigation. Because most of the experiments reported above used rather large sample numbers the measurement uncertainty is an unlikely explanation.

On the other hand, use of Fick's first law (1) is based on the assumption that ions only respond to a gradient of concentration. However, it is well established that charged solutes respond to a gradient of concentration and to any electrical field present. One immediate effect of a charged solute responding to both driving forces is that the *diffusion coefficient* can only be estimated for a particular *ion pair*. If the *partner ion* in the ion-pair is changed (or if other ions are added to the solution), then a different *diffusion coefficient* would be estimated for a particular test using Equation (1). This is one indication that the diffusion coefficients for *individual ions* estimated experimentally for a complex material like clay soil actually represent mass transfer coefficients for a particular system under investigation, rather than fundamental (system independent) quantities such as pore solution diffusion coefficients (see Cussler, 1997 for details).

The ion transport theory employed in the present paper takes into account gradients of concentration and electrical potential together with pore solution diffusion coefficients for each individual ion. Application of this theory to a microscopic unit cell allows for new insight into ion migration through charged porous media, and with suitable upscaling, can allow for the interpretation of macroscopic transport quantities.

However, before proceeding to investigate numerically ion transport through charged platy-clay soil, we first note that the theoretical study described here is based on the following assumptions and limitations: (i) Only a small assembly of clay particles is analysed by the microscale governing

equations. This is necessary because of the complexity of the governing equations and the rather fine discretization of the domain necessary for accurate finite element analyses. A similar approach has been adopted by previous authors for similar reasons (e.g. Quintard and Whitaker, 1993). (ii) The analysis is limited to two spatial dimensions, when in fact the clay particles are three-dimensional structures. Again this is done to simplify the problem, but the two-dimensional model is nevertheless expected to yield useful information. (iii) While it is straight forward to incorporate sorption in the model, as only steady-state diffusive transport is considered here, sorption is not required. (iv) The diffuse double-layer comprising the clay particles and associated counter-ions in solution is approximated by the Gouy–Chapman theory. While more sophisticated models of the diffuse double-layer have been developed (e.g. triple layer models), such refinements are not included because they only complicate the interpretation of the numerical analyses without changing the fundamental system behaviour. (v) Changes in the pore water viscosity within the diffuse double-layer are neglected. According to recent molecular dynamics simulations (Ichikawa *et al.*, 2002) the viscosity of the pore fluid is usually only significantly changed for a distance of one (to possibly two) nanometers for the surface of a strongly charged clay particle like montmorillonite. The length scales of the clay-water system analysed in this paper are significantly greater than one to two nanometers, hence, neglecting of viscosity changes in the pore water is reasonable. (vi) Surface diffusion is neglected. Some authors have reported that surface diffusion on the solid surface is important for the transport of radionuclides (e.g. Berry and Bond, 1992), but this is also neglected for simplicity. (vii) The influence of osmotically induced fluid flows is not considered. While osmotically induced flows often occur in saturated smectitic soils, this effect is more evident at low porosities and are usually negligible when the porosity is large, as in the example problem examined here. It is noted that the absence of osmotically induced flows implies the absence of streaming potentials (Mitchell, 1993).

While these limitations point to obvious improvements that could be made to better reflect the conditions in an actual platy-clay soil, we believe the model described here nevertheless gives important new insights into the steady-state mass transfer properties of charged platy-clay soils (see Section 3).

2. Governing Transport Equations

Diffusive transport of solutes in a porous medium typically takes place in the pores of the material. For clay materials, the pore sizes range between one nanometer up to some microns. Considering the large ratio of pore diameters to the diameter of the ions transported, a continuum description of diffusive

transport of solutes through the (saturated) pores is reasonable, provided the pore size is greater than about 5 nm.

2.1. MICROSCALE MULTI-ION TRANSPORT MODEL

We consider clay as a porous medium defined on a representative volume element (RVE) of several hundreds of nanometers characteristic length. This medium consists of two phases, a micropore space filled with a solution containing solutes and a solid phase consisting of aluminosilicates. In the following, the surface and the solid phase is regarded as non-diffusive (i.e., $D_{\text{surface},i} = 0$, $D_{\text{solid},i} = 0$),¹ we assign every solute a pore solution diffusion coefficient $D_{\text{poresol},i}$. Assuming that the pore fluid of the soil behaves such as an ideal solution, the species self-diffusion coefficient can be substituted for the pore-solution diffusion coefficient, i.e., $D_{\text{poresol},i} = D_{0,i}$ (see $D_{0,\text{Cl}}$ for chloride in Table I). The key constitutive equation describing microscale ion transport in the presence of electrochemical forces is the Nernst–Planck (N–P) equation (Cussler, 1997),

$$\mathbf{j}_i = -D_{0,i} \left(\nabla c_i + \frac{F}{RT} c_i z_i \nabla \psi \right) \quad (7)$$

where \mathbf{j}_i is the molar flux density of the i th ion, c_i the concentration of the i th ion, ∇c_i the concentration gradient of the i th ion in the pore solution; z_i the valence of the i th ion, $\nabla \psi$ the voltage gradient, and F , R and T are the Faraday constant, gas constant, and absolute temperature, respectively.

The first term inside the brackets results in transport of the i th ion species along minus of the concentration gradient.² The second term inside the brackets results in transport along the voltage gradient.³ The Nernst–Planck equation is a generalisation of Fick’s law, taking into account electrical effects on charged solutes. The voltage (ψ) appearing in Equation (7) is made up of two distinct parts. The first part of the voltage arises from any external potential applied to the system (for example, the external voltage may result from the accumulation of excess ions on one side of a clay barrier membrane). The second part of the voltage arises from the potential generated by the diffusion coefficients of the individual ions being different, leading to the formation of ion-pair dipoles.⁴ This second potential is known as the diffusion potential. However, the ions in solution are influenced by the electric

¹While diffusion either on the surface of the solid phase or through the solid phase may occur, these diffusion coefficients are typically several orders of magnitude smaller than the diffusion coefficient of solutes in the pore fluid and for this reason are neglected here.

²More general, ion transport is driven by the gradient of the chemical potential. However, for the case of ideal solutions the gradient of the chemical potential equals the concentration gradient.

³Note that the direction of the transport depends on the charge on the ion (z_i).

⁴Ion pair dipoles are present only in a time-averaged sense.

potential irrespective of its origin, so the two voltages arising from either process may be summed and represented by a single ψ .

The Nernst–Planck equation for ionic species (7), are supplemented by mass conservation equations. Mass conservation for each conservative ion species is expressed by

$$\frac{\partial c_i}{\partial t} = -\nabla \cdot \mathbf{j}_i, \quad (8)$$

where $\nabla \cdot \mathbf{j}_i$ is divergence of the flux of the i th ion, and t is time. Substitution of the flux equation (7) into the mass conservation equation (8) leads to the governing differential equation for mass transport in the clay pore solution. In order to complete this system of equations, one has to define a relationship that couples the transport of all ionic species to one another. Commonly applied constraint equations are:

$$\sum_{i=1}^N z_i c_i = 0 \quad \text{electroneutrality condition,} \quad (9)$$

$$\nabla \psi = \text{const} \quad \text{constant field assumption,} \quad (10)$$

$$\mathbf{i} = F \sum_{i=1}^N z_i \mathbf{j}_i = 0 \quad \text{nil current condition.} \quad (11)$$

Equations (9)–(11) only hold for special situations depending on the problem being investigated.⁵ The most rigorous way is to relate the variation of the electric potential to the spatial distribution of the electric charges. This relationship is given by Gauss's electrostatic theorem (sometimes referred to as the Poisson equation) (Newman, 1991):

$$\nabla \cdot (\varepsilon \nabla \psi) = F \sum_{i=1}^N z_i c_i, \quad (12)$$

where the permittivity ε is the product of the permittivity of free space, ε_0 , and the relative permittivity ε_w (of water). For the special case of a binary monovalent electrolyte (i.e., $N = 2$) the influence of the constraint equations (9) and (10) on the numerical results were discussed in Kato (1995). It was found that the electroneutrality condition (9) and the constant electric field assumption (10) are limiting asymptotic solutions of the Poisson Equation (12) (see Kato, 1995; MacGillivray, 1968 for details).

The system of simultaneous partial differential Equations (7), (8) and (12) must be solved over the domain of the clay particles subject to appropriate

⁵For example electroneutrality is observed in all solutions except in thin double layers near electrodes and charged particles in porous materials.

initial and boundary conditions. The choice of initial and boundary conditions necessary for the problems analyzed are discussed in Section 3.

2.2. MACROSCALE MULTI-ION TRANSPORT MODEL

Equations (7), (8), and (12) describe ion transport driven by gradients of concentration and electrical potential at the microscale. However, most engineering applications deal with the investigation of macroscopic transport properties such as measurement of macroscopic diffusion coefficients, conductivities, and membrane potentials. There are various alternatives to describe diffusive transport quantities for porous media at the macroscale. Macroscopic governing equations derived empirically are often referred to as phenomenological equations. On the other hand, if the underlying behaviour of the system is understood at a deeper level, these equations are derived through a mathematical process known as *up-scaling* or *homogenization*. Up-scaling is a (volume) averaging method (see, e.g., Bear and Bachmat, 1991; Whitaker, 1999), where microscopic quantities are averaged over a representative volume element (RVE) in order to obtain macroscopic quantities. The notion of the RVE forms the basis of the volume averaging method. The RVE must be large enough in order to capture defined material properties (such as porosity, solid fraction, etc.) correctly. In the following, volume averaged quantities are defined as (Whitaker, 1999):

$$\langle \cdot \rangle = \frac{1}{V_T} \int_{V_T} \cdot \, dV, \quad (13)$$

where V_T denotes the total macroscopic volume of the RVE. Integration of the governing equations over the volume V_T leads to the macroscopic transport equations (Samson *et al.*, 1999):

$$\langle \mathbf{j}_i \rangle = -D_i \left(\nabla \langle c_i \rangle + \frac{F}{RT} \langle c_i \rangle z_i \nabla \langle \psi \rangle \right), \quad (14)$$

$$\frac{\partial (n \langle c_i \rangle)}{\partial t} = \nabla \cdot \langle \mathbf{j}_i \rangle, \quad (15)$$

$$\nabla \cdot (\varepsilon_{\text{app}} \nabla \langle \psi \rangle) = nF \sum_{i=1}^N z_i \langle c_i \rangle + nF \omega \langle X \rangle, \quad (16)$$

where ε_{app} denotes the apparent (or soil) permittivity, X denotes the fixed charge concentration, and ω is the sign of the fixed charge concentration (i.e., negative for negatively charged materials).

The apparent solute diffusion coefficient of the soil is given as (compare with Equation (3) and Bear and Bachmat, 1991):

$$D_i = n\tau_i D_{0,i} = nD_{\text{eff},i} \quad (17)$$

τ_i denotes the tortuosity factor of individual ions. Neglecting electrical effects (i.e., setting $\nabla\langle\psi\rangle = 0$) in Equation (14) yields Fick's first law (compare with Equation (1)). In the case of uncharged porous media the tortuosity factor is a purely geometrical quantity characterizing the pore morphology (Bear and Bachmat, 1991). Values of τ_i ranges between 0 (impermeable pores) and 1 (cylindrical pores). For uncharged porous materials the tortuosity is the same for all diffusing species, i.e., $\tau_i = \tau = \text{const}$. For the case of charged porous materials, the pathways of diffusing cations and anions are different depending on the permanent charge on the particles, the charge of the diffusing ion and the salt concentration (see, e.g., Sen, 1989 and Revil, 1999). In the case of negatively charged porous materials, anions are repelled from the charged surface. It is noted that at high salinity, diffuse double-layers are strongly compressed. In this case the dominant paths for diffusive transport are located in the interconnected pore space, and in the limit, the tortuosities for the transport of anions and cations are equal. As the salinity decreases, the dominant paths for diffusion of cations shift and weighted towards the solid-water interface. The reverse happens for the anions, and so the pathways followed by cations and anions are different, and these different pathways are described by different tortuosities (see Sen, 1989; Revil, 1999 for details).

In the next section, the qualitative arguments given by Sen (1989) and Revil (1999) about cation and anion migration pathways in charged porous media will be investigated quantitatively, and rendered visually explicit using detailed *ion distribution maps*. This is possible by solving the governing equations at the microscale (which describes the behaviour of a *unit cell* in the material), for a particular set of boundary conditions. We believe this leads to new insight into ion migration through charged porous media.

Here we note that the macroscopic equations (14)–(16) are only applicable when the gradient of the ion concentrations are small. When the gradients are large, a more general set of flux equations is required. These equations are considerable more complicated than those shown in Equation (14)–(16). Investigation of these equations will be subject of a future paper.

Further, it is noted that the approach described in this paper can be generalised, and an iterative scheme may be developed involving the alternate solution of the macroscale and microscale equations. The advantage of this hierarchical approach is that it is a completely general solution methodology, providing a means for inserting information lost during the homogenization process at selected locations within the domain. The advantage of this scheme is that important non-linear microscale processes that influence macroscale behaviour are included into the analysis, but the problem is kept computationally feasible. While perturbation methods have been successfully applied to identify transport properties (such as the tortuosity) for uncharged porous

media (Auriault and Lewandowska, 1996; Whitaker, 1999; Dormieux and Lemarchand, 2000), this theory has not yet been applied to charged porous media.

3. Numerical Analysis of Electrolyte Diffusion Through a Unit Cell

The example problem analysed here is a two-dimensional spatially periodic unit cell of clay soil saturated with water. The unit cell is taken to be 150 nm wide and 300 nm high. The six clay particles within the unit cell are modelled as identical plates 10 nm in thickness and 100 nm long (such particles may be encountered in montmorillonitic clay (Iwata *et al.*, 1995)). The number of clay particles was chosen such that the porosity of the unit cell ($n = 0.87$) is close to the one used in the experiments conducted by Dutt and Low (1962) and Kemper and van Schaik (1966) (see Table I). The clay platelets are arranged so that there is no obvious preferred orientation of the clay plates (i.e. they are pseudo-randomly oriented, see Figure 1(a)). A Galerkin finite element method is employed to solve the governing equations. Triangular elements with second-order shape functions are used to approximate the trial solution. The mesh employed for all the reported analyses contains of 5056 triangular elements and 2781 nodes (see Figure 1(b)).

This model may represent diffusion across a very thin membrane (or represent transient diffusion at an early time when large concentration gradients occur). While this model offers no special advantage in the investigation of diffusion through an uncharged porous medium (Subsection 3.1), it does offer advantages when the porous medium is charged, as discussed in Subsection 3.3.

The boundary condition for the unit cell were chosen as follows: (i) for the Nernst–Planck Equation (7), concentrations c_1 and c_2 were applied at the upper and lower end of the unit cell, while zero flux was applied through the sides of the unit cell and the solid particles. For investigation of equilibrium states, zero flux was also applied at the lower boundary; (ii) for the Poisson equation (12), voltage boundary conditions (ψ_1 and ψ_2) were prespecified at the upper and lower end of the unit cell. The permanent negative charge in clay crystals was assumed to create a constant surface voltage ψ_s in the millivolt range. At the left and right side of the unit cell electrical insulation symmetry conditions were employed. For investigation of equilibrium states the insulation symmetry condition was also applied to the lower boundary of the unit cell.⁶ For the electric boundary condition study performed in Subsection 3.3, two different cases

⁶It is noted that at least one Dirichlet boundary condition is necessary in order to obtain a unique solution.

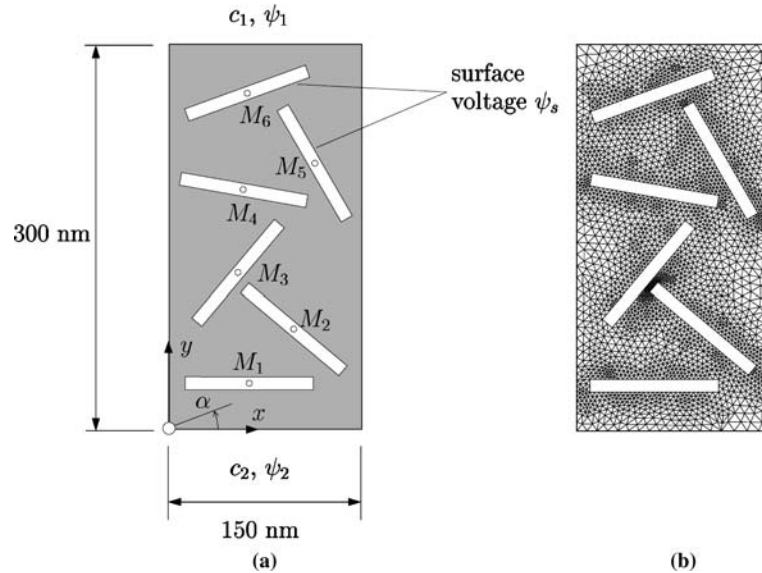


Figure 1. Diffusive transport through a unit cell: (a) geometric dimensions and (b) finite element mesh (mid-point coordinates ($\times 10^{-7}$ m) and rotation angle α : $M_1 = (0.60, 0.35; 0^\circ)$, $M_2 = (0.98, 0.79; -40^\circ)$, $M_3 = (0.55, 1.21; 50^\circ)$, $M_4 = (0.60, 1.86; -10^\circ)$, $M_5 = (1.12, 2.09; -60^\circ)$, $M_6 = (0.59, 2.60; 20^\circ)$).

for the lower boundary condition (ψ_2) were investigated. The first assumed $\psi_1 = \psi_2 = 0$ V, (i.e., allowing no charge to accumulate on either boundary), resulting in an electrical short circuit between the upper and lower boundary. It is noted that practically such an electric short circuit condition can be implemented in the laboratory using a salt bridge. In Subsection 3.3 this case is denoted as the *electric short circuit condition*. The second case involves a boundary condition leading to the nil current condition, given in Equation (11). Assuming a reference voltage ($\psi_1 = 0$ V), ψ_2 can be computed iteratively to satisfy this condition. It is noted that for charged solutes diffusing through soil samples (without applying any external electric field) this condition is the usual one. The voltage difference between the downstream and upstream side of the specimen is commonly referred to as *membrane potential*. The applied boundary condition for all numerical investigations are summarized in Table II. Finally, parameters used for the Nernst–Planck equation are given in Table III.

3.1. STEADY-STATE DIFFUSION OF UNCHARGED SOLUTES

The first case considered is steady-state diffusion of an uncharged solute across the unit cell. The concentration on the upper boundary (c_1) is taken to

Table II. Boundary conditions applied for the numerical analyses

Subsection Nr.	c_1 mol/m ³	c_2 mol/m ³	ψ_1 V	ψ_2 V
3.1	0.001–10	0	– ^a	– ^a
3.2	0.001–10	– ^b	0	– ^c
3.3	0.001–10	0	0	ψ_2 ^d

^a ... uncharged case; ^b ... application of zero flux boundary condition, ^c ... application of insulation symmetry condition; ^d ... $\psi_2 = 0$ for electric short circuit condition or ψ_2 computed to satisfy the nil current condition Equation (11).

Table III. Model parameters used for the numerical analyses

Symbol	Value	Dimension
ϵ_0	8.85×10^{-12}	C ² /(J m)
ϵ_ω	78	–
D_+	1.5×10^{-9}	m ² /s
D_-	1.5×10^{-9}	m ² /s
F	96500	C/mol
T	293	K
R	8.31	J/(K mol)

be 1 mol/m³, and on the lower boundary (c_2) zero (see Table II, Subs. Nr. 3.1 and description of boundary conditions at the beginning of this section). The solute diffusion coefficient is taken to be equal to the salt diffusion coefficient of the anion or cation (see Table III, i.e., $D_{0,\text{solute}} = 1.5 \times 10^{-9} \text{m}^2/\text{s}$).⁷

Figure 2 shows the solute distribution in the unit cell for the applied boundary conditions. Because the solute is uncharged, it is not influenced by surface voltage on the platelets.

The effective diffusion coefficient for the unit cell may be estimated from the mass transfer rate through the unit cell. Volume-averaging (Equation (13)) over the (y -component) of the microscopic flux j_{solute} leads a macroscopic flux as $2.46 \cdot 10^{-3} \text{mol}/(\text{s m}^2)$. Applying Equation (14) and using relation (17) leads to an estimate of the effective diffusion coefficient for the uncharged solute $D_{\text{eff},\text{solute}} = 8.49 \cdot 10^{-10} \text{m}^2/\text{s}$. Knowing the solute free-solution diffusion coefficient (i.e., $D_{0,\text{solute}} = 1.5 \cdot 10^{-9} \text{m}^2/\text{s}$) allows the tor-

⁷ The salt diffusion coefficient of a binary electrolyte is given as (Newman, 1991): $D_{\text{salt}} = D_+ D_- (z_+ - z_-) / (z_+ D_+ - z_- D_-)$.

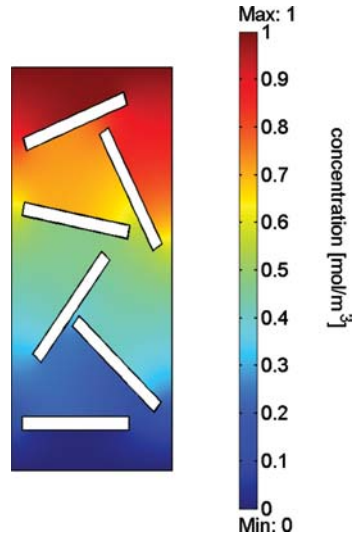


Figure 2. Diffusive transport of an uncharged solute through a platy-clay soil: concentration distribution for $c_1 = 1 \text{ mol/m}^3$ and $c_2 = 0 \text{ mol/m}^3$.

tuosity to be calculated for the uncharged solute as $\tau = D_{\text{eff,solute}}/D_{0,\text{solute}} = 0.56$.

A similar approach has been applied by Dormieux and Lemarchand (2000) in order to compute effective diffusion coefficients for three dimensional unit cells considering spherical and elliptical inclusions, allowing for the investigation of anisotropic effects. Because of the linearity of Fick's first law the size of the domain has no influence on the estimated effective diffusion coefficient, and the effective diffusion coefficient is only a function of the pore geometry (and is independent of the applied concentration gradient). It is mentioned that these findings justify the fundamental assumptions made in perturbation methods, namely, that the boundary conditions chosen for the unit cell or the size of the domain, have no influence on the estimated macroscopic quantity.

3.2. EQUILIBRIUM STATES IN CHARGED POROUS MEDIA

We next consider the equilibrium distribution of ions within the unit cell when the platelets are charged, and calculate the effective porosity ($n_{\text{eff},i}$) for both anions and cations. The experimental method described by Sposito (1989) to estimate the effective porosity is implemented numerically (that is, computing the exclusion volume (Equation (6)) and effective porosity (Equation (5)) for a given set of boundary conditions). In order to establish equilibrium of the system a constant electrolyte concentration $c_1 = c \text{ (mol/m}^3\text{)}$ is applied on the

upper boundary and zero flux on all other boundaries. For the parametric study now undertaken the surface voltage (ψ_s) is assumed to range between -0.01 and -0.05 V while the electrolyte concentration (c) ranges between 0.001 and 10 mol/m³ (see Table II, Subs. Nr. 3.2 and description of boundary condition at the beginning of this section).

The anion and cation distribution for a particular electrolyte concentration $c_l = 1$ mol/m³ with a particular surface voltage at the clay particles of $\psi_s = -0.025$ V is shown in Figure 3. It is clearly apparent that the negative surface voltage results in *exclusion* of anions from the unit cell (note the anion concentration next to the particles is as low as 0.36 mol/m³, see Figure 3(a)). On the other hand, the negative charge on the clay platelets results in *inclusion* of cations within the unit cell (note the cation concentration next to the particle surfaces is as high as 2.71 mol/m³, see Figure 3(b)).

Given the ion distribution for the charged unit cell, Equation. (6) can be applied to compute the exclusion volume V_{ex} and the effective porosity. Figure 4 shows the dependence of the effective porosity of anions and cations on the electrolyte concentration ($c = c_l$) and the surface voltage (ψ_s). Increasing the surface voltage while keeping the electrolyte concentration constant leads to a decrease of the effective porosity of anions ($n_{\text{eff},-}$, see Figure 4(a)) and to an increase of the effective porosity of cations ($n_{\text{eff},+}$, see Figure 4(b)). For the case of high electrolyte concentrations the effective

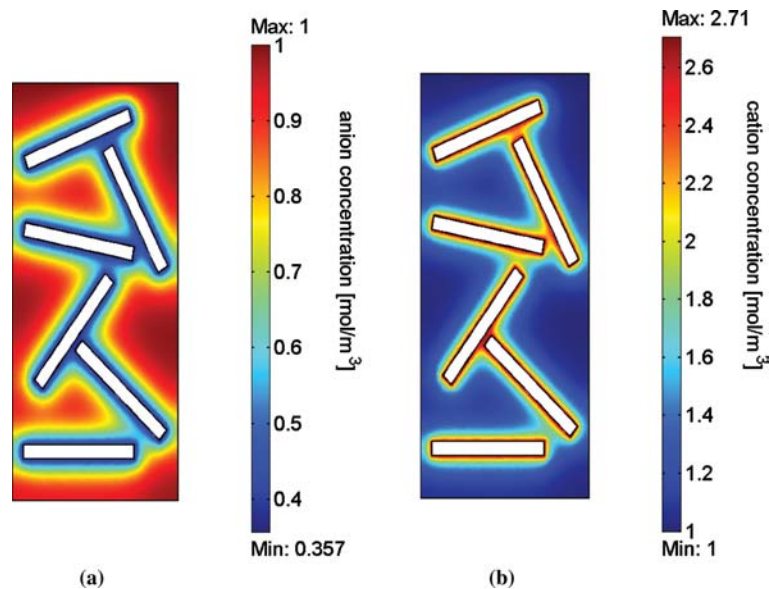


Figure 3. Equilibrium state in a platy-clay soil: concentration of (a) anion and (b) cation ($c_l = 1$ mol/m³ and $\psi_s = -0.025$ V).

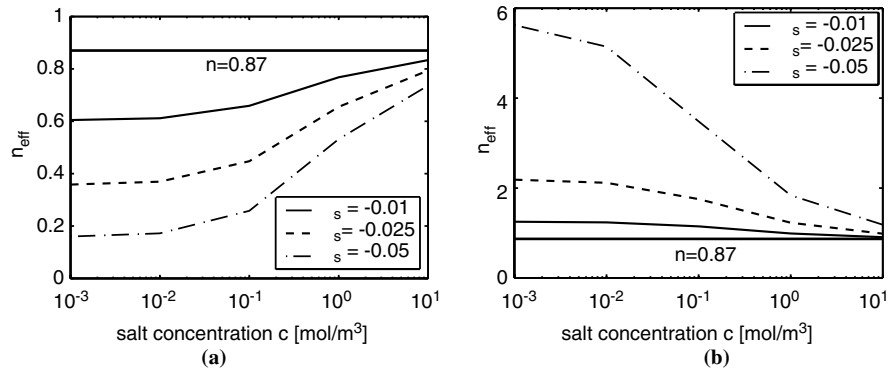


Figure 4. Equilibrium state in a platy-clay soil: dependence of effective porosity on the salt concentration c for (a) anions ($n_{\text{eff},-}$) and (b) cations ($n_{\text{eff},+}$) for various surface voltages ψ_s (semi-logarithmic scale).

porosity of anions and cations converge to the value of the porosity in the uncharged case, i.e., $n = 0.87$ (thick curve in Figure 4).

The influence of electrolyte concentration on the effective porosity of anions and cations can be best explained by looking at the voltage distribution. Figure 5 shows the voltage distribution for $\psi_s = -0.025$ V at

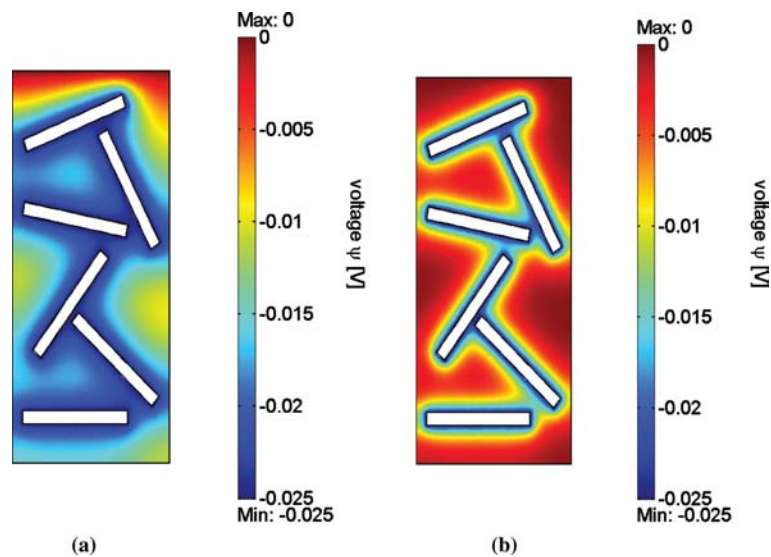


Figure 5. Equilibrium state in a platy-clay soil: voltage distribution for electrolyte concentrations of (a) $c = 0.01$ mol/m³ and (b) $c = 1$ mol/m³ for applied surface voltage $\psi_s = -0.025$ V.

concentrations of $c = 0.01 \text{ mol/m}^3$ and $c = 1 \text{ mol/m}^3$. Comparing the thickness of the electric double-layers, i.e., the (normal) distance from a charged surface at which the voltage reduces to $1/e$ (≈ 0.37) of the surface voltage indicates that for a rather low concentration of $c = 0.01 \text{ mol/m}^3$, the double layer thickness is in the range of 45 nm, while for $c = 1 \text{ mol/m}^3$ the double-layer thickness is only about 10 nm (see Figure 5(a) and (b)). This indicates that increasing the electrolyte concentration leads to a compression of the diffuse double-layer. At very high concentrations the double-layers are highly compressed, hence the effective porosities are almost equal to that for the uncharged case (see Figure 4 for high concentrations).

The numerical results show that the effective porosity strongly depends on the surface voltage on the platelets and on the electrolyte concentration. Thus using a constant effective porosity in Fick's first and/or second law (Equations (1) and (2)) is highly questionable (see arguments in Subsection 1.1). Further, it is noted that the above observations indicate that standard perturbation methods used for up-scaling cannot be used because the properties of the unit cell depend nonlinearly on the boundary conditions applied at the unit cell, thereby invalidating the basic assumption of perturbation theory (see Subsection 2.2).

3.3 STEADY-STATE DIFFUSION OF CHARGED SOLUTES

In this section, steady-state diffusive transport of a binary monovalent electrolyte across the unit cell is investigated. As mentioned previously, this can represent diffusion across a very thin membrane. The advantage of analysing this case is that all effects encountered in charged membranes can be made visually explicit by producing ion distribution maps showing preferential transport pathways, concentration effects on the double layers of the charged particles, and membrane potentials.

We consider two types of boundary conditions for the Poisson equation. First the electric short circuit condition, and second, the nil current condition (see Table II, Subs. Nr. 3.3 and description of boundary conditions at the beginning of this section). We start by investigating the transport behaviour for a particular concentration gradient and surface voltage (i.e., $\Delta c = 1 \text{ mol/m}^3$, $\psi_s = -0.025 \text{ V}$) and then perform a parametric study at the end of this subsection.

Figure 6 shows the voltage distribution and ion map distributions for the cations and anions obtained for the case of an electric short circuit condition.

Comparing the voltage distribution obtained for diffusive transport (Figure 6(a)) with the one obtained for the equilibrium state (Figure 5(b)) indicates a quite different voltage distribution within the unit cell. The thickness of the diffuse double-layer now increases steadily with distance

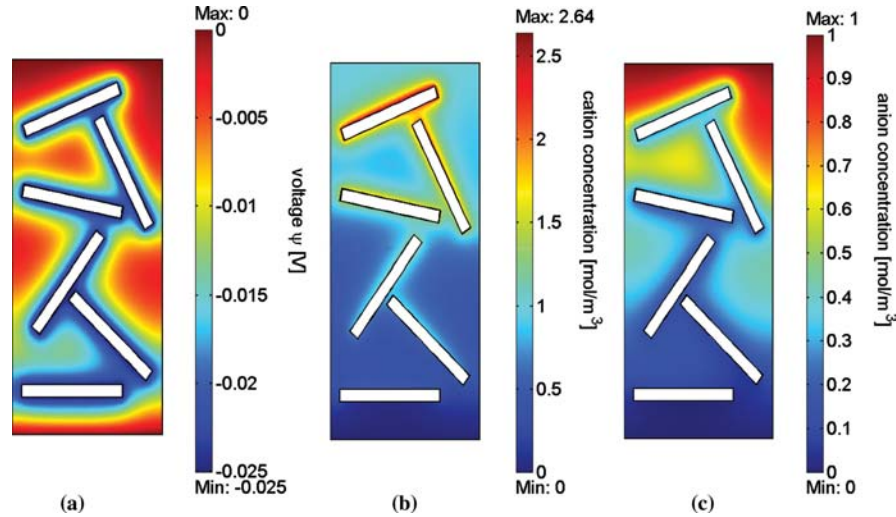


Figure 6. Diffusive transport of binary electrolyte through a platy-clay soil: distribution of (a) voltage, (b) cation concentration, and (c) anion concentration for electric short circuit condition ($\Delta c = 1 \text{ mol/m}^3$, $\psi_s = -0.025 \text{ V}$).

from the top boundary (whereas the concentration of ions in the pore fluid decreases to zero concentration at the bottom boundary). The cation distribution map (Figure 6(b)) clearly indicates that cations are attracted to the negatively charged platelets, and reveals that the diffuse double-layer around the platelets provides a *preferential transport pathway* for the cations. Comparison of the actual cation gradient close to the platelets and the nominal concentration gradient between the boundaries indicates an almost 2.5 fold increase of the concentration gradient (Figure 6(b)). This would suggest that the effective diffusion coefficient of the cations using Fick's first law (1), would be considerable greater than the effective diffusion coefficient for an uncharged solute ($D_{\text{eff,solute}} = 8.49 \cdot 10^{-10} \text{ m}^2/\text{s}$) using the same theory. On the other hand, anions are repelled from the negatively charged clay platelets, serving as a deterrent to the flow of anions (Figure 6(c)).

There is observed to be a very steep anion gradient immediately inside the upper boundary, which greatly reduces the anion gradient over the remainder of the unit cell. This leads to an effective diffusion coefficient for anions much smaller than for an uncharged solute. As mentioned previously, the calculation of effective diffusion coefficients at this stage is not straight forward and so will be the subject of a future paper.

Figure 7 shows the voltage distribution, and ion map distributions of cations and anions obtained by application of the nil current condition.

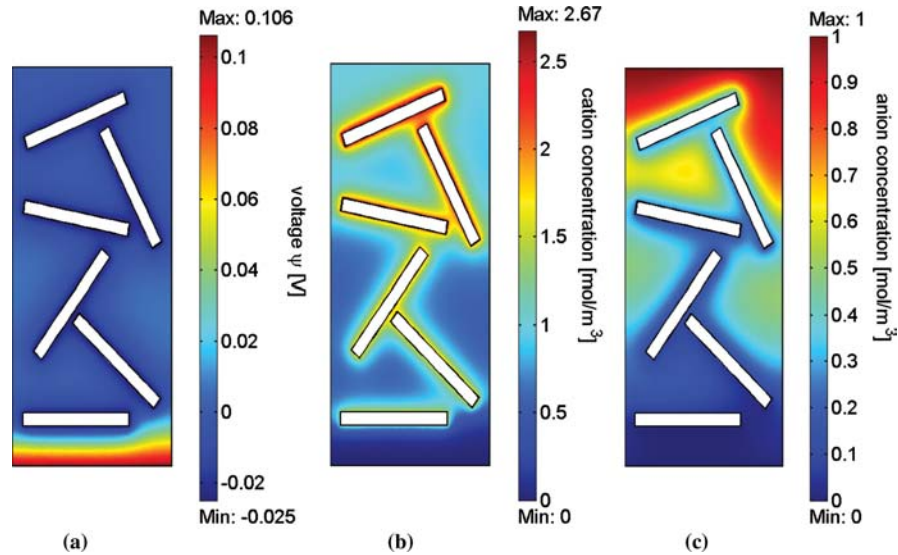


Figure 7. Diffusive transport of binary electrolyte through a platy-clay soil: distribution of (a) voltage, (b) cation concentration, and (c) anion concentration for nil current condition ($\Delta c = 1 \text{ mol/m}^3$, $\psi_s = -0.025 \text{ V}$).

The voltage distribution in the unit cell indicates a sharp voltage change near the lower boundary (see Figure 7(a)). However, this change is restricted to a rather small area near the boundary. The cation distribution clearly shows that the positive voltage on the lower boundary serves to repel cations (i.e., restraining their free exit) across the lower boundary (Figure 7(b)). This *dam effect* serves to increase the cation concentration on all upstream platelets (compare with Figure 6(b): note yellow shading now extends over all platelets). The anion concentration distribution indicates that anions are electrically attracted to the lower boundary by means of the positive voltage, hence anion transport is hastened by this *drag effect* due to the electric field (Figure 7(c)). The nil current requirement enforces the cation and anion flux to be equal (although the transport pathways through the porous medium of cations and anions are different).

Finally, we investigate the dependence of ion fluxes on the concentration gradient and the surface voltage. Figure 8 shows the cation and anion fluxes for the electric short circuit condition and the nil current condition.

For a particular concentration, the electric short circuit condition leads to an increase of the cation flux with increasing surface voltage, whereas the anion flux decreases with increasing surface voltage (Figure 8(a)).

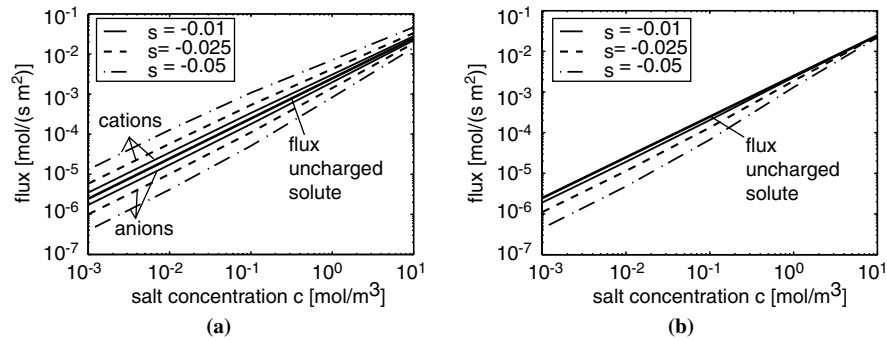


Figure 8. Diffusive transport of binary electrolyte through a platy-clay soil: cation and anion fluxes obtained from (a) electric short circuit condition and (b) nil current condition (double-logarithmic scale).

While the cation fluxes are higher than the flux obtained for an uncharged solute (thick line in Figure 8(a)), the opposite is true for the anions. It is observed that for high concentration gradients (i.e., compressed diffuse double-layers) the fluxes of cations and anions converge to that of the uncharged case. On the other hand, for the nil current condition the fluxes of cations (anions) are smaller than the flux of an uncharged solute (Figure 8(b)). This result is not obvious based on the individual ion behaviour in the electric short circuit condition. The parametric study makes it clear that the nil current condition results in ion fluxes that are much closer to the zero charge flux than either of the individual cation and anion fluxes in the electric short circuit case (i.e. for the nil current condition, the decrease in anion flux is offset against the increase in cation flux).

The dependence of the membrane potential ($\psi_2 - \psi_1$) on the concentration (gradient) and the surface voltage is shown in Figure 9.

The numerical results obtained in this section clearly show that the ion flux, the effective diffusion coefficient, and the membrane potential are functions of the ion concentration gradient and the surface voltage on the clay platelets.

Furthermore, it is noted that these quantities also depend on the size of the domain. These findings indicate that it is impossible to define a single (constant) effective diffusion coefficient (membrane potential) for an ionic species diffusing through a platy-clay soil. Only in the case of high ionic concentration (compressed diffuse double-layers) does the effective diffusion coefficient and the membrane potential become independent of the boundary conditions (i.e., the ion concentration and the surface voltage)

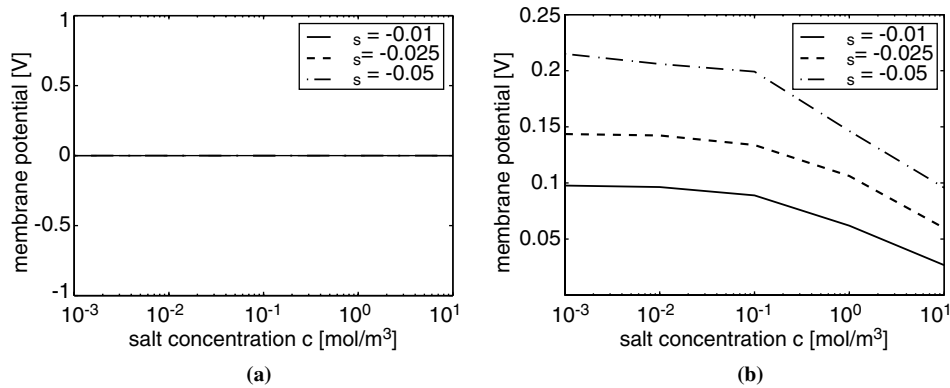


Figure 9. Diffusive transport of binary electrolyte through a platy-clay soil: membrane potentials obtained from (a) electric short circuit condition and (b) nil current condition (semi-logarithmic scale).

and the size of the domain. For this special situation use of a constant effective diffusion coefficient is justified.

4. Summary and Conclusions

From the numerical results obtained on the basis of the Nernst–Planck and Poisson system of equations applied to a unit cell the following conclusions can be made:

- (1) The concept of using effective porosity based on anion exclusion combined with a standard diffusion analysis (i.e. using Fick's first law) has been shown to be of little value in the interpretation of diffusive transport quantities of charged solutes through a charged porous medium. Even in the short circuit case, the distribution of ions within the diffuse double-layer is a function of the pore fluid composition, and so the estimated effective porosity of the charged porous medium is a function of the boundary conditions (i.e., the surface voltage ψ_s and the background electrolyte concentration c). Though not discussed in the example problem, the effective porosity will also be a function of the permittivity of the solvent and the valence of the ions in solution.
- (2) For uncharged solutes, the estimation of effective diffusion coefficients was found to depend only on the pore space geometry, and so is independent of the boundary conditions and size of the unit cell. On the other hand, for charged solutes diffusing through a charged porous medium, the effective diffusion coefficient strongly depends on the electrolyte

concentration and the particle surface voltage. These findings indicate that an effective diffusion coefficient employed in Fick's first law is system specific, and so this parameter is more properly considered an effective mass transfer coefficient. It has also been shown that in the case of high electrolyte concentrations the influence of the surface voltage becomes less pronounced because of the compression of the diffuse double-layer. Only for this special case is the concept of effective diffusion coefficients useful.

- (3) Application of the microscale governing equations allows the calculation of mass transfer properties of a charged porous medium based on diffusion coefficients. This approach can be practically employed at the microscale to reveal the behaviour of a unit cell. By means of this approach, detailed ion distribution maps have afforded important new insights into ionic transport through a charged platy-clay soil at the nanoscale. These maps have revealed a *dam effect* and a *drag effect*, both arising from charge accumulation on one side of a barrier membrane. It has been noted that modelling the complete macroscopic system using the microscale equations is for practical purposes currently unachievable. To make this problem tractable, it has been suggested that a hierarchical modelling approach can be employed.

Finally it is concluded that the mass transfer of ions through a charged porous medium cannot be simply represented by the same formalism as that adopted for the transport of an uncharged solute through a porous medium. The theory presented here allows for a detailed understanding of microscale ion transport, and provides for the first time, a detailed picture of ion transport through a charged porous medium. However, further experimental and theoretical investigations of ion transport through charged porous media are warranted for a more complete understanding of the system behaviour. Of particular interest are the macroscopic field equations in the presence of large concentration gradients, the effect of viscosity changes in the pore fluid close to the particle surface, the influence of advective transport, the generalization of the model to three spatial dimensions, and the development of a hierarchical modelling approach.

Acknowledgements

The finite element modelling reported here was performed using the multi-physics software package FEMLAB, while the research was supported by the Australian Research Council. The second author gratefully acknowledges the financial support of this study by the Austrian Foundation for the Promotion of Scientific Research (FWF) in the course of an Erwin Schrödinger scholarship.

Appendix: Notation

The following notation is used in this paper.

c_i	= concentration of ions in pore solution in mol/m ³
c_1, c_2	= electrolyte concentration on upstream and downstream side in mol/m ³
\bar{c}_i	= concentration of ion i in clay soil without permanent charge in mol/m ³
$D_{\text{eff},i}$	= effective diffusion coefficient of ion i in m ² / s
D_i	= apparent diffusion coefficient of ion i in m ² / s
\mathbf{D}_i	= second order apparent (i.e., homogenized) diffusion tensor of ion i (coefficients in m ² / s)
$D_{\text{poresol},i}$	= ion diffusion coefficient of pore solution in m ² / s
D_{salt}	= salt diffusion coefficient in m ² / s
$D_{\text{solid},i}$	= ion diffusion coefficient of solid phase of the soil in m ² / s
$D_{\text{surface},i}$	= surface diffusion coefficient in m ² / s
$D_{0,i}$	= self-diffusion coefficient of ion i in m ² / s
$D_{0,-}, D_{0,+}$	= self-diffusion coefficient of anion and cation in m ² / s
$D_{0,\text{solute}}$	= self-diffusion coefficient of uncharged solute in m ² / s
F	= Faraday constant in C/mol
\mathbf{i}	= current density in C/(m ² s)
\mathbf{j}_i	= molar mass flux density of ion i in pore solution of the soil in mol/(m ² s)
n	= total porosity of soil
n_{eff}	= effective porosity of soil
$n_{\text{eff},-}, n_{\text{eff},+}$	= effective anion and cation porosity of soil
R	= universal gas constant in J/(K mol)
t	= time variable in s
T	= absolute temperature in K
$V_f; V_s; V_T$	= volumes of the fluid phase, the solid phase, and the total volume of soil in m ³
V_{ex}	= excluded/included volume of the anion/cation in m ³
X	= fixed charge concentration mol/m ³
x, y	= spatial coordinates in m
z_i	= valence of ion i
ϵ	= permittivity of the medium in C ² /(J m)
ϵ_{app}	= apparent (or soil) permittivity in C ² /(J m)
ϵ_w	= relative permittivity of water (dimensionless)
ϵ_0	= permittivity of free space in C ² /(J m)
ψ	= voltage in V
ψ_s	= surface voltage on charged particles in V
ψ_1, ψ_2	= voltage applied on upstream and downstream side in V
τ	= tortuosity factor of uncharged solutes (dimensionless)

τ_i	= tortuosity factor of charged solutes in charged porous media (dimensionless)
ω	= sign of fixed charge concentration X
$\langle \cdot \rangle$	= macroscopic (volume averaged) quantities

References

- Appelt, H., Holtzclaw, K. and Pratt, P. F.: 1975, Effect of anion exclusion on the movement of chloride through soils, *Soil Sci. Soc. Am. Proc.* **39**, 264–267.
- August, H., Holzlohner, U. and Meggyes, T.: 1997, *Advanced Landfill Liner Systems*, Thomas Telford, New York, USA.
- Auriault, J. L. and Lewandowska, Y.: 1996, Diffusion/adsorption/advection macrotransport in soils, *Eur. J. of Mech. A/Solids* **15**(4), 681–704.
- Barone, F. S., Rowe, R. K. and Quigley, R. M.: 1992, A laboratory estimation of chloride diffusion and adsorption coefficients for several volatile organics in a natural clayey soil, *J. Contam. Hydro.* **10**, 225–250.
- Barracough, P. B. and Tinker, P. B.: 1981, The determination of ionic diffusion coefficients in field soils. I. diffusion coefficients in sieved soils in relation to water content and bulk density, *J. Soil Sci.* **32**, 225–236.
- Bear, J. and Bachmat, Y.: 1991, *Introduction to Modelling of Transport Phenomena in Porous Media*, Vol. 4. Kluwer Academic Publishers, Dordrecht, The Netherlands.
- Berry, J. A. and Bond, K. A.: 1992, Experimental investigation of radionuclide diffusion on site-specific sediment/groundwater systems, *Radiochim Acta* **58/59**, 329–335.
- Bond, W. J., Gardiner, B. N. and Smiles, D. E.: 1982, Constant flux adsorption of tritiated calcium chloride solution by a clay soil with anion exclusion, *Soil Sci. Soc. Am. J.* **46**, 1133–1137.
- Bresler, E.: 1973, Anion exclusion and coupling effects in nonsteady transport through unsaturated soils: I. theory, *Soil Sci. Soc. Am. Proc.* **37**, 663–669.
- Clarke, A. L. and Graham, E. R.: 1968, Zinc diffusion and distribution coefficients in soil as affected by soil texture, zinc concentration and pH, *Soil Sci.* **105**(6), 409–418.
- Crooks, V. E. and Quigley, R. M.: 1984, Saline leachate migration through clay: a comparative laboratory and field investigation, *Can. Geotech. J.* **21**, 349–362.
- Cussler, E. L.: 1997, *Diffusion Mass Transfer in Fluid Systems*, Cambridge University Press, New York, USA, 2nd edn.
- Day, S. R. and Daniel, D. E.: 1985, Hydraulic conductivities of two prototype clay liners, *ASCE J. Geotech. Eng.* **111**(8), 957–970.
- Desaulniers, D. E., Cherry, D. E. and Fritz, P.: 1981, Origin, age and movement of pore water in clayey pleistocene deposits in South Central Canada, *J. Hydro.* **50**, 231–257.
- Dormieux, L. and Lemarchand, E.: 2000, Modélisation macroscopique du transport diffusif: apport des méthodes de changement d'échelle d'espace, *Oil and Gas – Revue de l'Institut Français Pétrol* **55**(1), 15–34.
- Dormieux, L. and Lemarchand, E.: 2001, Homogenization approach of advection and diffusion in cracked porous media, *ASCE J. Eng. Mech.*, **127**(12), 1267–1274.
- Dutt, G. R. and Low, P. F.: 1962, Diffusion of alkali chlorides in clay–water systems. *Soil Sci.* **47**, 233–240.
- Gillham, R. W., Robin, M. J. L. and Dytynshyn, D. J.: 1984, Diffusion of nonreactive and reactive solutes through fine-grained barrier materials, *Can. Geotech. J.* **21**, 541–550.

- Ichikawa, Y., Kawamura, K., Fujii, N. and Nattavut, T.: 2002, Molecular dynamics and multiscale homogenization analysis of seepage/diffusion problem in bentonite clay, *Int. J. Numer. Meth. Eng.* **54**, 1717–1749.
- Iwata, S., Tabuchi, T. and Warkentin, B. P.: 1995, *Soil–water interactions*. Marcel Dekker, New York, USA.
- James, R. V. and Rubin, J.: 1986, Transport of chloride in a water-unsaturated soil exhibiting anion exclusion, *Soil Sci. Soc. Am. J.* **50**, 1142–1149.
- Kato, M.: 1995, Numerical analysis of the Nernst–Planck–Poisson system, *J. Theor. Biol.* **177**, 299–304.
- Kemper, W. D. and van Schaik, J. C.: 1966, Diffusion of salts in clay–water systems, *Soil Sci. Soc. Am. Proc.* **30**, 534–540.
- Kozaki, T., Inada, K., Sato, S. and Ohashi, H.: 2001, Diffusion mechanism of chloride ions in sodium montmorillonite, *J. Contam. Hydro.* **47**, 159–170.
- Macgillivray, A.: 1968, Nernst–Planck equations and the electroneutrality and Donnan equilibrium assumptions, *J. Chem. Phys.* **48**, 2903–2907.
- Mitchell, J. K.: 1993, *Fundamentals of Soil Behavior*, John Wiley & Sons, New York, USA, 2nd edn.
- Newman, J. S.: 1991, *Electrochemical Systems*, Prentice-Hall, Englewood Cliffs, NJ, USA, 2nd edn.
- Quigley, R. M., Crooks, V. E. and Fernandez, F.: 1984, Engineered clay liners (an overview report), in *Seminar on the Design and Construction of Municipal and Industrial Waste Disposal Facilities*, Toronto, Ontario, Canada.
- Quintard, M. and Whitaker, S.: 1993, Transport in ordered and disordered porous media V: geometrical results for two dimensional systems, *Trans. Porous Media* **15**, 183–196.
- Revil, A.: 1999, Ionic diffusivity, electrical conductivity, membrane and thermoelectric potentials in colloids and granular porous media: a unified model, *J. Colloid Interface Sci.* **212**, 503–522.
- Robin, M. J. L., Gillham, R. W. and Oscarson, D. W.: 1987, Diffusion of strontium and chloride in compacted clay-based materials, *Soil Sci. Soc. Am. J.* **51**, 1102–1108.
- Rowe, R. K.: 1998, Geosynthetics and the minimization of contaminant migration through barrier systems beneath solid waste, in *6th International Conference on Geosynthetics*, pp. 27–102, Atlanta, USA.
- Rowe, R. K.: 2001, *Geotechnical and Geoenvironmental Engineering Handbook*. Kluwer Academic Publishers, Dordrecht, The Netherlands.
- Rowe, R. K. and Booker, J. R.: 1984, The analysis of pollutant migration in a non-homogeneous soil, *Geotechnique* **34**(4), 601–612.
- Rowe, R. K., Caers, C. J. and Barone, F.: 1988, Laboratory determination of diffusion and distribution coefficients of contaminants using undisturbed soil, *Can. Geotech. J.* **25**, 108–118.
- Rowe, R. K., Quigley, R. M. and Booker, J. R.: 1995, *Clayey Barrier Systems for Waste Disposal Facilities*, London, E & FN Spon., Melbourne, Australia.
- Samson, E., Marchand, J. and Beaudoin, J. J.: 1999, Describing ion diffusion mechanisms in cement-based materials using the homogenization technique, *Cement Concr. Res.* **29**, 1341–1245.
- Sen, P. N.: 1989, Unified model of conductivity and membrane potential of porous media. *Phys. Rev. B* **39**(13), 9508–9517.
- Shackelford, C. D.: 1988, *Diffusion of Inorganic Chemical Wastes in Compacted Clay*. PhD thesis, University of Texas, Austin, Texas, USA.
- Shackelford, C. D. and Daniel, D. E.: 1991a, Diffusion in saturated soil. I: background. *ASCE J. Geotech. Eng.* **117**(3), 467–484.

- Shackelford, C. D. and Daniel, D. E.: 1991b, Diffusion in saturated soil. II: results for compacted clay, *ASCE J. Geotech. Eng.* **117**(3), 485–506.
- Shukla, M. K., Klepsch, S. and Loiskandl, W.: 1999, Miscible displacement in porous media: theoretical evaluation, *Die Bodenkultur* **50**(2), 93–108.
- Sposito, G.: 1989, *The Chemistry of Soils*, Oxford University Press, New York, USA.
- Thomas, G. W. and Swoboda, A. R.: 1970, Anion exclusion effects on chloride movement in soils, *Soil Science*, **110**(3), 163–166.
- Whitaker, S.: 1999, *The Method of Volume Averaging*, Vol. 13. Kluwer Academic Publishers, Dordrecht, The Netherlands.

P. Pivonka and D. Smith. Investigation of nanoscale electrohydrodynamic transport phenomena in charged porous materials. *International Journal for Numerical Methods in Engineering*, **63**, pp 1975-1990, 2005.

Investigation of nanoscale electrohydrodynamic transport phenomena in charged porous materials

P. Pivonka^{*,†} and D. Smith

*Department of Civil and Environmental Engineering, The University of Melbourne,
Parkville, Victoria 3010, Australia*

SUMMARY

Depending on the permeability of porous materials, different mass transport mechanisms have to be distinguished. Whereas mass transport through porous media characterized by low permeabilities is governed by diffusion, mass transport through highly permeable materials is governed by advection. Additionally a large number of porous materials are characterized by the presence of surface charge which affects the permeability of the porous medium. Depending on the ion transport mechanism various phenomena such as co-ion exclusion, development of diffusion–exclusion potentials, and streaming potentials may be encountered. Whereas these various phenomena are commonly described by means of different transport models, a unified description of these phenomena can be made within the framework of electrohydrodynamics.

In this paper the fundamental equations describing nanoscale multi-ion transport are given. These equations comprise the generalized Nernst–Planck equation, Gauss’ theorem of electrostatics, and the Navier–Stokes equation. Various phenomena such as the development of exclusion potentials, diffusion–exclusion potentials, and streaming potentials are investigated by means of finite element analyses. Furthermore, the influence of the surface charge on permeability and ion transport are studied in detail for transient and steady-state problems. The nanoscale findings provide insight into events observed at larger scales in charged porous materials. Copyright © 2005 John Wiley & Sons, Ltd.

KEY WORDS: electrohydrodynamic transport; Nernst–Planck equation; Navier–Stokes equation; Gauss’ theorem; diffuse double-layer

1. INTRODUCTION

It is well known that the permeability of a large number of porous materials is not only dependent on the pore morphology (i.e. the porosity and the tortuosity), but also dependent on

*Correspondence to: Peter Pivonka, Department of Civil and Environmental Engineering, The University of Melbourne, Parkville, Victoria 3010, Australia.

†E-mail: ppivonka@unimelb.edu.au

Contract/grant sponsor: Austrian Foundation for the Promotion of Scientific Research

Received 21 June 2004

Revised 6 October 2004

Accepted 14 October 2004

the concentration of ions in the pore fluid saturating the porous space, and the permittivity of the pore fluid [1, 2]. This phenomenon is typical for porous media including clays, shales, polymer gels, and biological tissues [3]. An important property of these materials is the positive/negative charge of their surface. In the case of clay minerals, negative surface charges are often a consequence of isomorphous substitutions of certain atoms in the clay crystal lattice and the presence of crystal imperfections (defects or broken bonds) [4, 5]. The presence of surface charge leads to formation of a diffuse double-layer characterized by high concentrations of anions or cations (depending on the sign of the surface charge) close to the charged surface. Importantly, in the presence of a diffuse double-layer the dissipation of energy in a flowing fluid is not only due to friction within the pore fluid, but also due to friction of the pore fluid and the ions 'pinned' in the diffuse double-layer by means of electrical forces [6].

In this paper the fundamental partial differential equations describing nanoscale multi-ion transport are given in the framework of electrohydrodynamics (Section 2). We seek to explain various phenomena such as the experimentally observed co-ion exclusion, development of diffusion–exclusion potentials, development of streaming potentials and the dependence of the permeability on the concentration of background electrolyte and on the surface charge density. We will do this by formulating a set of governing equations for fluid flow (generalized Navier–Stokes equation) and the transport of individual ions in solution (generalized Nernst–Planck equation), while at the same time including development of diffuse double-layers, i.e. relating the variation of the electric potential to the spatial distribution of the electric charges (using Gauss' theorem of electrostatics). The diffuse double-layer will be coupled to the fluid transport by a body force term in the generalized Navier–Stokes equation. This system of equations will be solved for monovalent binary electrolytes for two mass transport problems (Section 3). The first problem deals with 2D transient fluid flow through semipermeable membranes (Section 3.1). The second problem investigates 2D steady-state ion transport through a charged slit opening (Section 3.2). Using the proposed model, a better insight into the behaviour of clay soils may be gained. For this problem, phenomena such as co-ion exclusion, development of diffusion–exclusion potentials, development of streaming potentials, and the influence of electrolyte concentration and surface charge on fluid flux are investigated. Numerical results are compared with analytic formulas where possible.

2. GOVERNING TRANSPORT EQUATIONS

The key constitutive equation describing nanoscale multi-ion transport in the presence of electrochemical forces is the generalized Nernst–Planck (G–N–P) equation [7]

$$\mathbf{j}_i = -D_i \left(\nabla c_i + \frac{F}{RT} c_i z_i \nabla \psi \right) + \mathbf{v}_f c_i \quad (1)$$

where \mathbf{j}_i , c_i , and ∇c_i is the mass flux density, the concentration of the i th ion, and the concentration gradient of the i th ion in the solvent, respectively. D_i is the free-solution diffusion coefficient of the i th ion.[‡] The quantities z_i and $\nabla \psi$ are the valence of the i th ion and the

[‡]There are several refinements that may be incorporated in the estimated diffusion coefficient, for example, taking into account the activity of the ions in solution (arising from correlated spatial movements/arrangements of ions, see Reference [7] for details).

voltage gradient. \mathbf{v}_f is the fluid velocity and F , R , and T are the Faraday constant, gas constant, and absolute temperature, respectively.

The first term inside the brackets results in transport of the i th ion species along minus of the chemical potential gradient (assuming an ideal solution). The second term inside the brackets results in transport along the voltage gradient.[§] The generalized N–P Equation (1) is a generalization of Fick's law, taking into account electrical effects on charged solutes, and taking into account the movement of the fluid. The voltage ψ appearing in Equation (1) is made up of two distinct parts. The first part of the voltage arises from any external potential applied to the system (for example, the external voltage may result from the accumulation of excess ions on one side of a clay barrier membrane). The second part of the voltage arises from the potential generated by the diffusion coefficients of the individual ions being different, leading to the formation of ion-pair dipoles. This second potential is known as the diffusion potential. However, the ions in solution are influenced by the electric potential irrespective of its origin, so the two voltages arising from either process may be summed and represented by a single ψ .

The G–N–P Equations (1) are supplemented by mass conservation equations. Mass conservation for each conservative ion species is expressed by

$$\frac{\partial c_i}{\partial t} = -\nabla \cdot \mathbf{j}_i \quad (2)$$

where $\nabla \cdot \mathbf{j}_i$ is the divergence of the flux vector of the i th ion and t is the time. Substitution of Equation (1) into the mass conservation Equation (2) leads the governing partial differential equation for mass transport. The variation of electric potential is related to the spatial distribution of the electric charges by means of Gauss' electrostatic theorem (for a system consisting of N ions)

$$\nabla(\varepsilon \nabla \psi) = F \sum_{i=1}^N z_i c_i \quad (3)$$

where the permittivity ε is the product of the permittivity of free space, ε_0 , and the permittivity of water, ε_w , relative to the permittivity of free space, i.e. $\varepsilon = \varepsilon_0 \varepsilon_w$. It should be noted that Gauss' electrostatic theorem is also commonly referred to as Poisson equation of electrostatics. Equations (1)–(3) can be employed in order to gain information on the structure of the diffuse double-layer (DDL) for any ion composition of the pore fluid and solid geometry. Description of the DDL by means of combining the G–N–P Equation (1) and the Poisson equation (3) is commonly referred to as Gouy–Chapman model of the DDL. Further, these equations are suitable for the analysis of ion diffusion through a charged porous medium containing a stationary fluid, i.e. $\mathbf{v}_f = \mathbf{0}$ (see, e.g. Reference [8]). For these reasons, it is clear that the equations constitute a very powerful model, and can solve many problems dealing with colloidal domain processes and the chemomechanical behaviour of clays. Use of the Poisson equation (3) assumes ions are represented as point charges. It was recognized that this assumption considerably overestimates surface concentrations obtained by the Gouy–Chapman model of the diffuse double-layer described above (see e.g. References [5, 9, p. 94]). Rather than to introduce a *hydration potential*, a phenomenological 'correction term' may be applied to either

[§]Note that the direction of transport depends on the valence z_i of the ion.

the concentration or the electrical potential in the G–N–P Equation (1). Here, we have chosen to modify the electrical potential in the G–N–P Equation (1)

$$\mathbf{j}_i = -D_{i,0} \left(\nabla c_i + \frac{F}{RT} c_i z_i \exp(-c_i/k_0) \nabla \psi \right) + \mathbf{v}_f c_i \quad (4)$$

where k_0 represents a hydration parameter (which may be calibrated from concentration measurements near the particle surfaces). In the limit case of $k_0 \rightarrow \infty$ Equation (4) returns the G–N–P Equation (1). The finite size of ions (represented by k_0) limits the maximum concentrations of ions close to the particle surface.

For systems characterized by movement of the pore fluid (i.e. $\mathbf{v}_f \neq \mathbf{0}$), an additional equation describing the fluid flow is required. In this case, there are couplings between the flow of fluid in the pore spaces and the movement of ions in the pore fluid (e.g. as occurs in clay soils or in charged biological tissues). When pore fluid motion occurs relative to the counterions[¶] in the pore fluid, there is initially a drift of counterions in the direction of fluid flow. However soon after this drift begins, large electrical and chemical forces come into play, effectively ‘pinning’ the counterions in solution.^{||} The counterions pinned in pore fluid can contribute significantly to the dissipation of energy in the fluid (the counterions can be imagined to be small spheres suspended in the fluid, interrupting the flow). In clay soils with a high cation exchange capacity, this mechanism may be the principal means for energy dissipation during fluid flow (see first example in Section 3). Assuming no source or sink is present, the governing equations required for the analysis of this system are the continuity equation [10]

$$\nabla \cdot \mathbf{v}_f = 0 \quad (5)$$

and the generalized Navier–Stokes (G–N–S) equation describing electrohydrodynamic flow ([11, p. 553]),**

$$\rho_f \left(\frac{\partial \mathbf{v}_f}{\partial t} + \mathbf{v}_f \cdot \nabla \mathbf{v}_f \right) = \mathbf{F}_m + \mathbf{F}_e + \mathbf{F}_\mu + \mathbf{F}_g \quad (6)$$

where ρ_f is the fluid density. \mathbf{F}_m , \mathbf{F}_e , \mathbf{F}_μ , and \mathbf{F}_g are force vectors of mechanical, electrical, viscous, and gravitational origin. These forces can be expressed for an incompressible homogeneous fluid as

$$\mathbf{F}_m = -\nabla p \quad (7)$$

$$\mathbf{F}_e = qE + \nabla \left(\rho_f \frac{E^2}{2} \left(\frac{\partial \varepsilon}{\partial \rho_f} \right)_\theta \right) - \frac{E^2}{2} \nabla \varepsilon \quad (8)$$

$$\mathbf{F}_\mu = \mu_f \nabla^2 \mathbf{v}_f \quad (9)$$

$$\mathbf{F}_g = \rho_f \mathbf{g} \quad (10)$$

p denotes the fluid pressure in the pore fluid within the porous medium, μ_f is the fluid viscosity. θ is the temperature. $q = F \sum z_i c_i$ is the net charge and $E = -\nabla \psi$ is the electric

[¶]Counterions are the ions required to maintain electroneutrality of the charged clay particles.

^{||}The counterions are pinned in a spatial location in a time-averaged sense (there are thermally induced fluctuations about the mean position).

**Use of the G–N–S equation assumes $\rho_f = \text{const}$ and $\mu_f = \text{const}$, though these restrictions may be relaxed.

field strength. Ignoring electrostriction (i.e. the second term on the RHS of Equation (8)) and the gradient of permittivity in the electrical force Equation (8), for a strong ionic salt this equation becomes

$$\mathbf{F}_e = qE = -F \sum_{i=1}^N z_i c_i \nabla \psi \quad (11)$$

Considering the G–N–S Equation (6), in the case of zero fluid velocity, identifies ‘hydrostatic pressures’ arising from ‘electrical body forces’ [12]. However, this ‘hydrostatic pressure’ is misleading terminology, as it is in fact a thermodynamic pressure arising from the entropic contribution to the free energy of the water due to the presence of the solute in the solvent. The ‘electrical body forces’ can be transformed (using Gauss’ theorem) to Maxwell stresses. But once again the terminology is misleading. The Maxwell stresses do not contribute to a change in pressure in the fluid, but represents stored electrical energy (that changes the free energy of the solvent). We would like to remove this thermodynamic pressure from the G–N–S Equation (6).

In the case of hydrostatic pressure arising from gravitational forces, this may be removed by simply neglecting the gravitational body force in the G–N–S Equation (6). For the thermodynamic pressure, it is less obvious what can be done. However it may be noticed that at equilibrium, the G–N–P Equation (1) is satisfied and the ion fluxes are zero. It can now be seen that the thermodynamic pressure may be removed (for $\mathbf{v}_f = \mathbf{0}$) by introducing a ‘diffusive body force’ that is equal and opposite to the electrical body force (11), that is

$$\mathbf{F}_e = - \sum_{i=1}^N (RT \nabla c_i + z_i F c_i \nabla \psi) = - \sum_{i=1}^N \frac{z_i c_i (\mathbf{v}_f - \mathbf{v}_i)}{u_i} \quad (12)$$

where \mathbf{v}_i is the velocity of the i th ion and u_i denotes the ion mobility. The mobility (u_i) of an ion is linked to the free-solution diffusion coefficient (D_i) by the Nernst–Einstein relation, i.e., $u_i = D_i/(RT)$.

It is noted that the modified Equation (12) is rather fortuitous, in that it accounts for both electrical and chemical forces, and so is a generalization of Equation (11). It will be shown that this generalized equation is necessary for the investigation of coupled fluid flow and diffusion through uncharged and charged porous media (see for example problem 1 in Section 3).

The total power (energy/time) dissipated per unit volume of fluid in this system is the sum of the power dissipated due to fluid viscosity and the power dissipated by friction between the pore fluid the counterions ‘pinned’ in the fluid.^{††} For two-dimensional flow the power dissipated due to fluid viscosity is given by [10]

$$\mathcal{P}_\mu = \mu_f \left(2 \left(\frac{\partial v_1}{\partial x} \right)^2 + 2 \left(\frac{\partial v_2}{\partial y} \right)^2 + \left(\frac{\partial v_1}{\partial y} + \frac{\partial v_2}{\partial x} \right)^2 \right) \quad (13)$$

while the power dissipated due to the counterions pinned in the pore fluid under steady-state conditions is given by (ions fixed in position)

$$\mathcal{P}_e = \frac{c_i (\mathbf{v}_f)^2}{u_i} \quad (14)$$

^{††}The energy dissipated in the fluid must be equal to the rate of work done on the system by pressure–volume work on the system boundaries.

Finally the power dissipated under transient conditions by counterions pinned in the pore fluid is given by (ions moving)

$$\mathcal{P}_e = \sum_{i=1}^N \frac{u_i}{c_i} (RT \nabla c_i + z_i F c_i \nabla \psi)^2 = - \sum_{i=1}^N \frac{z_i c_i (\mathbf{v}_f - \mathbf{v}_i)^2}{u_i} \quad (15)$$

2.1. Origin of the governing equations

Consider a mole of ions being transported along an electro-chemical potential gradient in a liquid. Under steady conditions there is a force balance. The *driving force* acting on the ion must equal the *drag force* acting on the ion arising from the interaction of the ion with the liquid (inertial forces are neglected). As ion transport velocities are very small, it may be assumed that the drag force is proportional to the relative velocity of the ion in the liquid. In this case

$$\text{drag force per mol} = \mathcal{F}_D = \frac{\mathbf{v}_f - \mathbf{v}_i}{u_i} \quad (16)$$

where \mathbf{v}_f and \mathbf{v}_i are the fluid velocity and ion velocity, respectively. The driving force on the ion is given by the sum of the chemical and electrical forces, that is

$$\text{driving force per mol} = \mathcal{F} = -(\nabla \mu_i + F z_i \nabla \psi) \quad (17)$$

where μ_i denotes the chemical potential of the i th ion. Requiring force equilibrium (i.e. $\mathcal{F}_D + \mathcal{F} = 0$), and rearranging terms leads the velocity of the i th ion as

$$\mathbf{v}_i = -u_i (\nabla \mu_i + F z_i \nabla \psi) + \mathbf{v}_f \quad (18)$$

If the driving force acting on the ion is zero (or stating an equivalent condition, if the ion velocity and the pore fluid velocity are zero), then

$$\nabla \mu_i = -F z_i \nabla \psi \quad (19)$$

Now by definition, the ion flux is equal to [7]

$$\mathbf{j}_i = c_i \mathbf{v}_i \quad (20)$$

Assuming an ideal solution, the gradient of the chemical potential can be expressed as

$$\nabla \mu_i = \frac{RT}{c_i} \nabla c_i \quad (21)$$

Substituting the expression for the ion velocity (18) into Equation (20) and use of the Nernst-Einstein relation together with Equation (21) leads the generalized Nernst-Planck Equation (1).

3. NUMERICAL SIMULATIONS

In this section the consequences of the proposed theory will be demonstrated by two example problems. The set of coupled partial differential equations will be solved numerically using the finite element method (FEM).

Table I. Model parameters used for the numerical analyses.

Symbol	Value	Dimension
ε_0	8.85×10^{-12}	$C^2/(J\ m)$
ε_w	78	—
D^+	1.5×10^{-9}	m^2/s
D^-	1.5×10^{-9}	m^2/s
F	96500	C/mol
T	293	K
R	8.31	J/(K mol)
μ_f	0.001	kg/(m s)
ρ_f	1000	kg/m ³
k_0	2500	—

The first problem deals with N–S flow of an uncharged species through a semipermeable membrane. This example demonstrates how concentration gradients accounted for in the generalized force term (Equation (12)) influence fluid flow. The second problem investigates the influence on fluid flow of a charged slit opening containing an electrolyte. Parameters used for the coupled G–N–S Equation (6), G–N–P Equation (4), and the Poisson Equation (3) are given in Table I. It should be noted that material parameters chosen for the nanoscale numerical simulations are very sensitive with respect to the size of the problem. According to References [13, 14] the viscosity of water strongly increases in the vicinity of charged surfaces of the material (e.g. surfaces of clay-mineral particles). However, what can also be seen from theoretical findings [13] and more recently from molecular dynamic simulations [14] this change of material properties is essentially confined to a very thin layer (0.5–1 nm) next to the particle surfaces, depending on the surface charge density and the background concentration of ions in solution. Considering the chosen geometric dimensions (i.e. 10×20 nm for the first problem and 10×150 nm for the second problem, together with a relatively low surface charge density) we estimate the error made by assuming a constant viscosity might range between 1 and 5%. However, for geometric dimensions in the size of the Debye-length, a more refined model using a viscosity depending, e.g. as proposed in Reference [13], on the electric viscosity should be used.

3.1. Semipermeable membrane

This problem deals with 2D transient fluid flow through a region bounded by two membranes, permeable to the water flow but impermeable for solutes, i.e. two semipermeable membranes. The employed geometry and boundary conditions are shown in Figure 1. For the numerical simulations a rather fine finite element mesh consisting of 6176 triangular elements has been used.

Initially the (uncharged) solute is uniformly distributed over the region ($c = 10$ mol/m³) and the fluid pressure equals zero. At t_0 a pressure gradient ($p_1 = 1 \times 10^5$ N/m² and $p_2 = 0$ N/m²) is applied leading to fluid flow. The solute concentration along a cross section ($y = 5$ nm) is shown in Figure 2(a). It clearly indicates accumulation of the solute ions on the right membrane with increasing time. This redistribution of solute ions leads to the development of

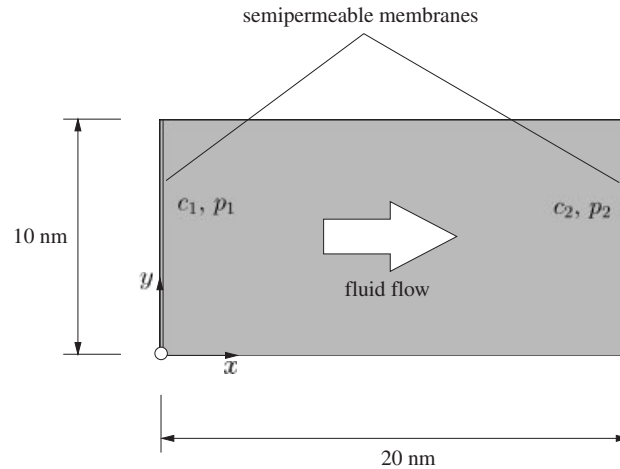


Figure 1. Navier–Stokes flow through a semipermeable membrane: geometric dimensions and boundary conditions.

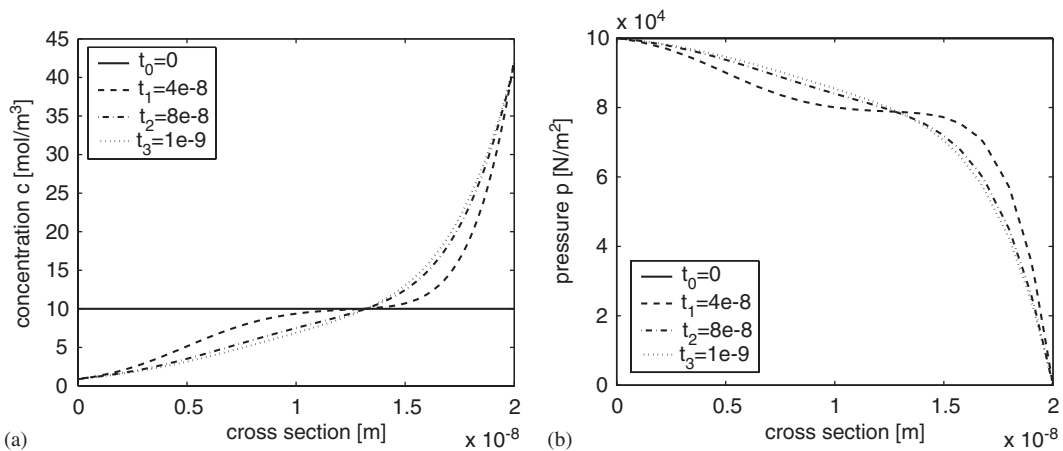


Figure 2. Navier–Stokes flow through a semipermeable membrane: (a) species concentration c (mol/m^3); and (b) pressure p (N/m^2) along a cross section ($y = 5 \text{ nm}$) at various time instants.

a concentration gradient acting in the opposite direction to the fluid flow. This in turn leads a redistribution of the fluid pressure (see Figure 2(b)).

This solution demonstrates that the permeability of a porous medium (such as for example soil) close to an evaporative surface decreases, due to the gradient of solute in the pore fluid at the surface. This problem also illustrates the generality of the proposed description of microscale ion transport processes using the generalized electrical force term (Equation (12)).

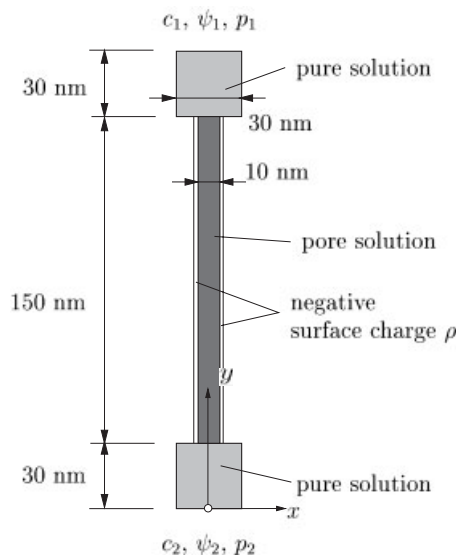


Figure 3. Charged slit opening: geometric dimensions and boundary conditions.

3.2. Mass transport through a charged slit opening

This problem deals with 2D stationary fluid flow ($\partial \mathbf{v}^f / \partial t = 0$) of an electrolyte through a negatively charged slit opening. The geometric dimensions of the slit and the boundary conditions are shown in Figure 3. The finite element mesh used for the numerical analyses consists of 2336 elements. In order to investigate the transition regions between a salt solution and the pore fluid saturating the slit opening (pore solution) ‘source’ and ‘collector’ regions were included (see light grey areas in Figure 3). For the Navier–Stokes problem no slip boundary conditions were used at the side walls. The boundary conditions employed for various subproblems are given in Table II.

The first transport phenomenon dealt with is pure diffusive mass transport (see subproblem 1.1 in Table II, rows 1–3). We begin by investigating the *equilibrium state* between the *membrane* (charged slit opening) and the solution (no fluid flow). A characteristic feature of ion-exchanger membranes is the large difference in permeability for counter ions and co-ions (known as *permselectivity* [15]). For the negatively charged slit opening Figure 4(a) clearly shows how co-ions (i.e. the negatively charged ions) are excluded from the *membrane*.

This exclusion depends on the electrolyte concentration and the surface charge density (ρ) on the slit walls [15]. Increasing the electrolyte concentration while keeping ρ constant leads to less pronounced co-ion exclusion because of the compression of the diffuse double-layer (see Figure 4(a)). In order to maintain overall electroneutrality of the system an electric potential (exclusion potential) between the membrane and the solution must develop.^{‡‡} The exclusion

^{‡‡}The exclusion potential repels co-ions from the membrane and thus prevents the internal co-ion concentration from rising beyond an equilibrium value which is usually much smaller than the concentration in the external solution (see [15] for details).

Table II. Boundary conditions used for subproblems (¹... ψ_2 computed from the nil current condition, i.e. $\sum z_i j_i = 0$; ²... application of zero voltage gradient, i.e. electric short-circuit boundary condition).

Problem No.	c_1 (mol/m ³)	c_2 (mol/m ³)	ψ_1 (V)	ψ_2 (V)	p_1 (N/m ²)	p_2 (N/m ²)
1.1	1	1	0	0	0	0
	10	10	0	0	0	0
	50	50	0	0	0	0
	20	10	0	1	0	0
1.2	10	10	0	2	10 ³	0
	10	10	0	2	10 ⁴	0
	10	10	0	2	10 ⁵	0
1.3	1	1	0	0	10	0
	10	10	0	0	10	0
	100	100	0	0	10	0
	1000	1000	0	0	10	0

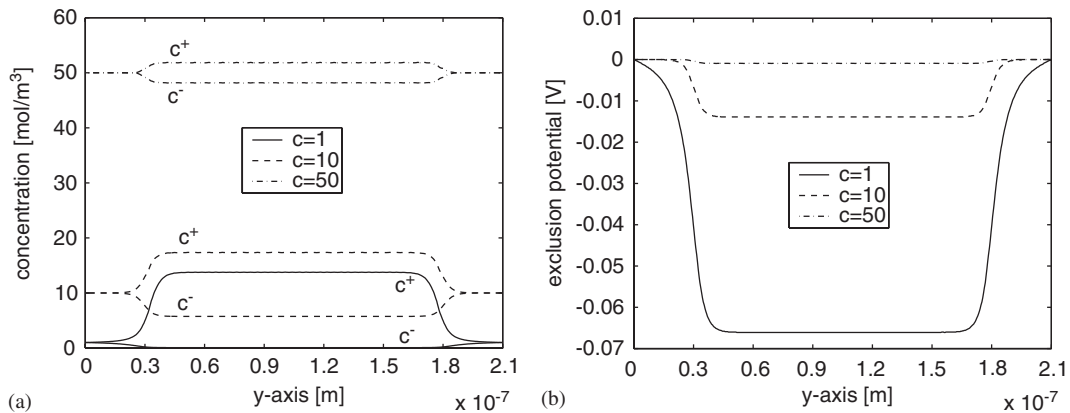


Figure 4. Charged slit opening: equilibrium state: (a) co-ion and counter-ion distribution; and (b) exclusion potential along the y -axis for $\rho = -0.01 \text{ C/m}^2$.

potential (often called the Donnan potential) is shown for various electrolyte concentrations in Figure 4(b). An analytical expression for the exclusion potential is given as [15]:

$$\Delta\psi_{\text{ex}} = \bar{\psi} - \psi = \frac{RT}{z_i F} \ln \frac{c_k}{\bar{c}_k} \tag{22}$$

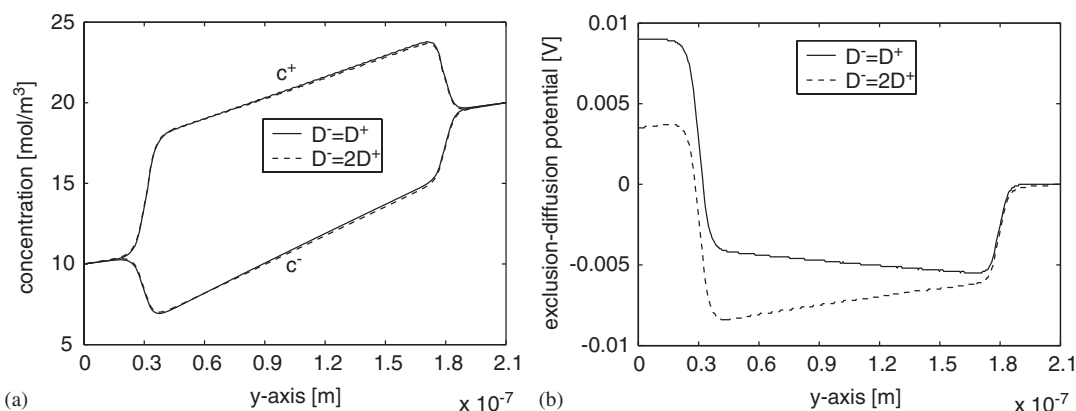


Figure 5. Charged slit opening: diffusive mass transport: (a) co-ion and counter-ion distribution; and (b) diffusion–exclusion potential along the y -axis for $\rho = -0.01 \text{ C/m}^2$.

where ψ , $\bar{\psi}$ and c_k , \bar{c}_k are the electric potentials and the species concentrations outside and inside the membrane.^{§§} For the case of a 10 mol/m^3 electrolyte solution, the exclusion potential is estimated to be -13.9 mV from the numerical model (see Figure 4(b)). The counter-ion and co-ion concentration inside the slit opening are 17.37 and 5.74 mol/m^3 (see Figure 4(a)). Inserting these values into Equation (22) leads to the same exclusion potential, validating the numerical model.

Now having some idea how equilibrium is established for the membrane–solution system, we investigate diffusive mass transport across the membrane (see subproblem 1.1 in Table II, row 4). The concentration distribution of co-ions and counter-ions together with the diffusion–exclusion potential are given along the y -axis for two different ratios of anion/cation self-diffusion coefficients in Figure 5.

Increasing the self-diffusion coefficient of anions leads to an increase of the salt flux from $7.3 \times 10^{-10} \text{ mol}$ (for $D_- = D_+$) to $1.2 \times 10^{-9} \text{ mol}$ (for $D_- = 2D_+$). The rate of electrolyte diffusion is controlled by diffusion of the species in *minority*, i.e. the co-ion (see Reference [15] for details). An interesting consequence is that in the case of a cation exchanging membrane (negatively charged pore surfaces) two salts such as HCl and NaCl ($D_{\text{H}} = 9.31 \times 10^{-9} \text{ m}^2/\text{s}$, $D_{\text{Na}} = 1.33 \times 10^{-9} \text{ m}^2/\text{s}$, $D_{\text{Cl}} = 2.03 \times 10^{-9} \text{ m}^2/\text{s}$ [16]) diffuse at about equal rates. However, this increase of self-diffusion coefficient of anions has almost no influence on the counter-ion and co-ion distribution in the membrane–solution system (see Figure 5(a)). This indicates that the counter-ion and co-ion distribution is mainly governed by the concentration gradient applied to the system.

Without application of an external electrical field the system is characterized by zero current density (nil current condition). Fulfilment of this condition implies equality of the counter-ion and co-ion fluxes which in turn leads to the development of an electric potential (exclusion–diffusion potential). For the general case of a charged porous medium the exclusion–diffusion

^{§§}Activity effects are not considered in Equation (22).

potential is also denoted as membrane or concentration potential [15]. On the other hand, in the absence of the porous medium this potential is called the liquid junction potential [17]. According to Reference [15] the exclusion–diffusion potential is the sum of the exclusion potentials and the diffusion potential

$$\begin{aligned}\Delta\psi_{\text{ed}} &= \psi_2 - \psi_1 \\ &= \Delta\psi_{\text{ex},1} - \Delta\psi_{\text{ex},2} + \Delta\psi_{\text{diff}} \\ &= -\frac{RT}{z_+F} \left(\ln \left(\frac{(c_+)_2}{(c_+)_1} \right) - (z_- - z_+) \int_1^2 \bar{t}_- d \ln c_{\pm} \right)\end{aligned}\quad (23)$$

where $\Delta\psi_{\text{ex},1}$ and $\Delta\psi_{\text{ex},2}$ are the exclusion potentials of the source and collector cells, respectively (see Figure 3). The subscripts 1 and 2 refer to the different phases (i.e. high and low concentration phase). $\bar{t}_i = z_i \bar{c}_i \bar{D}_i / ((z_+)^2 \bar{c}_+ \bar{D}_+ + (z_-)^2 \bar{c}_- \bar{D}_-)$ is the transference number. Given the concentration profiles of counter-ions and co-ions the integral in Equation (23) can be evaluated numerically. Equation (23) can be simplified by using the Meyer–Sievers assumptions (see Reference [18] for details), i.e. assuming that the ionic concentrations $(\bar{c}_i)_k$ in a charged pore are related to the bulk concentration $((c_+)_k = (c_-)_k = (c)_k$ for 1:1 electrolyte) by

$$\begin{aligned}(\bar{c}_-)_k &= y_k \\ (\bar{c}_+)_k &= y_k - q/F \\ y_k(y_k - q/F) &= (c)_k^2 \\ q &= 2\rho/b\end{aligned}\quad (24)$$

where q is the charge per unit volume in a pore (C/m^3) and b is the slit width. Using this assumption leads the estimated exclusion–diffusion potential as [18]

$$\begin{aligned}\Delta\psi_{\text{ed}} &= \Delta\psi_{\text{ex}} + \Delta\psi_{\text{diff}} \\ &= \frac{1}{2} \ln \left(\frac{(Y_2 + 1)(Y_1 - 1)}{(Y_2 - 1)(Y_1 + 1)} \right) + U \ln \left(\frac{Y_2 - U}{Y_1 - U} \right)\end{aligned}\quad (25)$$

where $Y_k = (2y_k/(q/F)) - 1$ and $U = (D_+ - D_-)/(D_+ + D_-)$. According to Equation (25)₂ the diffusion potential equals zero for $D_- = D_+$ and 4.7 mV for $D_- = 2D_+$. Using Equation (25)₁ leads the exclusion potential as -10.3 mV. Note that the exclusion potential given in Equation (25) is a function of the solution concentration and the charge per unit volume only. Summing up these two contributions leads the exclusion–diffusion potentials as -10.3 mV (for $D_- = D_+$) and -5.7 mV (for $D_- = 2D_+$). Comparison of these approximate values (based on the Meyer–Sievers assumptions) with the diffusion–exclusion potentials obtained from the numerical simulations (see Figure 5(b)), i.e. $\psi_{\text{ed}} = -9.0$ mV (for $D_- = D_+$) and $\psi_{\text{ed}} = -3.2$ mV (for $D_- = 2D_+$) indicates good agreement.

Whereas in the preceding problems, systems were investigated in which the solutions are under equal pressure ($p_1 = p_2$, i.e. no fluid flow), the third investigation deals with the effect

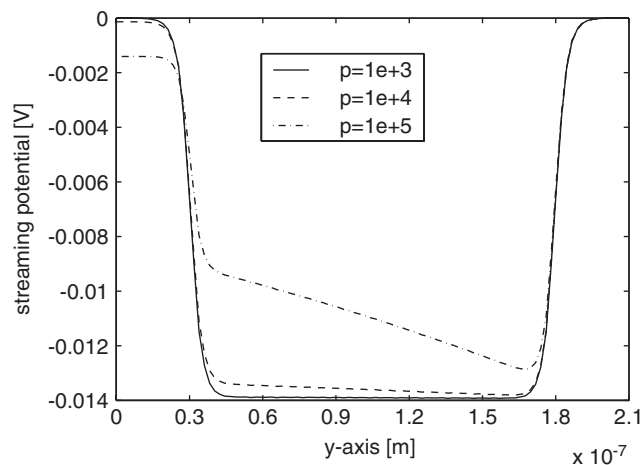


Figure 6. Charged slit opening: Navier–Stokes flow—dependence of the streaming potential on the relative pressure $\Delta p = p_1 - p_2$ (in N/m^2) for $\rho = -0.01 \text{ C/m}^2$.

of a pressure gradient (subproblem 1.2 in Table II). This pressure gradient ($p_1 > 0$, $p_2 = 0$) applied to the solution forces water flow through the membrane (see Figure 3). The pore liquid carries the net electric charge and, so, ion displacement builds up an electric potential difference, the so-called streaming potential (see Reference [15] for details). Figure 6 shows the streaming potential for various pressure gradients. Increasing the pressure gradient Δp leads to an increase of the streaming potential. At a pressure difference of $1 \times 10^5 \text{ N/m}^2$ ($\approx 1 \text{ atm}$) the streaming potential is -1.8 mV .

For solutions of identical composition in the source and collector regions (i.e. no difference in exclusion potentials between the two membrane interfaces), the streaming potential is given as [15]

$$\Delta\psi_{\text{str}} = \frac{\omega XF}{\sigma_0 \bar{\kappa}} \Delta p \quad (26)$$

where ω denotes the sign of the fixed charge concentration X . σ_0 is the specific flow resistance and $\bar{\kappa}$ denotes the specific electric conductivity of the membrane. For a typical cation-exchanger membrane ($\omega = -1$, $X = 2000 \text{ mol/m}^3$, $\sigma_0 = 10^{16} \text{ kg/m}^3/\text{s}$, $\bar{\kappa} = 1 \Omega^{-1} \text{ m}^{-1}$ (data from Reference [15])) the streaming potential is of the order of a few millivolts per atmosphere pressure difference between the solutions. It is interesting to note that this macroscopic estimate is in the range of the value for the streaming potential we have found here at the nanoscale, i.e. $\Delta\psi_{\text{str}} = 1.8 \text{ mV}$ for $\Delta p = 1 \times 10^5 \text{ N/m}^2$.

The next investigation is similar to the previous one (see subproblem 1.3 in Table II). An extensive study considering the influence of various model parameters on the numerical results was reported in References [6, 19]. In the following, we consider two cases: (i) uncharged solutes pinned in the slit solution (i.e. setting $F = 0$) and (ii) a 1:1 background electrolyte in the slit solution. The influence of background electrolyte concentration and surface charge density (ρ) on the numerical results is investigated for case (ii). The physical relevance of this problem is that it is observed experimentally in montmorillonitic clay soils that the permeability

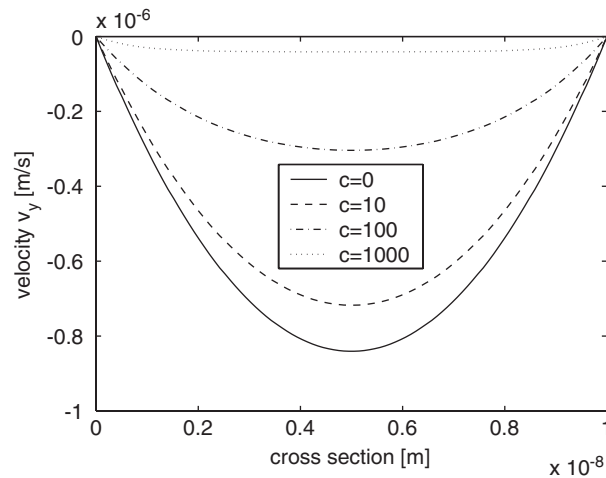


Figure 7. Charged slit opening: Navier–Stokes flow—velocity profiles for various uncharged species concentrations c in mol/m^3 .

increases significantly as the background electrolyte concentration increases, even though the porosity of the clay is unchanged [1].

For case (i) the velocity profiles obtained for uniformly distributed uncharged solutes indicates a strong decrease of the maximum fluid velocity with increasing concentration (see Figure 7). Comparison of the various profiles indicates a transition from a parabolic curve (classically obtained from the Navier–Stokes problem using $c = 0 \text{ mol/m}^3$) to a very flattened curve for high electrolyte concentration ($c = 1000 \text{ mol/m}^3$). This illustrates that the energy dissipation by friction with ions in solution may be much more significant than energy dissipation in the fluid (water) itself.

The dependence of the fluid flux on the concentration for uncharged (uniform distribution) and charged (non-uniform distribution) solutes (cases (i) and (ii)) is shown in Figure 8. Increasing the concentration of uncharged solutes pinned in the pore solution strongly decreases the fluid flux (Figure 8(a)). On the other hand, increasing the concentration of background electrolyte leads to an increase of the fluid flux (Figure 8(b)) independent of surface charge density ρ . This increase of flux with electrolyte concentration c is a consequence of the compression of the diffuse double-layer. In the limit of zero surface charge density equal numerical results are obtained for both cases (compare Figure 8(a) and (b)). This model behaviour may be interpreted in the following way: as the double-layer contracts, pore spaces are ‘unblocked’, and the permeability of the charged porous medium increases.

Finally, we investigate the influence of the hydration parameter k_0 (Equation (4)) on the numerical results. For this purpose k_0 was assumed to take values of 250, 1000, 2500, and 10000. For this example a electrolyte concentration of $c = 100 \text{ mol/m}^3$ and a surface charge density of $\rho = -0.2 \text{ C/m}^2$ has been assumed. Dependence of the solvent flux on the concentration of background electrolyte and the hydration parameter is shown in Figure 9(a). Increase of k_0 leads to a strong increase of the solvent flux.

The distribution of cations in a cross-section of the slit ($y = 75 \text{ nm}$) is given in Figure 9(b). Increasing the hydration parameter k_0 (i.e. decreasing the hydrated ion size) leads

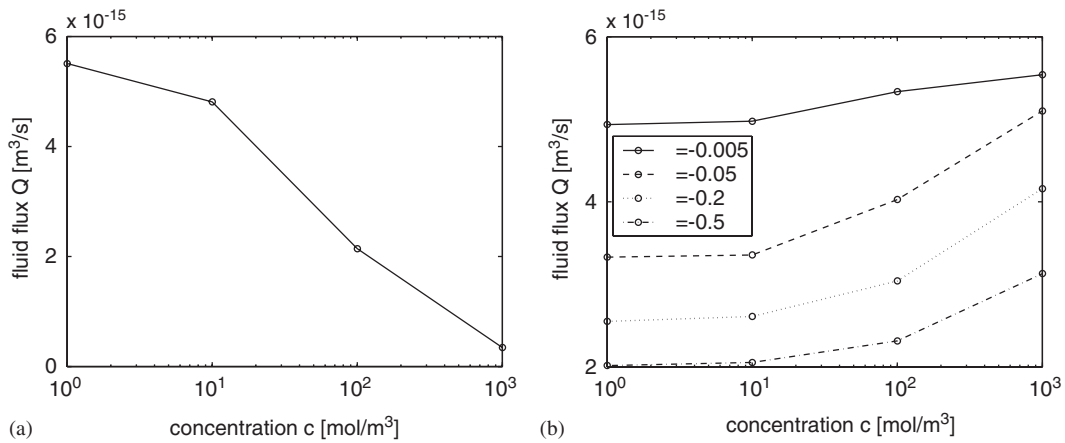


Figure 8. Charged slit opening: Navier–Stokes flow—dependence of solvent flux on species concentration for: (a) uncharged species; and (b) an electrolyte for various surface charges (ρ in C/m²).

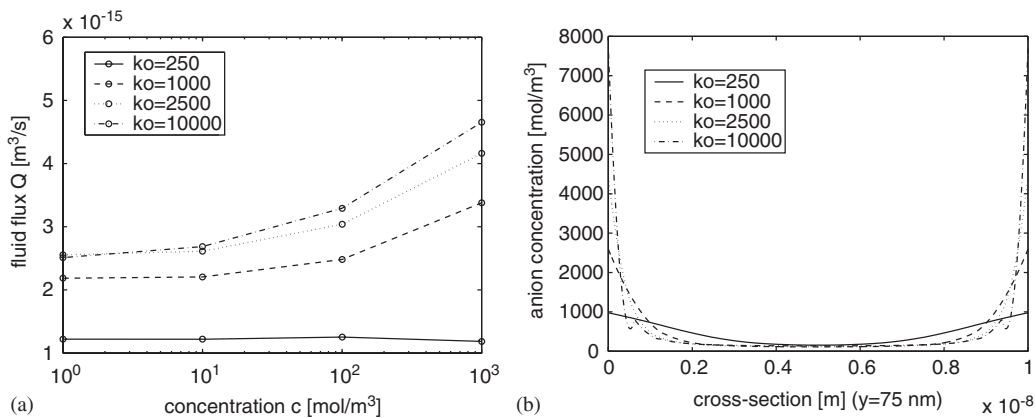


Figure 9. Charged slit opening: Navier–Stokes flow—influence of hydration parameter on: (a) ion flux; and (b) ion concentration (in cross section).

to a strong increase of surface concentration from approximately 1000 mol/m³ (for $k_0 = 250$) to 7000 mol/m³ (for $k_0 = 10000$).

4. CONCLUSIONS

From the numerical results obtained from the coupled Nernst–Planck–Navier–Stokes–Poisson equations the following conclusions can be drawn: it was found that the proposed model is capable of predicting many transport phenomena encountered at the macroscale, such as co-ion exclusion, the development of exclusion–diffusion potentials, and the development of streaming potentials in charged porous membranes. Furthermore, it was shown that energy dissipation by friction with ions in solution may be a significant contributor to the overall energy dissipation

(i.e. energy dissipation by friction within the fluid and by friction between the fluid and ions pinned in the pore solution). This dissipation mechanism was found to be responsible for the dependence of fluid flux on background electrolyte concentration and surface charge density. It is noted that accounting for finite ion size increases energy dissipation.

Finally it is noted that the proposed coupled model provides a powerful tool for the investigation of electrohydrodynamic transport problems. In order to further evaluate the model, comparison between (macroscopic) experimental data and numerical results will be made after upscaling.

ACKNOWLEDGEMENTS

The first author gratefully acknowledges the financial support of this study by the Austrian Foundation for the Promotion of Scientific Research (FWF) in the course of an Erwin Schrödinger scholarship.

REFERENCES

- Hueckel T. Coupled constitutive models in environmental geomechanics. In *Workshop on GeoEnvironmental Engineering*, Ascona, Switzerland, 30 June–5 July 2002, Vulliet Z, Laloui F, Schrefler P (eds). Environmental Geomechanics Publications EPFL Press, 27–44.
- Shackelford CD, Benson CH, Katsumi T, Edil TB, Lin L. Evaluating the hydraulic conductivity of GCLs permeated with non-standard liquids. *Geotextiles and Geomembranes* 2000; **18**:133–161.
- Hunter RJ. *Foundations of Colloid Science*. Oxford University Press: Oxford, U.K., 2001.
- Sposito S. *The Chemistry of Soils*. Oxford University Press: New York, U.S.A., 1989.
- Iwata S, Tabuchi T, Warkentin BP. *Soil–water Interactions*. Marcel Dekker: New York, U.S.A., 1995.
- Smith D, Pivonka P. Theoretical analysis of the influence of a diffuse double-layer on Darcy's law. In *IUTAM Symposium on the Mechanics of Physicochemical and Electromechanical Interactions in Porous Media*, 18–23 May 2003, Huyghe J (ed.). Rolduc, Kerkrade: The Netherlands, 2003; 1–13.
- Cussler EL. *Diffusion Mass Transfer in Fluid Systems* (2nd edn). Cambridge University Press: New York, U.S.A., 1997.
- Smith D, Pivonka P, Jungnickel C, Fityus S. Theoretical analysis of anion exclusion and diffusive transport through platy-clay soils. *Transport in Porous Media* 2004; **57**:251–277.
- Shainberg I, Kemper WD. Hydration status of adsorbed ions. *Soil Science Society of America Proceedings* 1966; **30**:707–713.
- Slattery JC. *Advanced Transport Phenomena*. Cambridge University Press: Cambridge, U.S.A., 1999.
- Eringen AC, Maugin GA. *Electrohydrodynamics of Continua II: Fluids and Complex Media*. Springer: New York, U.S.A., 1990.
- Derjaguin BV. *Theory of Stability of Colloids and Thin Films*. Consultants Bureau: New York, U.S.A., 1989.
- Hunter RJ, Leyendekkers JV. Viscoelectric coefficient for water. *Journal of the Chemical Society. Faraday Transactions I* 1978; **A204**:450–455.
- Ichikawa Y, Kawamura K, Fujii N, Nattavut T. Molecular dynamics and multiscale homogenization analysis of seepage/diffusion problem in bentonite clay. *International Journal for Numerical Methods in Engineering* 2002; **54**:1717–1749.
- Helfferich F. *Ion Exchange, Series in Advanced Chemistry*. McGraw-Hill: New York, U.S.A., 1962.
- Robinson RA, Stokes RH. *Electrolyte Solutions* (2nd edn). Butterworths Scientific Publications: London, England, 1959.
- Sen PN. Unified model of conductivity and membrane potential of porous media. *Physical Review B* 1989; **39**(13):9508–9517.
- Westermann-Clark GB, Christoforou CC. The exclusion–diffusion potential in charged porous membranes. *Journal of Electroanalytical Chemistry* 1986; **198**(1986):213–231.
- Pivonka P, Smith D. Electro-hydrodynamic transport in porous materials. *Advances in Geotechnical Engineering, The Skempton Conference*, 29–31 March 2004, London, England, vol. 1. Thomas Telford, 2004, 592–603.

P. Pivonka, D. Smith, and B. Gardiner. Investigation of Donnan equilibrium in charged porous materials: a scale transition analysis. *Transport in Porous Media*, 2007. (in print)

Investigation of Donnan equilibrium in charged porous materials — a scale transition analysis

Peter Pivonka · David Smith · Bruce Gardiner

Received: 28 June 2004 / Accepted: 4 October 2006
© Springer Science+Business Media B.V. 2006

Abstract We propose a new theory describing how the macroscopic Donnan equilibrium potential can be derived from the microscale by a scale transition analysis. Knowledge of the location and magnitude of the charge density, together with the morphology of the pore space allows one to calculate the Donnan potential, characterizing ion exclusion in charged porous materials. Use of the electrochemical potential together with Gauss' electrostatic theorem allows the computation of the ion and voltage distribution at the microscale. On the other hand, commonly used macroscopic counterparts of these equations allow the estimation of the Donnan potential and ion concentration on the macroscale. However, the classical macroscopic equations describing phase equilibrium do not account for the non-homogeneous distribution of ions and voltage at the microscale, leading to inconsistencies in determining the Donnan potential (at the macroscale). A new generalized macroscopic equilibrium equation is derived by means of volume averaging of the microscale electrochemical potential. These equations show that the macroscopic voltage is linked to so-called "effective ion concentrations", which for ideal solutions are related to logarithmic volume averages of the ion concentration at the microscale. The effective ion concentrations must be linked to an effective fixed charge concentration by means of a generalized Poisson equation in order to deliver the correct Donnan potential. The theory is verified analytically and numerically for the case of two monovalent electrolytic solutions separated by a charged porous material. For the numerical analysis a hierarchical modeling approach is employed using a one-dimensional (1D) macroscale model and a two-dimensional (2D) microscale model. The influence

P. Pivonka (✉) · D. Smith · B. Gardiner
Department of Civil and Environmental Engineering, The University of Melbourne,
Melbourne, VIC 3010, Australia
e-mail: ppivonka@unimelb.edu.au

D. Smith
e-mail: david.smith@unimelb.edu.au

B. Gardiner
e-mail: bgardine@unimelb.edu.au

of various parameters such as surface charge density and ion concentration on the Donnan potential are investigated.

Keywords Donnan potential · Anion exclusion · Electrochemical potential · Poisson equation · Charged porous materials · Volume averaging

Notations

The following notations are used in this article.

c_i	Concentration of ions in pore solution, mol/m ³
c_{i1}	Concentration of ions in pure solution (phase 1), mol/m ³
c_{i2}	Concentration of ions in porous material (phase 2), mol/m ³
d	Characteristic length of heterogeneities, m
ℓ	Characteristic length of RVE, m
\mathbf{D}_f	Electric displacement of fluid, C/m ²
E_{Don}	Donnan potential, V
$E_{\text{Don},+}, E_{\text{Don},-}$	Donnan potential computed from cations and anions, V
F	Faraday constant, C/mol
L	Characteristic length of structure, m
\mathbf{n}_f	Unit normal vector
R	Universal gas constant, J/(K mol)
S_{sf}	Area of solid-fluid interface within RVE, m ²
T	Absolute temperature, K
\mathbf{x}	Macroscopic spatial coordinates, m
\mathbf{z}	Microscopic spatial coordinates, m
z_i	Valence of ion i
α	Index for α -phase (i.e., solid or liquid)
β	Index for β -material (i.e., solution or charged porous material)
ε	Permittivity of the medium, C ² /(J m)
$\varepsilon_{\text{eff}\beta}$	Effective permittivity of β -material, C ² /(J m)
ε_f	Relative permittivity of fluid
ε_w	Relative permittivity of water
ε_0	Permittivity of free space, C ² /(J m)
$\mu_{i\beta}$	Electrochemical potential, J/mol
ρ_β	Volume charge density in fluid phase of β -material, C/m ³
σ_β	Surface charge density on solid–fluid interface of β -material, C/m ²
ϕ_α	Volume fraction of α -phase
χ^0, χ^α	Indicator functions
ψ_β	Microscopic voltage, V
ω	Sign of intrinsic fixed charge concentration
$\Omega(\mathbf{0}), \Omega(\mathbf{x})$	Domain of the RVE at $\mathbf{x} = \mathbf{0}$ and \mathbf{x}
Ω_α	Domain occupied by the α -phase of the RVE
$\partial\Omega_{sf}$	Solid-fluid interface within the RVE

$\mathcal{V}, \mathcal{V}_\alpha$	Total volume and volume of α -phase of RVE, m^3
$\overline{e}_\alpha^\alpha(\mathbf{x}, t)$	Intrinsic phase average of e
$\overline{e}_\alpha(\mathbf{x}, t)$	Apparent phase average of e
$\overline{c_{i\beta}^f}$	Intrinsic actual concentration, mol/m^3
$\widehat{\overline{c_{i\beta}^f}}$	Intrinsic effective concentration, mol/m^3
$\overline{X_\beta^f}$	Intrinsic fixed charge concentration, mol/m^3
$\widehat{\overline{X_\beta^f}}$	Intrinsic effective fixed charge concentration, mol/m^3
$\overline{\psi_\beta^f}$	Intrinsic voltage, V
$\Delta\overline{\psi^f}$	Difference in intrinsic voltage, V

1 Introduction

A broad class of porous materials including clays, shales, polyelectrolyte gels, and biological tissues are characterized by positive and/or negative charge on their surfaces (Hunter 2001). For example in the case of clay minerals negative charges are often a consequence of isomorphous substitutions of certain atoms in the clay crystal lattice, crystal imperfections (defects or broken bonds), or ligand exchange reactions on the particle surface (Sposito 1989; Iwata et al. 1995). The presence of surface charges leads to formation of diffuse-double layers characterized by high surface concentrations of anions or cations depending on the sign of the surface charge.

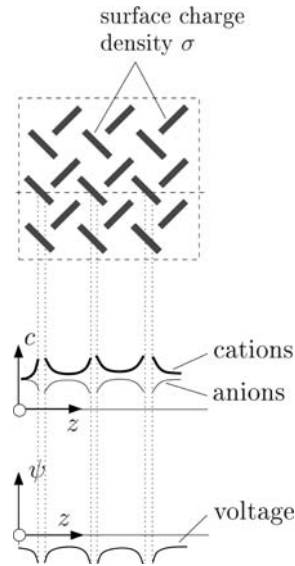
When a charged porous material is immersed in an electrolytic solution there are considerable concentration differences between the solution and the porous material arising from the fixed charges in the porous material. In the case of a negatively charged porous material the cation concentration is higher in the porous media phase (relative to the solution phase outside the porous material), whereas the opposite holds for anions. This phenomenon is often referred to as anion exclusion.¹ There are three main chemo-physical mechanisms that give rise to a voltage difference $\Delta\overline{\psi^f}$ across an external electrolytic solution and charged porous materials (Westermann-Clark and Christoforou 1986): (i) steric exclusion (characteristic of polymer molecules too large to enter the pores of the porous membrane), (ii) electrostatic repulsion (surface charges on the pore walls of the membrane repel ions whose charge has the same sign), and (iii) combinations of steric and electrostatic effects. This voltage difference is commonly referred to as the Donnan Potential (E_{Don}). In the following, we consider only electrostatic exclusion.

The solution of the classical Poisson–Boltzmann equation describing ion and voltage distribution near charged particles (at the microscale²) shows a highly nonlinear distribution of these quantities (see Fig. 1) over a distance ranging from one to hundreds of nanometers (the so-called Debye length) depending on concentration of background electrolyte, temperature, and solvent type (Hunter 2001). However, most engineering applications only deal with the investigation of macroscopic quantities such as macroscopic concentrations and electric potentials (e.g., the Donnan potential between an electrolytic solution and a porous material containing surface charges on

¹ Ions that electrically balance the fixed charges in porous materials are commonly referred to as counter-ions. Whereas, ions of opposite charge to the fixed charges are denoted as co-ions.

² In the following we denote the scale where non-linearities in ion and voltage distribution are detected as the microscale.

Fig. 1 Schematic representation of nonlinearities in concentration and voltage distribution observed at the microscale for a negatively charged porous material (e.g., platy clay) immersed in a binary electrolytic solution



particles). Estimation of (macroscopic) electrostatic potentials is generally performed indirectly by measuring first the (macroscopic) fixed charge density (or fixed charge concentration) based on ion exchange reactions or titration experiments. Then at a second step ion concentrations and electrostatic potential in the charged porous material are calculated based on the macroscopic Donnan equilibrium model (see Sect. 3.2). However, it has been found that the Donnan equilibrium model may significantly overestimate the electrostatic potential in charged biological tissues and polyelectrolyte gels (see [Basser and Grodzinsky 1993](#) and Sect. 5 for details). This is because the classical macroscopic Donnan model is based on the assumption of a *homogeneous* charge distribution across the material ([Basser and Grodzinsky 1993](#); [Dähnert and Huster 1999](#)).

In this article, we address the following question: how are *microscopic* electrochemical quantities such as cation and anion concentration, voltage distribution, and fixed surface charge density, related to the respective *macroscopic* (that is, measurable) quantities? A similar question has been previously addressed in a simplified one dimensional(1D) form by ([Basser and Grodzinsky 1993](#)) and later by ([Dähnert and Huster 1999](#)). However, the focus of these authors was to derive relations between the Poisson–Boltzmann model and the Donnan equilibrium model. In contrast, our approach is hierarchical, we use two models, one at the microscale and one at the macroscale, in order to give estimates for the macroscopic electric potential. Input parameters for the macroscale models are estimated from a microscale analysis. Furthermore, equations given in this article are not restricted to 1D problems that have analytical solutions such as the previous cited works. In other words, the method described here is completely general.

For the two scale hierarchical modeling approach we assume that the location and magnitude of fixed surface charge density and the pore morphology (i.e., the size and location of particles) is known at the microscale. The fixed surface charge density may be readily estimated using ion exchange methods ([Sposito 1989](#)). Information on pore

morphology can be obtained for example using transmission electron microscopy with serial sectioning and 3D reconstruction or with micro-CT for large particles. Based on this microscale information we employ the definition of electrochemical potential together with the Poisson equation in order to determine the ion and voltage distribution together with effective permittivities and fixed charge concentrations. The latter two quantities serve as input parameters for the macroscale model, where the macroscopic (i.e., measurable) quantities are estimated.

The article is organized as follows: Sect. 2 deals with the theoretical framework of macroscopic modeling approaches including the fundamental notion of *representative volume element* (RVE) and modeling of phase boundaries. In Sect. 3, we summarize the governing equations describing phase equilibrium at the microscale and macroscale (i.e., the classical Donnan equilibrium model). Limitations and assumptions of these equations are also discussed in this section. Generalized equations describing phase equilibrium at the macroscale are then derived in Sect. 4 based on volume averaging of the microscale governing equations. The two theories are compared using an analytical and a numerical example of phase equilibrium between monovalent electrolytic solutions separated by a charged porous material. The numerical analysis is described in detail in Sect. 5, where we also perform a parametric study of the influence of surface charge density and concentration of background electrolyte on the numerical results.

2 Hierarchical modeling approach

Application of governing equations at various length scales is generally denoted as a “hierarchical modeling approach.” The hierarchy of models used in this approach are denoted as macro, meso, micro, etc. models depending on the length scale. This approach allows one to obtain detailed insight into a (physical) problem on different scales of observation. The information gained at lower levels can be linked to higher levels by a mathematical process known as *up-scaling* or *homogenization*. Up-scaling is a (volume) averaging method (see, e.g., [Bear and Bachmat 1991](#); [Zaoui 1997](#); [Whitaker 1999](#)), where microscopic quantities are averaged over a RVE in order to obtain macroscopic quantities.³ In the course of the averaging process information about the microscale is necessarily lost. Considering the large dimensions of macroscopic structures, compared to the size of a typical RVE, it is practically impossible to simulate all processes occurring at lower scales as computer resources are finite. Therefore, a macroscopic model is employed at the global level, whereas mesoscale models are applied only at selected “points” in the macroscopic domain, likewise microscopic models are in turn applied at selected “points” in the mesoscopic domain, and so on. In this way, selected information about one level is introduced into the level above, and so, a compromise is made between capturing important microscale processes on the one hand, and limited computer resources on the other hand. By using this approach, previously intractable numerical problems become solvable.

³ Macroscopic governing equations derived empirically are often referred to as phenomenological equations.

2.1 Representative volume element

Every macroscopic (3D) mechanical structure can be characterized by its macroscopic (structural) length (L) and the length of microstructural heterogeneities (d). In the case of a porous material, the characteristic length scale of the local heterogeneities is typically defined by the pore size. Often L and d are separated by several orders of magnitude. This allows one to introduce the concept of RVE on which continuum mechanics is based (see, e.g., [Bear and Bachmat 1991](#)). Mathematically the choice of RVE having characteristic length ℓ is formulated as separation of scales condition, i.e., $d \ll \ell \ll L$. Condition $\ell \ll L$ guarantees that the tools of differential calculus offered by a continuous description can be used. In turn, $\ell \gg d$ aims at ensuring that the elementary volume is large enough to be representative of the constitutive properties of the material.

Macroscopic poromechanics accounts for the multiphase nature of the porous material by considering different phases present in the RVE (solid and liquid) as distinct macroscopic phases located at the same macroscopic point \mathbf{x} . At this scale, the RVE is regarded as the superposition of these phases (particles) in space. By contrast, the micromechanical viewpoint considers the RVE as a heterogeneous structure in which the different physical phases are located in separate domains. This requires a refinement of the length scale. At the microscale the position vector is here denoted by \mathbf{z} . Depending on \mathbf{z} , the microscopic particle located at point \mathbf{z} belongs to either the solid phase or to a fluid phase. By definition, the characteristic order of magnitude of the variation of \mathbf{z} is the size ℓ of the RVE.

For a physical quantity $e(\mathbf{z})$ assigned to the α -phase (i.e., solid or liquid) there are two different spatial averages, namely the *apparent phase average* and the *intrinsic phase average*, as defined by ([Dormieux 2005](#))

$$\overline{e_\alpha}(\mathbf{x}, t) = \frac{1}{\mathcal{V}} \int_{\Omega(\mathbf{x})} \chi^0(\mathbf{z} - \mathbf{x}) \chi^\alpha(\mathbf{z}, t) e(\mathbf{z}, t) dV_z \tag{1}$$

$$\overline{e_\alpha^\alpha}(\mathbf{x}, t) = \frac{1}{\mathcal{V}_\alpha} \int_{\Omega_\alpha(\mathbf{x})} \chi^0(\mathbf{z} - \mathbf{x}) \chi^\alpha(\mathbf{z}, t) e(\mathbf{z}, t) dV_z \tag{2}$$

where \mathcal{V} and \mathcal{V}_α denote the total volume and the volume of the α -phase of the RVE respectively. χ^0 and χ^α are the characteristic (or indicator) functions of $\Omega(\mathbf{0})$ and Ω_α (see notation section for definitions and ([Dormieux 2005](#)) for details). It follows that apparent and intrinsic phase averages are related by:

$$\overline{e_\alpha}(\mathbf{x}, t) = \phi_\alpha \overline{e_\alpha^\alpha}, \tag{3}$$

where $\phi_\alpha = \mathcal{V}_\alpha/\mathcal{V}$ is the phase volume fraction.

2.2 Modeling phase boundaries

Macroscopic equations are strictly valid only within a certain material domain. On the interface between two materials (such as an electrolytic solution and a charged porous material) the method of volume averaging has to be applied with caution. [Figure 2](#) shows three regions of different materials: a binary electrolytic solution containing no solid matrix (material 1) and two materials having different porosities and negative surface charge density (material 2 and material 3).

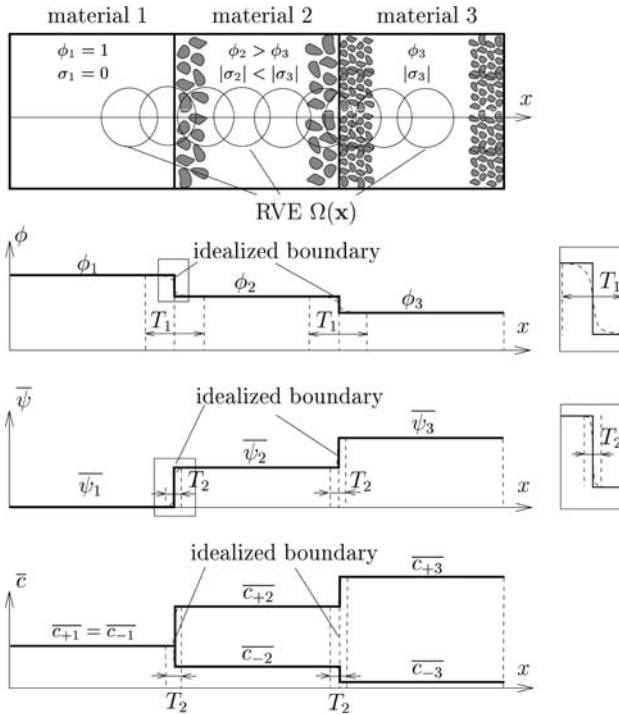


Fig. 2 Macroscopic modeling of phase boundaries: electro-chemical equilibrium between binary electrolytic solution and (negatively) charged porous materials ($\phi_\beta \dots$ porosity of material β ; $\sigma_\beta \dots$ surface charge density of material β ; T_1, T_2 size of transition regions)

By applying the method of volume averaging over an RVE in order to estimate quantities such as the porosity, ion concentration, voltage, and charge density, we note that the latter quantities vary gradually as the averaging “window” (i.e., the RVE) moves along the x -axis. Although we observe rather steep changes in $\phi, \bar{c}_i, \bar{\psi}$, etc. (shown by the dashed lines), no abrupt change occurs. Thus in a continuum sense, sharp boundaries that delineate the different phases at the macroscopic level do not exist anywhere along the x -axis. It is noted that the length of the transition region depends on the physical quantity considered. In the case of electrochemical equilibrium between electrolytic solutions and charged porous materials, the actual transition region for concentrations and voltage (T_2) is at the size of the Debye length (i.e., nanometer range), whereas the transition region for the porosity (T_1) strongly depends on the particle size and distribution within material. T_1 and T_2 may differ by several orders of magnitude.

Variation of any macroscopic quantity (e.g., porosity, concentration, voltage, etc.) over the RVE must be near linear (Bear and Bachmat 1991). If this condition is not satisfied in the region of transition from one material phase to another, as shown for the electrochemical equilibrium in Fig. 2, the actual variation in each quantity in every region of transition should be replaced by an idealized boundary in the form of a surface across which an abrupt change in the quantity takes place. The boundary surface introduced in this way, divides the entire domain into subdomains separated from each other by sharp boundary surfaces. The continuum approach may be applied to

each subdomain using appropriate boundary conditions for each of the subdomains. However, the choice of these boundary conditions strongly depends on the underlying chemo-physical nature of the problem and it is not always straight forward to identify the most suitable approximation at the boundary. For the case of advective-dispersive solute transport through (uncharged) porous materials it has been shown that a phase boundary can be modeled in two ways (see [Peters and Smith 2001](#) for details): (i) application of the governing equations only within each subdomain and prescribing appropriate interface conditions (e.g., concentrations, flux, etc.) and (ii) application of the governing equations across the entire domain and assuming appropriate transition conditions (e.g., continuity of certain quantities). It was demonstrated analytically that both methods deliver the same results if suitable interface boundary conditions and interface transition conditions are chosen ([Peters and Smith 2001](#)).

3 Governing equations describing phase equilibrium

In this section, generalized equations describing phase equilibrium at the macroscale are derived, taking into account the non-homogeneous distribution of microscale quantities. First, we demonstrate analytically that the classical macroscopic equations describing phase equilibrium are not applicable for charged porous materials (Sect. 4.1), and if employed lead to discrepancies in the definition of the Donnan potential (when defined in terms of concentrations). In Sect. 4.2, we then derive new generalized macroscopic equilibrium equations by means of volume averaging of the microscale electrochemical potentials in different material phases.

3.1 Phase equilibrium at the microscale

The theory of thermodynamics provides the framework for the description of equilibrium of ionic species in different phases ([Atkins and de Paula 2002](#)). In the following, we consider phase equilibrium of ionic species between two phases. The distribution of the ions is assumed to be only controlled by differences in concentration and electric potential between the two phases (i.e., we neglect activity and pressure effects). The electrochemical potential of an ionic species in solution is described by ([Newman 1991](#))

$$\mu_{i\beta} = \mu_{i0\beta} + RT \ln c_{i\beta} + z_i F \psi_{\beta}, \quad (4)$$

where the index i refers to the ionic species and the index β refers to the electrochemical phase respectively. $\mu_{i0\beta}$ is a reference electrochemical potential. $c_{i\beta}$ and ψ_{β} are the concentration of ion i and the voltage in the solution phase β . At equilibrium by definition, the electrochemical potentials of the ionic species i is the same in both phases ([Helfferich 1962](#)):

$$\mu_{i1} = \mu_{i2}. \quad (5)$$

An alternative way to define phase equilibrium at the microscale is to state that the gradient of electrochemical potential is zero, i.e.,

$$\nabla \mu_{i\beta} = RT(1/c_{i\beta}) \nabla c_{i\beta} + z_i F \nabla \psi_{\beta} = \mathbf{0}. \quad (6)$$

In order to complete the set of equations describing phase equilibrium at the microscale a relation between the electric potential and the spatial distribution of the

electric charges in a β -phase is required. The most rigorous way to relate the variation of the electric potential to the spatial distribution of the electric charges is by Gauss' electrostatic theorem (also known as Poisson equation) (Newman 1991):

$$-\nabla \cdot (\varepsilon_0 \varepsilon_{\alpha\beta} \nabla \psi_{\alpha\beta}) = \rho_{\alpha\beta} \quad \text{on } \Omega_{\alpha\beta}, \tag{7}$$

where the index α refers to the respective phase in the RVE (i.e., fluid (f) or solid (s) phase) and the index β refers to the electrochemical phase. In the following, we consider solid particles to have only a surface charge. We assume that the voltage and volume charge density is defined over the fluid phase only. Using the short notation, $\psi_{f\beta} = \psi_{\beta}$, $\varepsilon_{f\beta} = \varepsilon_{\beta}$ and $\rho_{f\beta} = \rho_{\beta}$ Eq. 7 can be written as:

$$-\nabla \cdot (\varepsilon_0 \varepsilon_{\beta} \nabla \psi_{\beta}) = \rho_{\beta} \quad \text{on } \Omega_f, \tag{8}$$

where ε_0 is the permittivity of free space, ε_{β} is the relative permittivity of the fluid, and ρ_{β} is the volume charge density of the fluid. The volume charge density of the fluid is linked to the ion concentration in solution as follows:

$$\rho_{\beta} = F \sum_{i=1}^N z_i c_{i\beta}. \tag{9}$$

Use of the Poisson equation assumes that ions are represented as point charges. It is recognized that this assumption may considerably overestimate ion concentrations at the surface of charged particles under some conditions (see Shainberg and Kemper 1966; Iwata et al. 1995; Pivonka and Smith 2004 for details).

The electrostatic boundary conditions applied to a charged particle surface can be expressed as ((Stratton 1941)):

$$\mathbf{D}_f \cdot \mathbf{n}_f = \sigma_{\beta} \quad \text{on } \partial\Omega_{sf} \tag{10}$$

$$\mathbf{D}_f = -\varepsilon_0 \varepsilon_{\beta} \nabla \psi, \tag{11}$$

where \mathbf{D}_f is the electric displacement in the fluid phase respectively. \mathbf{n}_f is the unit normal vector at the solid–fluid interface pointing into the solution.

The system of coupled partial differential Eqs. 6 and 8 must be solved over the domain of the RVE subject to appropriate boundary conditions (see Smith et al. 2004 for details).

3.2 Phase equilibrium at the macroscale

By analogy with the electrochemical potential at the microscale, the electrochemical potential at the macroscale can be expressed as (Helfferich 1962):

$$\overline{\mu_{i\beta}^f} = \overline{\mu_{i0\beta}^f} + RT \ln \overline{c_{i\beta}^f} + z_i F \overline{\psi_{\beta}^f}, \tag{12}$$

where $\overline{\mu_{i0\beta}^f}$ is a reference electrochemical potential of a material β . $\overline{c_{i\beta}^f}$ and $\overline{\psi_{\beta}^f}$ are the (macroscopic) intrinsic (i.e., volume averaged according to Eq. 2) actual concentrations of ion i and the voltage in the material. By definition, at equilibrium the electrochemical potential of the ionic species is the same in both materials (Helfferich 1962):⁴

$$\overline{\mu_{i1}^f} = \overline{\mu_{i2}^f}, \tag{13}$$

⁴ Thermodynamic equilibrium requires equality of temperatures.

where the index i refers to the ionic species and the indices 1, 2 refer to the different materials (for example material 1 may denote an electrolytic solution and material 2 denote a charged porous material). Inserting Eq. 12 into Eq. 13 and assuming the same reference potential leads to the well known Donnan potential between two phases (see Helfferich 1962, pp. 141 for further details):

$$RT \ln \overline{c_{i1}^f} + z_i F \overline{\psi_1^f} = RT \ln \overline{c_{i2}^f} + z_i F \overline{\psi_2^f}, \tag{14}$$

$$z_i F \left(\overline{\psi_2^f} - \overline{\psi_1^f} \right) = -RT \left(\ln \left(\overline{c_{i2}^f} \right) - \ln \left(\overline{c_{i1}^f} \right) \right), \tag{15}$$

$$E_{\text{Don}} := \overline{\psi_2^f} - \overline{\psi_1^f} = -\frac{RT}{z_i F} \ln \left(\overline{c_{i2}^f} / \overline{c_{i1}^f} \right), \tag{16}$$

where $\overline{c_{i1}^f}$, $\overline{c_{i2}^f}$ and $\overline{\psi_1^f}$, $\overline{\psi_2^f}$ indicate the intrinsic actual concentration of ion i and the voltage in the solution and the charged porous medium, respectively. It is noted that use of intrinsic ion concentrations (and not apparent ion concentrations, see Eqs. 1 and 2) in the definition for the Donnan potential (Eq. 16) is essential in order to obtain physical correct voltage. This can easily be seen by applying Eq. 16 to the case of an uncharged porous material where the ion concentration in the fluid phase of the porous material is constant and equal to the ion concentration in the external solution. Applying the definition of intrinsic phase average (Eq. 2) to the (constant) concentration in the pore space of the porous material one obtains $\overline{c_{i2}^f} = \overline{c_{i1}^f}$, which delivers zero Donnan potential as confirmed by experiments. On the other hand, use of the apparent phase average (Eq. 1) delivers $\overline{c_{i2}^f} = \phi_f \overline{c_{i1}^f}$ which in turn gives a non-zero Donnan potential that is not physically correct.

As in the previous section phase equilibrium can be alternatively described by means of zero gradient in electrochemical potential, i.e.,

$$\nabla \overline{\mu_{i\beta}^f} = RT(1/\overline{c_{i\beta}^f})\nabla \overline{c_{i\beta}^f} + z_i F \nabla \overline{\psi_{\beta}^f} = \mathbf{0}. \tag{17}$$

Integration of Eq. 17 across the two materials and rearrangement of terms delivers the expression for the Donnan potential (Eq. 16).

According to Eq. 16, the quantity $(\overline{c_{i2}^f} / \overline{c_{i1}^f})^{1/z_i}$ is equal for all ionic species $i = A, B, \dots, Y$ present in the system, regardless of whether they are counter-ions or co-ions. That is:

$$\left(\overline{c_{A2}^f} / \overline{c_{A1}^f} \right)^{1/z_A} = \left(\overline{c_{B2}^f} / \overline{c_{B1}^f} \right)^{1/z_B} = \dots = \left(\overline{c_{Y2}^f} / \overline{c_{Y1}^f} \right)^{1/z_Y}. \tag{18}$$

The macroscopic Poisson equation is given as:

$$-\nabla \cdot \left(\varepsilon_{\text{eff}\beta} \nabla \overline{\psi_{\beta}^f} \right) = F \sum_{i=1}^N z_i \overline{c_{i\beta}^f} + F \omega \overline{X_{\beta}^f} \tag{19}$$

where $\varepsilon_{\text{eff}\beta}$ is the effective permittivity of the material β at the macroscale. ω is the sign of the fixed charge concentration (i.e., negative for negatively charged materials). $\overline{X_{\beta}^f}$ is the intrinsic fixed charge concentration of the material β (e.g., $\overline{X_{\beta}^f} = 0$ for a pure solution and $\overline{X_{\beta}^f} > 0$ for a charged porous material).

The effective permittivity of the charged porous material can be either estimated from a microscale numerical analysis of a parallel plate capacitor or determined from experimental data. However, it should be noted that the value of the (macroscopic) effective permittivity has almost no influence on the numerical results of the

macroscale analysis as this parameter simply controls the thickness of diffuse-double layers between different materials (such as for example the transition from a pure solution phase to a charged porous material), which is in the range of nanometers. As Eq. 19 is generally applied to domains in the centimeter range, changes in $\epsilon_{\text{eff}\beta}$, even of several orders of magnitude, have no observable macroscopic effect.

The intrinsic fixed charge concentration can be determined (from the microscale) by integration over all charged particle surfaces contained in the RVE in the β -material, i.e.:

$$\overline{X}_\beta^f = \frac{1}{F} \frac{1}{V_f} \int_{S_{sf}} |\sigma_\beta(\mathbf{z})| dS_z, \tag{20}$$

where σ_β is the surface charge density, V_f is the fluid volume, and S_{sf} is the solid–fluid interface of material β .

Having summarized the equations describing phase equilibrium in charged porous materials at the macroscale we want to discuss the important assumption of electroneutrality in Eq. 19. Setting the RHS of Eq. 19 to zero is commonly referred to as electroneutrality condition (or zero charge density condition), i.e.,

$$\sum_{i=1}^N z_i \overline{c}_{i\beta}^f + \omega \overline{X}_\beta^f = 0. \tag{21}$$

It has been demonstrated using asymptotic expansion technique that under certain assumptions the electroneutrality condition is the upscaled form of the Poisson equation (see MacGillivray 1968 for details).

For the special case of a charged porous membrane immersed in a binary electrolytic solution use of the electroneutrality condition allows to give analytical expressions for the cation, anion, and voltage distribution in the Donnan equilibrium model. In the following, we denote $\beta = 1$ as the outside salt solution and $\beta = 2$ as the pore solution of the charged porous material. Given a (mono-monovalent) salt solution of $\overline{c}_{+1}^f = \overline{c}_{-1}^f = \overline{c}^f$ and a surface charge density σ (note that the surface charge concentration \overline{X}^f may be calculated using Eq. 20) we are interested in determining the cation and anion concentration $\overline{c}_{+2}^f, \overline{c}_{-2}^f$ in the charged porous material and the Donnan potential E_{Don} . From Eqs. 16, 18, and 21 we can identify the following three equations:

$$E_{\text{Don}} := \overline{\psi}_2^f - \overline{\psi}_1^f = -(RT/F) \ln (\overline{c}_{+2}^f / \overline{c}_{+1}^f) \tag{22}$$

$$\overline{c}_{+1}^f \overline{c}_{-1}^f = \overline{c}_{+2}^f \overline{c}_{-2}^f \tag{23}$$

$$\overline{c}_{+1}^f - \overline{c}_{-1}^f = 0 \quad \text{and} \quad \overline{c}_{+2}^f - \overline{c}_{-2}^f + F\omega \overline{X}^f = 0 \tag{24}$$

This set of equations can be solved analytically, giving the concentration of cations, anions, and the Donnan potential (see Dähnert and Huster 1999 for details):

$$\overline{c}_{+2}^f = \sqrt{(\overline{X}^f)^2 / 4 + (\overline{c}^f)^2} - \omega \overline{X}^f / 2 \tag{25}$$

$$\overline{c}_{-2}^f = \sqrt{(\overline{X}^f)^2 / 4 + (\overline{c}^f)^2} + \omega \overline{X}^f / 2 \tag{26}$$

$$E_{\text{Don}} = -\frac{RT}{z_i F} \ln (\overline{c}_{i2}^f / \overline{c}^f) \tag{27}$$

As discussed in Sect. 2.2, the macroscopic governing equations (i.e., Eqs. 17 and 19) can be solved in two different ways: (i) application of the governing equations to each subdomain and prescription of concentration and voltage boundary conditions at the interfaces and (ii) application of the governing equations across the entire domain and assuming voltage and concentrations to be continuous across interfaces.

For the numerical analysis in Sect. 5 we employ the second approach. The numerical results will be also compared with the above given analytical expressions.

4 Generalized macroscopic equilibrium equations

For a charged porous material, with known analytical solution of actual ion concentrations in terms of electrostatic potential, we can use the definition of the Donnan potential (Eq. 16) in order to derive an identity for the electrostatic potential. It turns out that for charged porous materials with a non-homogeneous distribution of charge across the domain, two different values of electrostatic potential are obtained. This cannot be correct. As a result of this inconsistency, we derive a new generalized definition of the Donnan potential in terms of “intrinsic effective concentrations,” which yields the same voltage for anions and cations.⁵

4.1 Application of classic Donnan potential to charged porous materials

First we demonstrate analytically that the classical equation describing Donnan equilibrium at the macroscale (Eq. 16) leads to different values of electric potential across two materials depending on the ions considered (i.e., cations or anions). For this purpose, we chose the simplest case of a charged porous material where an analytical expression of the distribution of electric potential and ion concentration in the pore space is known. We consider a porous material having a layered microstructure with surface charge (σ) on each side of the layer (see Fig. 3). We assume that the layer distance between particles (B) is large compared to the thickness of the double layer (λ_D), but small enough to capture non-homogeneous distribution of ion concentrations and electric potential. This assumption justifies a continuum approach. For this configuration, the ion concentration in the pore space follows essentially a 1D Boltzmann distribution (Hunter 2001):

$$c_{i2}(z) = c_{i1} \exp(-w_i(z)/(RT)) \quad (28)$$

with

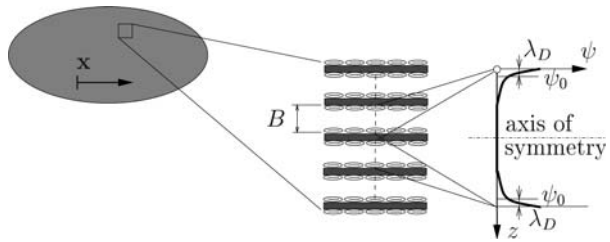
$$w_i(z) = z_i F \psi(z) \quad (29)$$

where c_{i1} is the concentration of ions of type i in the bulk solution far from the charged surface. w_i/N_A is the work done moving an ion to the spatial position z . N_A represents the Avogadro number.

We now apply the intrinsic phase average operation (Eq. 2) for a chosen RVE to the electric potential and ion concentration. The intrinsic phase average of the electric

⁵ In the nomenclature of “intrinsic effective concentrations,” intrinsic refers to the volume averaging procedure, whereas effective refers to the fact that the logarithmic function is applied to the concentration.

Fig. 3 Schematical representation of representative volume element (RVE) of a layered porous material containing same surface charge on each side of the layer



potential is given as:

$$\overline{\psi}_2^f(x) = \frac{1}{V_f} \int_{\Omega(x)} \psi(z) dV_z. \tag{30}$$

Note that ψ is a symmetric function and does not depend on the spatial position of the RVE $\Omega(x)$. For a chosen RVE size ($\ell > B$) the integral (30) delivers the same value for the electric potential across the material, i.e., $\overline{\psi}_2^f = \overline{\psi}_2^f(x) = \text{const}$ (see Fig. 3). Using the intrinsic phase average of the ion concentration (Eq. 28) and using the fact that the ion concentration in the bulk solution is constant leads to:

$$\begin{aligned} \overline{c}_{i2}^f(x) &= \frac{1}{V_f} \int_{\Omega(x)} c_{i2}(z) dV_z \\ &= c_{i1} \frac{1}{V_f} \int_{\Omega(x)} \exp(-z_i F \psi(z) / (RT)) dV_z. \end{aligned} \tag{31}$$

Dividing Eq. 31 by the concentration of the bulk solution (using $c_{i1} = \overline{c}_{i1}^f$) and employing the definition for the Donnan potential (Eq. 16, assuming a zero reference potential $\overline{\psi}_1^f$) leads to:

$$E_{\text{Don}} := \overline{\psi}_2^f = -\frac{RT}{z_i F} \ln \left(\frac{1}{V_f} \int_{\Omega(x)} \exp(-z_i F \psi(z) / (RT)) dV_z \right). \tag{32}$$

Equation 32 should deliver an identity for $\overline{\psi}_2^f$. However, it can be seen that for a given microscopic voltage distribution this equation leads to two different values for the Donnan potential $\overline{\psi}_2^f$ depending on the ion considered (i.e., cations or anions). This is clearly wrong, as from the experiments only one Donnan potential is measured.

4.2 Generalized Donnan potential

The last subsection demonstrated that the classical definition of the Donnan potential leads different values of the electric potential for two different ions. Clearly, we want to find an expression for E_{Don} in terms of concentrations which delivers the same value of electric potential, independent of the type of ion. For this purpose we proceed from the definition of the microscale electrochemical potential (Eq. 4) and apply the intrinsic phase average rule (Eq. 2), that is,

$$\begin{aligned} \overline{\mu}_{i1}^f &= \overline{\mu}_{i2}^f \\ \overline{RT \ln c_{i1} + z_i F \psi_1^f} &= \overline{RT \ln c_{i2} + z_i F \psi_2^f} \\ RT \overline{\ln c_{i1}^f} + z_i F \overline{\psi_1^f} &= RT \overline{\ln c_{i2}^f} + z_i F \overline{\psi_2^f} = \text{const}. \end{aligned} \tag{33}$$

Now we introduce the concept of *intrinsic effective concentrations*, defined here as,

$$\widehat{c}_{i\beta}^{-f} := \exp(\overline{\ln c_{i\beta}^{-f}}), \tag{34}$$

where

$$\overline{\ln c_{i\beta}^{-f}}(\mathbf{x}) = \frac{1}{V_f} \int_{\Omega(\mathbf{x})} \ln(c_{i\beta}(\mathbf{z})) dV_z = \ln \widehat{c}_{i\beta}^{-f}(\mathbf{x}). \tag{35}$$

Equation 33 can then be rearranged to give the generalized Donnan potential:

$$\begin{aligned} E_{\text{Don}} &:= \overline{\psi}_2^{-f} - \overline{\psi}_1^{-f} \\ &= -\frac{RT}{z_i F} \left(\overline{\ln c_{i2}^{-f}} - \overline{\ln c_{i1}^{-f}} \right) = -\frac{RT}{z_i F} \ln \left(\widehat{c}_{i2}^{-f} / \widehat{c}_{i1}^{-f} \right). \end{aligned} \tag{36}$$

This equation is a generalization of Eq. 16 and is valid for any phase equilibrium (with uniform and non-uniform distribution of charge throughout the domain). For the special case where one material is a pure solution (with uniform distribution of charge) characterized by constant (microscopic) concentration and voltage distribution, the relation $\overline{\ln c_{i1}^{-f}} = \ln \overline{c_{i1}^{-f}}$ and, hence, $\widehat{c}_{i1}^{-f} = \overline{c_{i1}^{-f}}$ holds.

In order to demonstrate the validity of Eq. 36, we employ the example problem of a layered charged porous material examined in the previous section. We first determine the intrinsic (average) logarithmic concentration using the Boltzmann concentration distribution function (Eq. 28), i.e.,

$$\begin{aligned} \overline{\ln c_{i2}^{-f}} &= \frac{1}{V_f} \int_{\Omega(x)} \ln c_{i2}(z) dV_z \\ &= \frac{1}{V_f} \int_{\Omega(x)} \ln(c_{i1} \exp(-z_i F \psi(z)/(RT))) dV_z \\ &= \overline{\ln c_{i1}^{-f}} - \frac{z_i F}{RT} \overline{\psi}_2^{-f}. \end{aligned} \tag{37}$$

Inserting the intrinsic logarithmic concentration of material 2 (Eq. 37) into the generalized Donnan potential (Eq. 36), assuming a zero reference voltage $\overline{\psi}_1^{-f}$) gives:

$$\begin{aligned} E_{\text{Don}} &:= \overline{\psi}_2^{-f} \\ &= -\frac{RT}{z_i F} \left(\overline{\ln c_{i2}^{-f}} - \overline{\ln c_{i1}^{-f}} \right) \\ &= -\frac{RT}{z_i F} \frac{1}{V_f} \int_{\Omega(x)} \left(\ln c_{i1} - \frac{z_i F}{RT} \psi(z) - \ln c_{i1} \right) dV_z, \end{aligned} \tag{39}$$

which is an identity that holds for both cations and anions and validates the proposed generalized equation describing Donnan equilibrium.

Now we may again formulate the macroscopic equilibrium equations in terms of the gradient of the electrochemical potential, that is,

$$\nabla \overline{\mu}_{i\beta}^{-f} = RT(1/\widehat{c}_{i\beta}^{-f}) \nabla \widehat{c}_{i\beta}^{-f} + z_i F \nabla \overline{\psi}_\beta^{-f} = \mathbf{0}. \tag{40}$$

Comparing Eq. 16 with the generalized equation for the Donnan potential (Eq. 36) leads one to consider the difference between intrinsic actual concentrations ($\overline{c_{i\beta}^{-f}}$) and

intrinsic effective concentrations ($\overline{\hat{c}}_{i\beta}^f$), or the (absolute) difference between the logarithms of these quantities, i.e.,

$$\left\| \ln \left(\frac{1}{V_f} \int_{\Omega} c_{i\beta}(\mathbf{z}, t) dV_z \right) - \frac{1}{V_f} \int_{\Omega} \ln(c_{i\beta}(\mathbf{z}, t)) dV_z \right\| = \Delta. \tag{41}$$

The value of Δ in Eq. 41 strongly depends on the concentration distribution of $c_{i\beta}$ within the fluid phase of the material β . Δ in Eq. 41 is only zero for constant concentration distribution across the fluid phase of the RVE (i.e., $c_{i\beta} = \text{const}$). For this case the two integrals in Eq. 41 are equal. The assumption of a constant concentration distribution across the fluid phase only holds for uncharged porous materials and porous materials containing a homogeneous distribution of charge. On the other hand, for charged porous materials with non-homogeneous distribution of charge, gradients of concentration (and voltage) across the RVE may be expected, resulting in $\Delta > 0$. For these cases the standard theory (i.e., Eq. 16) breaks down, leading to discrepancies in the value for the Donnan potential. However, for the limiting cases of very low surface charge densities and high ion concentrations in the RVE, the two integrals converge to the same value (indicating nearly constant ion concentrations across the RVE, see Sect. 5 for further discussion).

Having discussed the physical meaning of the generalized Donnan potential, we can conclude that Eq. 36 is a more general definition of the Donnan potential, taking into account the non-homogeneous charge distribution within a porous material phase.

4.3 Generalized macroscopic Poisson equation

We next formulate the counterpart of the Poisson equation (Eq. 19) in terms of effective ion concentration. In order to provide a relation between electric potential and intrinsic effective ion concentration we have to replace the RHS of the (macroscopic) Poisson equation (Eq. 19) by effective quantities, leading a generalized Poisson equation, i.e.,

$$-\nabla(\varepsilon_{\text{eff}\beta} \nabla \overline{\psi}_{\beta}^f) = F \sum_{i=1}^N z_i \overline{\hat{c}}_{i\beta}^f + F \omega \overline{\hat{X}}_{\beta}^f, \tag{42}$$

where $\overline{\hat{c}}_{i\beta}^f$ are the intrinsic effective concentrations (see Eq. 34) and $\overline{\hat{X}}_{\beta}^f$ is an effective fixed charge concentration related to the surface charges σ on particles of the material phase (β). Equilibrium at the macroscale implies electroneutrality within a material (β), and so the RHS of Eq. 42 is zero within the considered material, i.e.,

$$\sum_{i=1}^N z_i \overline{\hat{c}}_{i\beta}^f + \omega \overline{\hat{X}}_{\beta}^f = 0. \tag{43}$$

Once the intrinsic effective concentrations of ions are determined from a microscale analysis, the intrinsic effective fixed charge concentration can be computed using Eq. 43.

With the knowledge of the effective permittivity ($\varepsilon_{\text{eff}\beta}$) and (intrinsic) effective fixed charge concentration ($\overline{\hat{X}}_{\beta}^f$), the generalized macroscopic equations describing phase equilibrium (40) and (42) can be solved numerically. Alternatively, assuming

Table 1 Set of governing equations used for the macroscopic numerical analyses

		Macroscale governing equations			
		Equilibrium Eq.	Poisson Eq.	Variables	Parameters
Classical	Eq. 17	Eq. 19	$\overline{\psi}^f, \overline{c_{i\beta}^f}$	$\varepsilon_{\text{eff}\beta}, \overline{X_\beta^f}$	
Generalized	Eq. 40	Eq. 42	$\overline{\psi}^f, \widehat{c_{i\beta}^f}$	$\varepsilon_{\text{eff}\beta}, \widehat{X_\beta^f}$	

electroneutrality (Eq. 43), the Donnan potential can be computed analytically using Eq. 27 substituting $\widehat{X_\beta^f}$ for $\overline{X_\beta^f}$. For this case concentrations in Eq. 27 have to be interpreted as effective concentrations rather than actual concentrations.

The governing equations describing classical and generalized Donnan equilibrium which are employed for the numerical analyses are summarized in Table 1.

5 Numerical analysis

In this section, we investigate phase equilibrium between two compartments containing a monovalent binary electrolyte (material 1 and 3) separated by a negatively charged porous membrane (material 2) (see Fig. 4).

In order to incorporate (detailed) information from the microscale (such as surface charge density and size and distribution of particles), we apply a hierarchical modeling approach using a macroscale and a microscale model. The geometric dimensions, boundary conditions, and numerical details for both models are discussed below.

The macroscopic system is modeled using both the classical and the new generalized macroscopic governing equations (see Table 1 for details) applied to a 1D

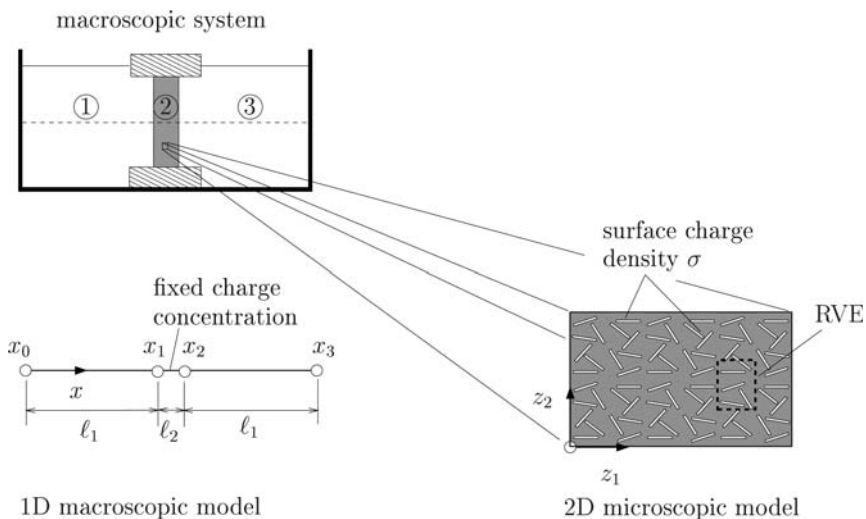


Fig. 4 Equilibrium state: Schematic representation of the employed hierarchical model consisting of a 1D macroscopic model and a 2D microscopic model to describe electrochemical equilibrium in charged porous materials

Table 2 Model parameters used for microscale and macroscale numerical analyses (ε_w : permittivity of pore fluid (i.e., water))

Symbol	Value	Dimension
Microscale model		
ε_0	8.85×10^{-12}	$C^2/(J\ m)$
ε_w	78	–
F	96500	C/mol
T	293	K
R	8.31	$J/(K\ mol)$
Macroscale model		
$\overline{X}_1^f, \overline{X}_3^f$	0	mol/m^3
$\widehat{X}_1^f, \widehat{X}_3^f$	0	mol/m^3
\overline{X}_2^f	3.51	mol/m^3
\widehat{X}_2^f	3.09	mol/m^3
$\varepsilon_{eff1} = \varepsilon_{eff3} = \varepsilon_w \varepsilon_0$	6.90×10^{-10}	$C^2/(J\ m)$
$\varepsilon_{eff2} = 60\varepsilon_0$	5.30×10^{-10}	$C^2/(J\ m)$

geometry (see dashed line in Fig. 4). Numerical results from the macroscale model are compared with the analytical expressions obtained using the electroneutrality condition. In the following, we assign three different β values for the different materials (i.e., $\beta = 1, 3 \dots$ solution phases, $\beta = 2 \dots$ charged porous membrane, see notation in Sect. 3.2 and Fig. 4). The geometric dimensions used for the 1D macroscopic model are $\ell_1 = 4\text{ cm}$ (electrolytic solutions) and $\ell_2 = 1\text{ cm}$ (charged porous membrane). The material parameters required for the macroscale equations are the actual and effective fixed charge concentration and effective permittivity of the solution phases (i.e., $\overline{X}_1^f, \overline{X}_3^f, \widehat{X}_1^f, \widehat{X}_3^f, \varepsilon_{eff1}, \varepsilon_{eff3}$) and the charged porous membrane (i.e., $\overline{X}_2^f, \widehat{X}_2^f$, and ε_{eff2}). The latter two quantities must be estimated from a microscale analysis. Material parameters used for the macroscale model are summarized in Table 2.

At the macroscale a rather fine finite element mesh consisting of 480 quadratic elements has been used. Concentration and voltage boundary conditions are applied at spatial coordinates x_0 and x_3 (i.e., $\overline{c}_1^f(x_0) = \overline{c}_3^f(x_3) = 10\text{ mol/m}^3$ and $\overline{\psi}_1^f(x_0) = \overline{\psi}_1^f(x_3) = 0\text{ V}$, see Fig. 4). At the interfaces (x_1 and x_2) continuity of concentration and voltage is assumed (see discussion on approach 2 for modeling of interfaces, Sects. 2.2, 3.2).

For the microscale analysis we assume the chosen volume element (dashed box in Fig. 4) to be representative (see Sect. 2.1 for choice of RVE) of the microstructure of the material. For simplicity we investigate a 2D microscale domain containing six (randomly distributed) charged particles⁶ of size $100\text{ nm} \times 10\text{ nm}$ (see Fig. 5). The pore geometry (i.e., the particle size and distribution) and surface charge density σ are assumed to be given quantities. The geometry and boundary conditions for the microscale analysis, together with the employed finite element mesh (consisting of 5056 triangular elements with quadratic shape functions), are shown in Fig. 5. The

⁶ The chosen 2D domain might be representative for example for clay materials. However, more complex materials must be modeled using a 3D domain. This is straightforward but computationally more time consuming.

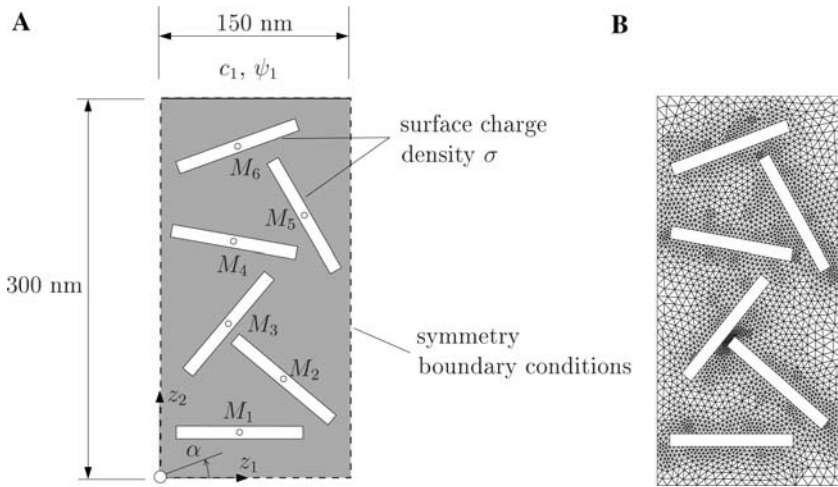


Fig. 5 Equilibrium state—representative volume element(RVE): (a) geometric dimensions together with boundary conditions and (b) finite element mesh (midpoint coordinates ($\times 10^{-7}$ m) and rotation angle α : $M_1 = (0.60, 0.35; 0^\circ)$, $M_2 = (0.98, 0.79; -40^\circ)$, $M_3 = (0.55, 1.21; 50^\circ)$, $M_4 = (0.60, 1.86; -10^\circ)$, $M_5 = (1.12, 2.09; -60^\circ)$, $M_6 = (0.59, 2.60; 20^\circ)$)

material parameters used for the numerical analysis at the microscale are also given in Table 2.

We first demonstrate that the classic Donnan equilibrium model based on volume averaged fixed charge concentrations (\bar{X}^f) leads to an overestimation (in terms of absolute values) of the Donnan potential. This can be shown by using effective fixed charge concentrations (\bar{X}^f) obtained from a microscale analysis. We then demonstrate from a microscale analysis, following a similar approach to that used in the analytical example discussed in Sect. 4.1, that the classical theory describing phase equilibrium (i.e., the Donnan equilibrium model) leads to discrepancies in the definition of the Donnan potential for charged porous materials characterized by a non-homogeneous distribution of charge when combined with a microscale analysis. Use of the generalized Donnan potential resolved this problem. Finally, we perform a parametric study at the microscale showing the dependence of fixed charge concentration on the surface charge density and concentration of background electrolyte.

Assuming that particles of the material contain a constant negative surface charge $\sigma = -0.01 \text{ C/m}^2$ we can use Eq. 20 to determine the fixed charge concentration, i.e., $\bar{X}^f = 3.51 \text{ mol/m}^3$ (with $\omega = -1$). The intrinsic voltage and actual concentration distribution obtained from the numerical analysis is shown in Fig. 6 (dashed lines). Inserting the intrinsic actual concentrations of cations and anions (i.e., $\bar{c}_{+2}^f = 11.91 \text{ mol/m}^3$, $\bar{c}_{-2}^f = 8.40 \text{ mol/m}^3$) into the classical Donnan potential (Eq. 16) delivers an electrostatic potential of $E_{\text{Don}} = -4.4 \text{ mV}$. On the other hand, using an intrinsic effective fixed charge concentration of $\bar{X}^f = 3.09 \text{ mol/m}^3$ we obtain intrinsic (effective) concentrations of cations and anions as $\bar{c}_{+2}^f = 11.67 \text{ mol/m}^3$ and $\bar{c}_{-2}^f = 8.58 \text{ mol/m}^3$, and the electrostatic potential as $E_{\text{Don}} = -3.89 \text{ mV}$. The later value is the correct value for the Donnan potential as will be shown in the next analysis. It should be noted

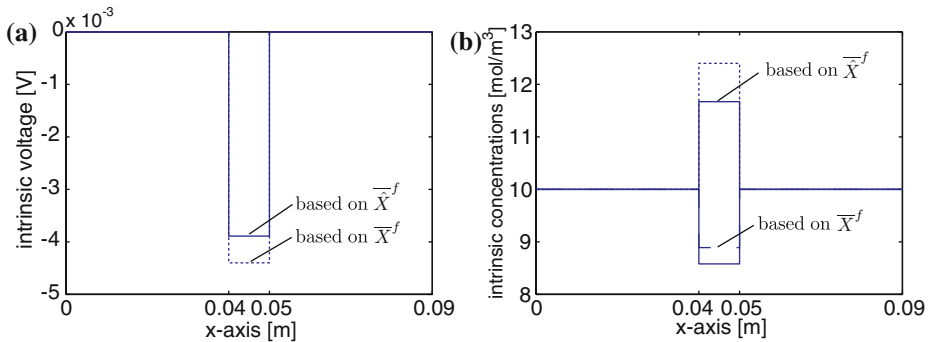


Fig. 6 Equilibrium state—macroscale: distribution of (a) intrinsic voltage and (b) intrinsic cation and anion concentration using actual and effective fixed charge concentrations (for $c_{i1} = 10 \text{ mol/m}^3$ and $\sigma = -0.01 \text{ C/m}^2$)

that the macroscopic concentrations obtained on the basis of effective fixed charge concentration (see Eqs. 25,26) must be interpreted as effective concentrations rather than actual concentrations.

Comparison of the two values for the electrostatic potential indicates that use of actual fixed charge concentration in the Donnan equilibrium model overestimates (in terms of absolute values) the Donnan potential (i.e., $-4.40 \text{ mV} > |-3.89 \text{ mV}$). The reason for this overestimation will be discussed in detail in the following parametric study at the microscale.⁷

Next we use the microscale model to compute intrinsic actual ion concentrations, intrinsic effective ion concentrations, and voltage. The boundary conditions applied for the microscale model are the concentration of background electrolyte (i.e., $c_{i1} = c_1 = 10 \text{ mol/m}^3$), a zero reference potential (i.e., $\psi_1 = 0$), and a negative surface charge density $\sigma = -0.01 \text{ C/m}^2$ (see Fig. 5).⁸ At $(z_1, z_2 = 0)$, $(z_1 = 0, z_2)$, and $(z_1 = 150 \text{ nm}, z_2)$ we apply symmetry conditions. Based on these boundary conditions we compute the intrinsic actual concentrations of cations, anions and voltage as: $\bar{c}_{+2}^f = 12.40 \text{ mol/m}^3$, $\bar{c}_{-2}^f = 8.89 \text{ mol/m}^3$, and $\bar{\psi}_2^f = -3.89 \text{ mV}$). Inserting the intrinsic actual concentration of cations and anions into the Donnan potential (16) delivers two values of the voltage (i.e., $E_{\text{Don},+} = -(RT/F) \ln(\bar{c}_{+2}^f/10) = -5.43 \text{ mV}$ and $E_{\text{Don},-} = (RT/F) \ln(\bar{c}_{-2}^f/10) = -2.96 \text{ mV}$) both which are different from the volume averaged voltage. Obtaining two different values for the Donnan potential is clearly incorrect, as only a single value for voltage is measured. On the other hand, computing the intrinsic effective concentrations of cations and anions (i.e., $\hat{c}_{+2}^f = 11.67 \text{ mol/m}^3$ and $\hat{c}_{-2}^f = 8.58 \text{ mol/m}^3$) and use of the generalized equation describing phase equilibrium (Eq. 36) delivers the same Donnan potential⁹ (i.e., $E_{\text{Don},+} = E_{\text{Don},-} = -(RT/F) \ln(\hat{c}_{+2}^f/10) = (RT/F) \ln(\hat{c}_{-2}^f/10) = -3.89 \text{ mV}$).

⁷ It is noted that the numerical values for macroscopic cation and anion concentration and electric potential deliver the same values as the analytical expressions given in Sect. 3.2

⁸ Boundary conditions applied to the microscale model must be estimated from an initial macroscale analysis. However, for the case of phase equilibrium these boundary conditions are known in advance.

⁹ It should be noted that the accuracy of the FEM calculation at the microscale depends on the employed discretization. At corners of the clay platelets a rather fine FE mesh is required.

Table 3 Evaluation of formulas for Donnan potential based on microscale analysis, $\overline{\psi}^f = -3.89\text{ mV}$

	$\overline{c_{+2}^f}/\overline{c_{+1}^f}$	$\overline{c_{-2}^f}/\overline{c_{-1}^f}$	$\overline{\hat{c}_{+2}^f}/\overline{\hat{c}_{+1}^f}$	$\overline{\hat{c}_{-2}^f}/\overline{\hat{c}_{-1}^f}$
E_{Don} (in mV)	12.40/10	8.89/10	11.67/10	8.58/10
	-5.43	-2.96	-3.89	-3.89

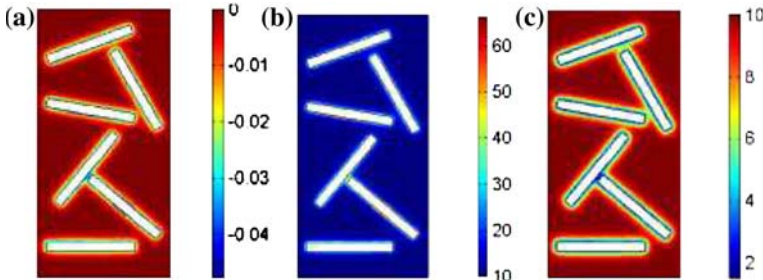


Fig. 7 Equilibrium state—microscale: distribution of (a) voltage (in V), (b) cation concentration (in mol/m³), and (c) anion concentration (in mol/m³) (for $c_{i1} = 10\text{ mol/m}^3$ and $\sigma = -0.01\text{ C/m}^2$)

This value is also identical to the computed intrinsic voltage thereby validating the consistency of the upscaling procedure. The above results are summarized in Table 3.

Figure 7 shows the distribution of voltage, cations, and anions. In the region around a particle the cation concentration is as high as 66.4 mol/m³ (Fig. 7b), whereas the anion concentration is as low as 1.51 mol/m³ (Fig. 7c) indicating that anions are excluded from the porous material. This figure clearly indicates the non-homogeneous distribution of ion concentration and voltage and, hence, of charge across the RVE.

Having demonstrated the validity of the generalized theory describing phase equilibrium at the macroscale, we are now interested in relations between the microscale and macroscale model. As we demonstrated in the first numerical analysis the main input parameter for the macroscale model is the effective fixed charge concentration which must be estimated from a microscale analysis. In the following, we perform a parametric study investigating the dependence of the Donnan potential and fixed charge concentration on the surface charge density and the concentration of background electrolyte. All macroscopic quantities are obtained by intrinsic phase averaging of respective microscale quantities.

Figure 8 shows the dependence of the Donnan potential on the surface charge density (σ) and the concentration of background electrolyte. As for the analytical example (see Sect. 4.1) this figure clearly indicates that use of intrinsic actual cation and anion concentration (i.e., $\overline{c_{+2}^f}$ and $\overline{c_{-2}^f}$) together with the classical Eq. 16 leads to different values for the Donnan potential (i.e., $E_{\text{Don,+}} \neq E_{\text{Don,-}}$). Again this is incorrect, as only a single voltage value is measured. On the other hand, use of intrinsic effective concentrations ($\overline{\hat{c}_{+2}^f}$ and $\overline{\hat{c}_{-2}^f}$) together with Eq. 36 leads to the same value of Donnan potential for cations and anions (i.e., $E_{\text{Don,+}} = E_{\text{Don,-}}$).

As one might expect the difference in values of Donnan potential becomes less pronounced for the case of very low surface charge densities ($\sigma > -10^{-3}\text{ C/m}^2$, see Fig. 8a) and for very high concentration of background electrolyte ($\overline{c_{i1}^f} > 10\text{ mol/m}^3$, see Fig. 8b) both leading to approximately the same ion concentration inside and outside the porous material (i.e., $\overline{c_{i2}^f}/\overline{c_{i1}^f} = 1$ and $\overline{\hat{c}_{i2}^f}/\overline{\hat{c}_{i1}^f} = 1$). In both cases the

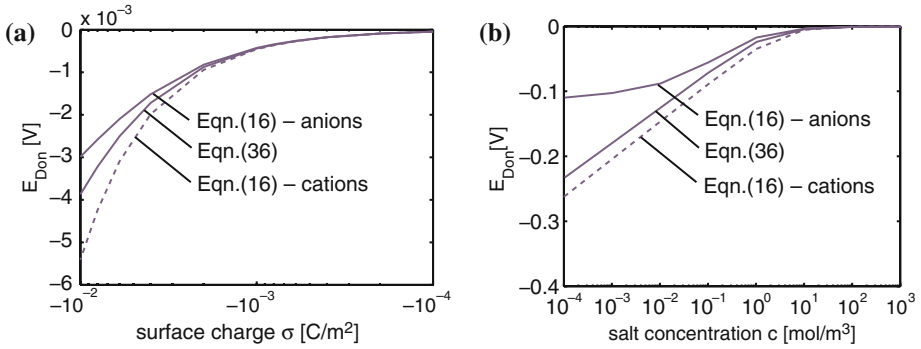


Fig. 8 Equilibrium state—microscale: dependence of Donnan potential ($E_{Don} = \bar{\psi}_2^f$) on (a) surface charge density (for fixed electrolyte concentration $c_{i1} = 10 \text{ mol/m}^3$) and (b) salt concentration (for fixed surface charge density $\sigma = -0.01 \text{ C/m}^2$)

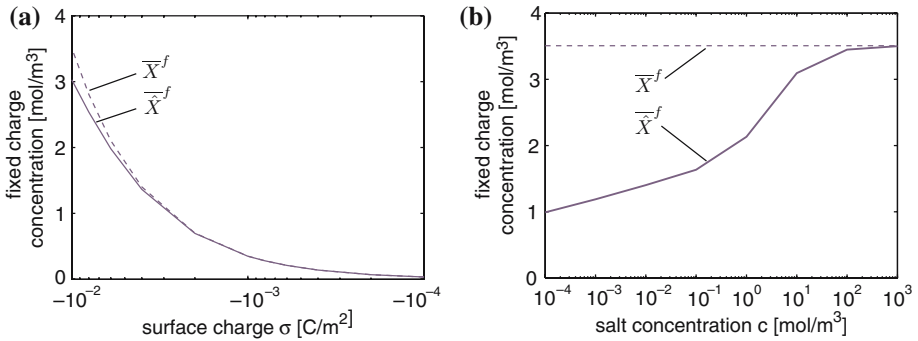


Fig. 9 Equilibrium state—microscale: dependence of fixed charge concentration on (a) surface charge density (for fixed electrolyte concentration $c_{i1} = 10 \text{ mol/m}^3$) and (b) salt concentration (for fixed surface charge density $\sigma = -0.01 \text{ C/m}^2$)

value of Donnan potential converges to its upper/lower bound for a negatively/positively charged porous material, i.e., $E_{Don} = -(RT/F) \cdot \ln 1 = 0 \text{ V}$. For very low surface charge densities the ion distribution approaches the limiting case of an uncharged porous material with constant ion distribution across the fluid phase (see also discussion in Sect. 4.2). On the other hand, high concentration of background electrolyte leads to compression of diffuse-double layers resulting in approximately constant distribution of concentrations in the fluid phase.

Figure 9a shows the dependence of the fixed charge concentration on the surface charge density σ for a constant concentration of background electrolyte of 10 mol/m^3 . As one would expect, decreasing the surface charge density leads to a decrease of fixed charge concentration. Comparison of the actual fixed charge concentration \bar{X}_2^f with the effective fixed charge concentration \hat{X}_2^f shows strong deviations of these two quantities at high surface charge densities. For very low surface charge densities both quantities approach the same value. The actual fixed charge concentration is an upper bound of the effective fixed charge concentration, i.e., $\bar{X}_2^f > \hat{X}_2^f$. This also explains the overestimation of (absolute value of) the Donnan potential in the macroscopic

equilibrium model using actual fixed charge concentration (\overline{X}_2^f) instead of the correct value of effective fixed charge concentration (\overline{X}_2^f) previously discussed.

The dependence of the fixed charge concentration on the background electrolyte concentration for a constant surface charge density of $\sigma = -0.01 \text{ C/m}^2$ is shown in Fig. 9b. From this figure the fundamental difference in definition of fixed charge concentrations can be seen. The actual fixed charge concentration does not depend on the concentration of background electrolyte, i.e., $\overline{X}_2^f = \text{const}$. On the other hand, the effective fixed charge concentration is highly non-linear. Increasing the salt concentration leads to an increase of the effective fixed charge concentration. However, for rather high salt concentrations ($\overline{c}_{i1}^f > 100 \text{ mol/m}^3$), an upper bound of the effective fixed charge concentration of approximately 3.5 mol/m^3 is obtained. This value also corresponds to the actual fixed charge concentration. This case resembles highly compressed diffuse-double layers leading to almost the same electrolyte concentration inside and outside of the porous material (see discussion above on Donnan potential and Fig. 8b).

6 Summary and conclusions

In this article, a new theory for estimating the (macroscopic) Donnan potential in charged porous materials has been proposed. This theory incorporates information from a non-homogeneous charge distribution at the microscale, to macroscale governing equations. The set of macroscopic governing equations comprises the equilibrium equations for different species and the Poisson equation of electrostatics. These equations are derived by consistent upscaling of the microscale governing equations using the volume averaging method. Comparison of the classical macroscale governing equations with the one obtained from upscaling indicate differences in terms of concentration and fixed charge concentration. In the classical equilibrium equations intrinsic voltage is linked to intrinsic actual ion concentrations. On the other hand, the new generalized equilibrium equations relate the intrinsic voltage to so-called intrinsic effective ion concentrations. The intrinsic effective concentrations are, for ideal solutions, related to logarithmic volume averages of concentrations. For the Poisson equation, it turns out that the variation of the electric potential must be related to an effective fixed charge concentration.

The new theory has been verified analytically and numerically for the case of charged porous materials separating two monovalent binary electrolytic solutions of same composition and ion concentration. It has been shown that the new theory is a generalization of the classical theory describing phase equilibrium. For special cases, such as phase equilibrium in uncharged porous materials, very low surface charge densities, and high concentration of background electrolyte, both theories deliver the same results. On the other hand, for non-homogeneous distribution of charge the classical theory fails (leading to inconsistencies in the definition of the Donnan potential). Use of the generalized governing equations resolves this problem.

Additionally, it has been demonstrated that use of the classical Donnan equilibrium model together with actual fixed charge concentration leads to an overestimation of the Donnan potential. On the other hand, use of effective fixed charge concentration leads the correct value for the Donnan potential. A parametric study on the microscale showed that the actual fixed charge concentration is an upper bound of

the effective fixed charge concentration. For this reason the macroscopic electrostatic potential computed from the Donnan equilibrium model based on actual fixed charge concentration leads to an overestimation of the Donnan potential in terms of absolute values.

Clearly, the proposed model may be refined in several ways such as for example using activities rather than concentrations in order to incorporate effects such as high concentrated electrolytic solutions.

Acknowledgments The first author gratefully acknowledge the financial support of this study by the Austrian Foundation for the Promotion of Scientific Research (FWF) in the course of an Erwin Schrödinger scholarship. The authors are also grateful to the Australian Research Council (ARC) for discovery projects funding.

References

- Atkins, P., de Paula, J.: *Atkins' Physical Chemistry*, 7th edn. Oxford University Press, New York, USA (2002)
- Basser, P.J., Grodzinsky, A.J.: The Donnan model derived from microstructure. *Biophys. Chem.* **46**, 57–68 (1993)
- Bear, J., Bachmat, Y.: *Introduction to Modelling of Transport Phenomena in Porous Media*, vol. 4. Kluwer Academic Publishers, Dordrecht, The Netherlands (1991)
- Dähnert, K., Huster, D.: Comparison of the Poisson–Boltzmann model and the Donnan equilibrium of a polyelectrolyte in salt solution. *J. Colloid Interface Sci.* **215**, 131–139 (1999)
- Dormieux, L.: A mathematical framework for upscaling operations. In: Dormieux, P., Ulm, F. (eds.) *Applied Micromechanics of Porous Materials*. Springer, New York, CISM series (Nr.480) (2005)
- Helfferich, F.: *Ion exchange*. McGraw-Hill, New York, USA, Series in Advanced Chemistry (1962)
- Hunter, R. J.: *Foundations of Colloid Science*. Oxford University Press, Oxford, UK (2001)
- Iwata, S., Tabuchi, T., Warkentin, B. P.: *Soil–water Interactions*. Marcel Dekker, New York, USA (1995)
- MacGillivray, A.D.: Nernst–Planck equations and the electroneutrality and Donnan equilibrium assumptions. *J. Chem. Phys.* **48**, 2903–2907 (1968)
- Newman, J. S.: *Electrochemical Systems*, 2nd edn. Prentice-Hall, Englewood Cliffs, NJ, USA (1991)
- Peters, G., Smith, D.: Numerical study of boundary conditions for solute transport through a porous medium. *Int. J. Numer. Anal. Met. Geomech.* **25**, 629–650 (2001)
- Pivonka, P., Smith, D.: Investigation of nanoscale electrohydrodynamic transport phenomena in charged porous materials. *Int. J. Numer. Met. Eng.* **63**, 1975–1990 (2004)
- Shainberg, I., Kemper, W. D.: Hydration status of adsorbed ions. *Soil Sci. Soc. Am. Proc.* **30**, 707–713 (1966)
- Smith, D., Pivonka, P., Jungnickel, C., Fityus, S.: Theoretical analysis of anion exclusion and diffusive transport through platy-clay soils. *Transport Porous Media* **57**, 251–277 (2004)
- Sposito, G.: *The Chemistry of Soils*. Oxford University Press, New York, USA (1989)
- Stratton, J. A.: *Electromagnetic Theory*. McGraw-Hill, New York, USA (1941)
- Westermann-Clark, G. B., Christoforou, C. C.: The exclusion-diffusion potential in charged porous membranes. *J. Electroanal. Chem.* **198**(1986), 213–231 (1986)
- Whitaker, S.: *The Method of Volume Averaging*, vol. 13. Kluwer Academic Publishers, Dordrecht, The Netherlands (1999)
- Zaoui, A.: Structural morphology and constitutive behavior of micro-heterogeneous materials. In: Suquet, P. (ed.) *Continuum Micromechanics*. Springer, New York, CISM courses and lectures No. 377 (1997)

B. Gardiner, D. Smith, **P. Pivonka**, A. Grodzinsky, E. Frank, L. Zhang. Solute transport in cartilage undergoing cyclic deformation. *Computer Methods in Biomechanics and Biomedical Engineering*, 2007. (in print)

Author Queries

JOB NUMBER: MS 230818

JOURNAL: GCMB

- Q1** We have inserted a short title. Please approve or provide an alternative.
- Q2** Please supply received, revised and accepted dates.
- Q3** We have inserted a minimum of 4 keywords as per the journal style. Please approve or provide an alternative.
- Q4** Equations (3.13.3) are cited in the text but not provided. Please remove the citations or provide the equations.
- Q5** Figure 5 is in poor quality. Please provide better quality figure.

Solute transport in cartilage undergoing cyclic deformation

BRUCE GARDINER^{†*}, DAVID SMITH^{†¶}, PETER PIVONKA^{†§}, ALAN GRODZINSKY^{‡||}, ELIOT FRANK^{‡##} and
LIHAI ZHANG^{†**}

[†]Department of Civil and Environmental Engineering, Centre for Biomedical Engineering, The University of Melbourne, Melbourne, Vic. 3010, Australia

[‡]Department of Electrical Engineering and Computer Science, Department of Mechanical Engineering, Center for Biomedical Engineering, Massachusetts Institute of Technology, Cambridge, MA, USA

(Received ■; revised ■; in final form ■)

There are no blood vessels in cartilage to transport nutrients and growth factors to chondrocytes dispersed throughout the cartilage matrix. Insulin-like growth factor-I (IGF-I) is a large molecule with an important role in cartilage growth and metabolism, however, it first must reach the chondrocytes to exert its effect. While diffusion of IGF-I through cartilage is possible, it has been speculated that cyclic loading can enhance the rate of solute transport within cartilage. To better understand this process, here a one-dimensional axisymmetric mathematical model is developed to examine the transport of solutes through a cylindrical plug of cartilage undergoing cyclic axial deformation in the range of 10^{-3} –1 Hz. This study has revealed the role of timescales in interpreting transport results in cartilage. It is shown that dynamic strains can either enhance or inhibit IGF-I transport at small timescales (<20 min after onset of loading), depending on loading frequency. However, on longer timescales it is found that dynamic loading has negligible effect on IGF-I transport. Most importantly, in all cases examined the steady state IGF-I concentration did not exceed the fixed boundary value, in contrast to the predictions of Mauk *et al.* (2003).

Keywords: Insulin-like growth factor-I (IGF-I); Cartilage; Cyclic deformation; Chondrocytes

1. Introduction

Articular cartilage is found at the end of long bones within synovial joints. Its main functions appear to be to reduce contact pressures between opposing bones and to provide a low-wear contacting surface. Articular cartilage is prone to damage through abrasion or tearing if the joint is subjected to unusual loads or deformations, such as those potentially encountered in many sports or in motor vehicle accidents. Unlike neighboring bone, cartilage's ability to repair itself is extremely limited. Once damaged through injury or disease it generally degenerates toward the common and often debilitating disorder—osteoarthritis. The degeneration of cartilage indicates an imbalance in the anabolic and catabolic activities of the chondrocyte. Chondrocyte metabolism is regulated by a large number of factors ranging from the physiochemical environment

(van den Berg *et al.* 2001, Shieh and Athanasiou 2003) to the mechanical environment (Kim *et al.* 1994, Quinn *et al.* 1998, Grodzinsky *et al.* 2000, Li *et al.* 2000, 2001, Silver and Bradica 2002).

It is known that extracellular matrix (ECM) production in cartilage is enhanced when the cartilage is subjected to small dynamic strains ($\leq 10\%$ compressive strain) at physiologically relevant frequency ranges (0.002–1 Hz) (Kim *et al.* 1994, Buschmann *et al.* 1999, Grodzinsky *et al.* 2000, Li *et al.* 2001) and inhibited when subjected to static compressive loads (Grodzinsky *et al.* 2000). Furthermore, experiments (Kim *et al.* 1994, Buschmann *et al.* 1999) have revealed that the spatial distribution of the biosynthetic response of chondrocytes varies as a function of loading frequency, suggesting that the chondrocytes are influenced by dynamic changes in fluid flow within the cartilage. It has been speculated that not only do

*Corresponding author. Tel.: +61-3-83446932. Fax: +61-3-83444616. Email: bgardine@unimelb.edu.au

¶Tel.: +61-3-83444061. Fax: +61-3-83446215. Email: david.smith@unimelb.edu.au

§Tel.: +61-3-83446932. Fax: +61-3-83444616. Email: ppivotka@unimelb.edu.au

||Tel.: +1-617-2534969. Fax: +1-617-2585239. Email: alg@mit.edu

#Tel.: +1-617-253-0295. Fax: +1-617-2585239. Email: ehfrank@mit.edu

**Tel.: +61-3-83446932. Fax: +61-3-83444616. Email: l.zhang@civenv.unimelb.edu.au

chondrocytes respond to fluid shear, but they may also be responding to potentially-enhanced transport of nutrients, such as the insulin-like growth factor (IGF-I), by the cyclic loading-induced fluid motion (Kim *et al.* 1994, Buschmann *et al.* 1999, Bonassar *et al.* 2001). For example, IGF-I has been shown to increase ECM production and there appears to be a synergistic effect of IGF-I and dynamic loading on ECM production (Bonassar *et al.* 2000, Grodzinsky *et al.* 2000, Li *et al.* 2001), potentially due to enhanced IGF-I transport under cyclic loading conditions.

In vitro, IGF-I has been found to increase chondrocyte numbers and the production of the various constituents of cartilage matrix (Osborn *et al.* 1989). Although IGF-I is synthesized in many tissues, it is predominantly produced by the liver (Sara and Hall 1990) and circulates throughout the body in the blood. As articular cartilage is avascular, nutrient transport to chondrocytes and waste product transport out of the cartilage must be done through *advection–diffusion transport* through the ECM. However, IGF-I is a large molecule (7.6 kDa) and so does not easily diffuse, suggesting a potentially important role for advective transport.

The question then naturally arises; Does cyclic loading enhance the transport of solutes in cartilage?

2. Previous experimental and theoretical studies of nutrient transport in dynamically loaded cartilage

A summary of relevant experimental and theoretical studies of neutral solute transport into articular cartilage (and intervertebral discs) undergoing cyclic loading can be found in tables 1 and 2.

In an experimental study by O'Hara *et al.* (1990) the desorption of solutes of various sizes through articular cartilage subjected to a square wave cyclic loading of 2.8 MPa at 1 Hz was investigated over a period of 60 min. They found that for small solutes, such as urea (60 Da) and NaI, cyclic loading did not influence the transport of solutes and that free diffusion was dominant. However for the larger solute, serum albumin (68 kDa), the rate of transport was increased by 30–100% by cyclic loading. Note, IGF-I at 7.6 kDa falls within the transition between these two molecular size ranges.

Quinn *et al.* (2002) performed radial desorption experiments on 2.7 mm diameter cartilage discs undergoing axial compression. Results from both static compression (0–46% strain) and cyclic loading (23% static strain \pm 5% dynamic strain amplitude at 0.001 Hz) experiments were presented. Although static results were obtained for Dextran (a complex branched polysaccharide) of two molecular weights 3 and 40 kDa, cyclic loading results were only shown for the 3 kDa Dextran. It was observed that after 1 h of cyclic loading (i.e. only 3.6 loading cycles), the solute desorption had been augmented in comparison to cartilage discs held at 15 and 31% static strains levels. Of note was that this augmentation was only found in the 0.5 mm region near the edge of the cartilage and that the solute profile near this edge had a distinct concave shape.

Bonassar *et al.* (2001) performed radial absorption experiments with IGF-I. In particular a 1 mm thick, 3 mm diameter cartilage disc was subjected to a 2% sinusoidal strain at 0.1 Hz (no static compression). IGF-I take-up by the cartilage was recorded using a radio-labeled IGF-I, such that they effectively recorded a volume-averaged IGF-I concentration. They concluded that cyclic loading significantly increased the rate of IGF-I transport, compared to a control (unloaded) cartilage disc, over a time period of approximately 30 h. Note this timescale is much longer than the 60 min duration of the experiments results discussed previously (O'Hara *et al.* 1990, Quinn *et al.* 2002). Furthermore, they found that a steady state concentration of IGF-I was reached after approximately 40 h in both the loaded and control cartilage sample. The steady state concentration was independent of loading.

Recently, Mauck *et al.* (2003) presented a one-dimensional (1D), axisymmetric porous media model of radial neutral solute transport in various tissues undergoing axial dynamic compressive loading. Results were presented for timescales sufficient for solute absorption to reach a steady state. They predicted that dynamic loading can concentrate a solute inside the tissue to levels well above the boundary concentrations, particularly for large strains (up to 20%) and high frequencies (approximately, 1 Hz). Hence, from their results it could be concluded that dynamic loading can intensify the solute concentration inside cartilage, thereby offering a new mechanism for enabling chondrocytes to detect and respond to an applied load. Note Mauck *et al.*'s study did not include charged

Table 1. Review of experimental studies of solute transport in cyclically loaded cartilage.

Study	Type	Solute	Load/strain	Frequency (Hz)	Timescale	Enhanced transport
O'Hara <i>et al.</i> (1990)	Desorption	Urea 60 Da	2.8 MPa	1	60 min	No
	Desorption	NaI	2.8 MPa	1	60 min	No
	Desorption	Ser. Alb. 68 kDa	2.8 MPa	1	60 min	Yes
Quinn <i>et al.</i> (2002)	Desorption	Dextran 3 kDa	10%	0.001	60 min	Yes
Mauck <i>et al.</i> (2003)	Absorption	IGF-I 7.6 kDa	2%	0.1	2–3 days	Yes

Q1

Table 2. Review of theoretical studies of solute transport in cyclically loaded cartilage.

Study	Type	Solute	Load/strain (%)	Frequency (Hz)	Timescale	Enhanced transport
Mauck <i>et al.</i> (2003)	1D model	Various	0–20	0.01–1	2–3 days	Yes
Zhang and Szeri (2005)	Absorption	400 Da	20	Unclear	100 min	Yes/no
	Desorption	3 kDa	10	0.001	60 min	–
	Absorption	400 kDa	20	Unclear	100 min	Yes
Ferguson <i>et al.</i> (2004)	2D model	400 Da	0.5 MPa/11	10^{-5}	24 h	No
	Absorption	40 kDa	0.5 MPa/11	10^{-5}	24 h	Yes

species, sources or sinks for the solute or compressibility of any of the phases (solid, fluid or solute). Furthermore, terms involving osmotic effects and the Poisson's ratio were assumed to be negligible. From an engineering viewpoint, it is then quite peculiar that the solute concentration inside the cartilage was able to rise to, in some cases, three times the boundary concentrations. Note, no indication of solute concentration exceeding boundary levels has been observed in the only long time span experiments (Bonassar *et al.* 2001). Consequently, one of the secondary, yet important, goals of the current paper is to reexamine Mauck *et al.*'s prediction with a simple, phenomenological model of the same system.

Zhang and Szeri (2005) recently presented a 1D, porous media model for solute transport in cartilage. Unlike the previously-discussed experiments and model, Zhang and Szeri considered axial, rather than radial, solute transport, with axial loading. That is, the solute absorption was in the same direction as the loading. In addition to the new geometry, their model differs from that of Mauck *et al.* (2003) mainly through the use of a strain dependent diffusion coefficient and hydraulic permeability. Absorption was considered over a 100 min time span, for two molecule sizes, 400 Da and 400 kDa, and model predictions were also presented for comparison with the 3 kDa experiment of Quinn *et al.* (2002). Only quite large dynamic strain of 20% were considered and the loading frequency used was not explicitly stated in the paper. Their main conclusion was that, solute transport was enhanced for the 400 kDa solutes, with negligible effect for the 400 Da solute. Enhancement was greatest near the edge of the cartilage. Interestingly, for the 400 Da solute their results indicate a slight inhibition of solute transport at deeper layers within the cartilage. Unfortunately, no direct comparison could be made from the figures provided to decide whether or not their model could reproduce the enhanced transport for 3 kDa observed in Quinn *et al.* (2002). Furthermore, no attempt was made by Zhang and Szeri to distinguish between the effects of including a strain-dependent diffusion coefficient, a strain-dependent permeability and the loading-induced fluid motion.

In a related model, Ferguson *et al.* (2004) formulated a two-dimensional, multi-layered model for the transport of solutes of size 400 Da and 40 kDa in intervertebral discs

undergoing diurnal loading. Reminiscent of Zhang and Szeri (2005), a strain dependent permeability was used, but only a constant diffusion coefficient. By formulating a multi-layered model Ferguson *et al.* have constructed a model in which there is anisotropy in both the ECM stiffness and permeability. They conclude that the cyclic loading had only a minor effect on the smaller molecules but did result in a net transport of around 30% over a diurnal cycle for the larger molecules. Note, in the model of Ferguson *et al.* (2004) the diurnal loading frequency ($\sim 10^{-5}$ Hz) is significantly lower than that we will consider here 0.001–1 Hz, and those frequencies used in the cartilage experiments of Bonassar *et al.* (2000), Grodzinsky *et al.* (2000) and Li *et al.* (2001).

It can be seen from the above discussion (summarized in tables 1 and 2) that although a fairly wide range of solute sizes, applied loads/strains and frequencies have been used, it is generally reported that transport is enhanced due to cyclic loading, with the effect being greatest for larger molecules (though several papers report no effect). This size effect is hardly surprising as the larger molecules do not diffuse as easily as smaller molecules, and so advective transport would tend to dominate diffusional transport.

There is, however, some inconsistency in the details of these experiments and models. First, two quite distinct timescales are examined—of the order of 1 h and of the order of 2–3 days. One of the key findings from the current paper is that these two timescales can display quite distinct behaviors, as will be discussed in Section 6 in the context of our model predictions. Certainly the transition between these two timescales has not been adequately explored. Second, the theoretical models have tended toward higher dynamic strains (>10%) than those used in the experiments on chondrocyte synthesis (Kim *et al.* 1994, Grodzinsky *et al.* 2000, Li *et al.* 2001) or studies of enhanced transport (Bonassar *et al.* 2001, Quinn *et al.* 2002). Furthermore, the strains of 20% used in the models of Mauck *et al.* (2003) and Zhang and Szeri (2005) arguably exceed the small strain assumption employed. It is important then to reexamine the potential role that dynamic loading has in experiments, and alternatively whether or not current 1D models are capable of predicting enhanced transport under the experimental conditions.

In this paper, we develop a mathematical model for the transport of neutral solutes through a cylindrical

articular cartilage disc. In keeping with experiments (Bonassar *et al.* 2000, 2001, Li *et al.* 2001) involving IGF-I and dynamically loaded articular cartilage we will consider dynamic strains of 2% at 0.1–1 Hz (e.g. load cycle at a walking pace). However, we will also extend this frequency range down to 0.001 Hz to examine the potential contribution to IGF-I transport of altering between standing and sitting over a 20 min cycle and to enable reflection on the experiments of Quinn *et al.* (2002). In the next section three-dimensional governing equations for solute transport in porous media are presented. Section 5 then simplifies these governing equations for the specific geometry of radial transport in axial loaded cylindrical disc undergoing cyclic deformations. Then the predictions of the model for various loading frequencies will be presented and discussed. In particular, we will demonstrate model predictions at two distinct timescales. First, consider short timescales, < 20 min. Then we will consider a time scale of approximately 2–3 days (here referred to as a long timescale), which is the approximate time needed for a steady state conditions for diffusion of IGF-I through 1 mm of cartilage. We will see that these two timescales are characterized by quite disparate behaviors. We then examine the flow of fluid within cartilage for a range of applied strains and frequencies, and the cartilage matrix properties of stiffness and permeability. We consider the effect of experimental design on interpreting enhanced transport results (specifically the assumption of a well-mixed bath). Finally, we consider the theoretical results presented here in relation to those presented in previous papers.

3. Solute transport in a deforming porous media

In the following section, a model will be produced for the deformation of articular cartilage which will include the mass transport of interstitial fluid and a dissolved solute. The model is based on the porous media (or mixture) theory approach, in which the heterogeneity of the material is ignored and only the relative volume ratios of the various phases are important, along with a general form of their interactions. Using this abstraction, the model presented here may be applied to other biological tissues, just as it has been applied to other engineering systems (e.g. mechanical consolidation of geomaterials (Bear and Bachmat 1991, Verruijt 1995, Smith 2000, Peters and Smith 2002)). In fact the theory of mechanical consolidation was developed first by Biot (1941) and Terzaghi (1943) to describe the deformation and load characteristics of clay and soil systems. The use of porous media theory to model cartilage (and other biological tissues (De Angelis and Preziosi 2000, Lemon *et al.* 2006)) is not a recent idea (Mow *et al.* 1980), with many examples of cartilage models based on porous media theory found in the literature (Lai *et al.* 1991, Gu *et al.* 1998, Klisch *et al.* 2003, 2005, Mauck *et al.* 2003, Zhang and Szeri 2005).

In the model employed here, cartilage is considered to be a homogenous three-phase mixture consisting of a solid, a liquid and a solute. The solid component is comprised of the various proteins, polysaccharides, etc. in the ECM as well as the chondrocytes. The liquid phase represents the interstitial fluid. The solute phase of primary interest in this paper is IGF-I, although the model can be applied to other neutral solutes as well. The concentration of each of these phases in cartilage is then defined by

$$\bar{c}^\alpha = \frac{n^\alpha}{V} \quad (1)$$

where n^α is the number of moles of the α phase in the mixture volume element V . The volume fraction of each phase is commonly defined as

$$\phi^\alpha = \frac{V^\alpha}{V} \quad (2)$$

where V^α is the volume of the α phase. Hence, we see that in the volume element V

$$c^w = \frac{\bar{c}^w}{\phi^f} \quad (3)$$

where c^w denotes the concentration of solute relative to the fluid volume. Note, here the superscripts s , f and w are used to refer to the solid, fluid and solute phases, respectively. Assuming the cartilage is entirely composed of the three phases identified (i.e. a solid, liquid and solute phase), the sum of all phase volume fractions is equal to one. However, we can further assume that the solute does not change the volume of the mixture, such that $\phi^w \cong 0$. The density (known as the *true density* or the *intrinsic density*) of the solid and fluid phase may now be expressed in terms of the phase volume fraction, i.e.

$$\rho^\alpha = \frac{m^\alpha}{V^\alpha} = \frac{m^\alpha}{\phi^\alpha V} \quad (4)$$

Hence, the mass balance for each component in the mixture is

$$0 = \frac{\partial(\phi^s \rho^s)}{\partial t} + \nabla(\phi^s \rho^s \mathbf{v}^s) \quad (5)$$

$$0 = \frac{\partial(\phi^f \rho^f)}{\partial t} + \nabla(\phi^f \rho^f \mathbf{v}^f) \quad (6)$$

$$0 = \frac{\partial(\phi^f c^w)}{\partial t} + \nabla(\phi^f c^w \mathbf{v}^w) \quad (7)$$

where \mathbf{v}^α is the velocity of each phase relative to an external inertial frame of reference. Note, consistent with the previous models here we have assumed that there is no sorption or transport of solute on the solid phase. From (5) and (6) the mass balances for an incompressible (constant true density), isotropic solid

and fluid are

$$0 = -\frac{\partial \phi^f}{\partial t} + \nabla \cdot ((1 - \phi^f) \mathbf{v}^s) \quad (8)$$

$$0 = \frac{\partial \phi^f}{\partial t} + \nabla \cdot (\phi^f \mathbf{v}^f) \quad (9)$$

Hence from (8) and (9) we can obtain

$$0 = \nabla \cdot ((1 - \phi^f) \mathbf{v}^s + \phi^f \mathbf{v}^f) \quad (10)$$

The fluid phase velocity relative to the solid phase velocity is assumed to be proportional to the gradient of fluid pressure (Darcy's law), and is referred to here as the Darcy velocity \mathbf{v}_d . That is,

$$\mathbf{v}_d = \phi^f (\mathbf{v}^f - \mathbf{v}^s) = -k \nabla p \quad (11)$$

where k is often called the hydraulic permeability (or hydraulic conductivity), and is the ratio of the intrinsic permeability of the porous material and the viscosity of the fluid. Hence, from (10) and (11) we find

$$0 = \nabla \cdot (\mathbf{v}^s - k \nabla p) \quad (12)$$

The solid phase is assumed to obey the equilibrium equations, viz,

$$0 = \nabla \cdot \boldsymbol{\sigma} \quad (13)$$

where $\boldsymbol{\sigma}$ is the total stress tensor (Verruijt 1995). Equation (13) is valid in the absence of body forces and when inertial effects are negligible. For small strains, the solid phase can be considered to be isotropic linear elastic. Under this assumption the stress in the solid/fluid mixture is given by Terzaghi (1943), Mow *et al.* (1980) and Verruijt (1995)

$$\boldsymbol{\sigma} = -p \mathbf{I} + \lambda_s (\text{tr} \boldsymbol{\varepsilon}) \mathbf{I} + 2\mu_s \boldsymbol{\varepsilon} \quad (14)$$

where $\boldsymbol{\varepsilon}$ is the infinitesimal strain tensor defined by

$$\boldsymbol{\varepsilon} = \frac{1}{2} (\nabla \mathbf{u}^s + (\nabla \mathbf{u}^s)^T) \quad (15)$$

The equations of equilibrium (equation (13)), the constitutive law (equations (14) and (15)) and the following vector identity ($\nabla \cdot (\nabla \cdot \mathbf{b}) \equiv \nabla \times \nabla \times \mathbf{b} + \nabla^2 \mathbf{b}$) combine to give

$$-\nabla p + H_A \nabla \cdot (\nabla \cdot \mathbf{u}^s) - \mu_s \nabla \times (\nabla \times \mathbf{u}^s) = 0 \quad (16)$$

where $H_A = \lambda_s + 2\mu_s$ and $\mathbf{v}^s = (\partial \mathbf{u}^s / \partial t)$. Note, although commonly employed, the assumptions of isotropic linear elasticity used to obtain (16) must be considered as only a first approximation, as it has been previously shown that there is an asymmetry in the cartilage fluid pressures under tension and compression when the effects of fibril stiffening are accounted for Li *et al.* (2001).

Equations (12) and (16) are used to describe the mechanical behavior of a deforming porous media (or in this case, cartilage).

Returning to (7), Fick's law for the flux of the solute in cartilage is

$$\bar{c}^w (\mathbf{v}^w - \mathbf{v}^f) = -\phi^f D \nabla c^w \quad (17)$$

where D is the diffusion coefficient for the solute in the cartilage and takes into account the tortuosity of the cartilage matrix. Equation (7) along with (11) and (17) lead to

$$0 = \frac{\partial (\phi^f c^w)}{\partial t} + \nabla \cdot (c^w (\phi^f \mathbf{v}^s - k \nabla p) - \phi^f D \nabla c^w) \quad (18)$$

It is timely to note that (9) and (11) provide the following relationship,

$$0 = \frac{\partial \phi^f}{\partial t} + \nabla \cdot (\phi^f \mathbf{v}^s - k \nabla p) \quad (19)$$

Using (19) and the vector identity, $\nabla \cdot (\mathbf{a} \mathbf{b}) \equiv \mathbf{b} \cdot \nabla \mathbf{a} + \mathbf{a} \nabla \cdot \mathbf{b}$, we can simplify (18) to

$$0 = \frac{\partial c^w}{\partial t} - D \nabla^2 c^w + (\mathbf{v}^s - \frac{k}{\phi^f} \nabla p - \frac{1}{\phi^f} \nabla \cdot (\phi^f D)) \nabla c^w \quad (20)$$

If it is assumed that the solid phase displacement is identical to the cartilage matrix displacement, then the cartilage volumetric strain ϵ_v is given by the divergence of the solid phase displacement,

$$\epsilon_v = \nabla \cdot \mathbf{u}^s \quad (21)$$

For small strains

$$\phi^f = \phi_0^f + \epsilon_v \quad (22)$$

where ϕ_0^f represents the initial fluid volume fraction. Assuming an initially homogeneous cartilage (i.e. there are no initial spatial gradients in ϕ^f) then we may obtain

$$\nabla (D \phi^f) = \nabla (D \nabla \cdot \mathbf{u}^s) \quad (23)$$

such that (20) may be written as

$$0 = \frac{\partial c^w}{\partial t} - D \nabla^2 c^w + \left(\mathbf{v}^s - \frac{k}{\phi^f} \nabla p - \frac{1}{\phi^f} \nabla (D \nabla \cdot \mathbf{u}^s) \right) \nabla c^w \quad (24)$$

Hence, assuming an isotropic diffusion coefficient, we can use (16) to express (24) as

$$0 = \frac{\partial c^w}{\partial t} - D \nabla^2 c^w + \left(\mathbf{v}^s - \frac{k}{\phi^f} \left(1 + \frac{D}{H_A k} \nabla p \right) - \frac{\mu_s D}{\phi^f H_A} \nabla \times (\nabla \times \mathbf{u}^s) \right) \nabla c^w \quad (25)$$

For the 1D problem to be considered in the following section, we will see that (25) can be further simplified (due to initial homogeneity of the sample and under unconfined compression conditions the deformation is irrotational $\nabla \times \mathbf{u}^s = 0$) to

$$0 = \frac{\partial c^w}{\partial t} - D \nabla^2 c^w + \left(\mathbf{v}^s - \frac{k}{\phi^f} \left(1 + \frac{D}{H_A k} \right) \nabla p \right) \nabla c^w \quad (26)$$

Equation (25) is the solute transport equation for a deforming porous media. Together, equations (12), (16) and (25) form the set of governing equations for the movement of the various phases in a three phase material.

Q4 These equations are equivalent to equations (3.1)–(3.3) of Zhang and Szeri (2005), if their strain-dependent diffusion coefficient and permeability are neglected, despite the difference in the method of derivation. We can see that the second term in (25) is the contribution to solute transport from free diffusion. The third term is the contribution to solute transport from fluid motion (advection) as well as changes in the fluid volume fraction, in our case, induced by cyclic deformations. Note these governing equations were developed using a spatial (external) coordinate system. Due to the choice of coordinate system there is (perhaps) an unexpected term in the transport equation. The advection term depends on the solid phase velocity \mathbf{v}^s , not just the fluid velocity relative to the solid velocity—the Darcy velocity $k \nabla p$. Normally, it assumed that for small deformations the solid phase velocity is negligibly small, as are the solid phase displacements, thereby allowing the equations to be solved without considering a moving boundary.

4. Radial solute transport in cartilage undergoing axial cyclic deformations

Consider the case of a homogenous cylindrical disc of cartilage undergoing axisymmetric loading by an impermeable, frictionless barrier (figure 1), i.e. an unconfined dynamic compression test. Under this geometry we may assume that the axial strain is independent of the radial coordinate, and that there is no gradient in pressure or solute concentration in the axial direction. Hence, the governing equations (12), (16) and (25) may be rewritten

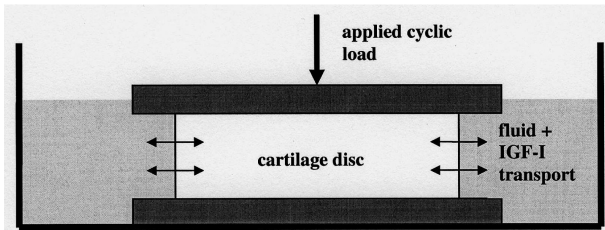


Figure 1. Diagram of cartilage dynamic loading experiment. A cylindrical cartilage plug undergoes axial sinusoidal deformation due to the movement of an impermeable, frictionless barrier. Surrounding the cartilage plug is a bath containing a solute (i.e. IGF-I), such that the cyclic transport of solute (and fluid) is in the radial direction only.

in cylindrical coordinates as

$$\frac{\partial v_r^s}{\partial r} + \frac{v_r^s}{r} + \frac{\partial \epsilon_z}{\partial t} - k \left[\frac{1}{r} \frac{\partial p}{\partial r} + \frac{\partial^2 p}{\partial r^2} \right] = 0 \quad (27)$$

$$-\frac{\partial p}{\partial r} + H_A \left[-\frac{u_r^s}{r^2} + \frac{1}{r} \frac{\partial u_r^s}{\partial r} + \frac{\partial^2 u_r^s}{\partial r^2} \right] = 0 \quad (28)$$

$$\frac{\partial c^w}{\partial t} - D \frac{\partial}{\partial r} \left(\frac{\partial c^w}{\partial r} \right) + \left[v_r^s - \frac{k}{\phi^f} \left(1 + \frac{D}{H_A k} \right) \frac{\partial p}{\partial r} - \frac{D}{r} \right] \times \frac{\partial c^w}{\partial r} = 0 \quad (29)$$

where $\epsilon_z = (\partial u_z^s / \partial z)$ is the applied time-dependent axial strain and

$$v_r^s = \frac{\partial u_r^s}{\partial t} \quad (30)$$

is the radial component of the solid phase velocity.

The applied strain is in the axial direction, and for simplicity (and to reflect a common experimental condition) is of sinusoidal form, i.e.

$$\epsilon_z = -\frac{\epsilon_0}{2} (1 - \cos(2\pi f t)) \quad (31)$$

With $u_r = u_r(r, t)$, $p = p(r, t)$ and $c^w = c^w(r, t)$ we can express the initial conditions as

$$u_r(r, 0) = 0 \quad \forall r \quad (32)$$

$$p(r, 0) = 0 \quad \forall r \quad (33)$$

$$c^w(r, 0) = 0 \quad \forall r \quad (34)$$

and the boundary conditions at the outer edge of the cartilage $r = r_0$ as the following:

$$p(r_0, t) = p_0 = 0 \quad (35)$$

$$c^w(r_0, t) = c_0 \quad (36)$$

$$\frac{\partial u_r}{\partial r}(r_0, t) = \frac{\nu}{1 - \nu} \left(\frac{u_r(r_0, t)}{r_0} + \epsilon_z \right) \quad (37)$$

where p_0 and c_0 are the pressure and solute concentration at the edge of the cartilage (i.e. *in vivo*, this is in the synovial joint), respectively. Equation (37) provides the requirement that at the boundary $r = r_0$ there should not be a jump in the traction. For symmetry, at the center of the cartilage we also have

$$u_r(0, t) = 0 \quad (38)$$

$$\frac{\partial u_r}{\partial r}(0, t) = 0 \quad (39)$$

and

$$\frac{\partial c^w}{\partial r}(0, t) = 0 \quad (40)$$

Table 3 lists the range of parameters used in this study. The cartilage parameters used are typical of bovine articular cartilage (Buschmann *et al.* 1999, Bonassar *et al.* 2000, Williamson *et al.* 2001), although we are aware that large variations can occur from these parameter set with cartilage age (Williamson *et al.* 2001), load (Gu *et al.* 2003, Zhang and Szeri 2005), health and even within a normal cartilage (Krishnan *et al.* 2003). The one exception is the choice for the Poisson's ratio ($\nu = 0$). This value was chosen so that results could be compared directly with the past model of Mauck *et al.* (2003). However, although not be presented here, a more realistic Poisson's ratio of 0.1 was also tested for the cases 0.001 and 0.1 Hz and was found to have little impact on the results or conclusions presented in this paper ($< 0.5\%$ difference in solute concentration when $c^w(r, t) > 10^{-4}c_0$). An applied strain of 2% ($\epsilon_0 = 0.02$) was chosen because it corresponds to the strains applied in the experiments of Bonassar *et al.* (2000), (2001). These experiments, as well as those of (Li *et al.* 2001), also use a loading frequency in the range 0.1–1 Hz. We have extended this frequency range to 0.001 Hz to examine the potential contribution to IGF-I transport of altering between standing and sitting over a 20 min cycle. Later, we examine the effect on the fluid flow profiles during a loading cycle of varying the loading frequency and strain and the cartilage matrix properties of aggregate elastic modulus and hydraulic permeability.

Finally, the commercial finite element method software FEMLAB 3.1 (FEMLAB 2003) was used to solve the governing equations on an Intel Pentium 4, 3 GHz CPU, 1 Gb RAM, running Windows XP. In particular, equations (27)–(30), along with boundary conditions (34)–(40), were implemented using FEMLAB's *PDE modes, general form, time-dependent analysis*. A one-dimensional domain corresponding to the radial coordinate was used. Due to sharp gradients in pressure and velocity profiles encountered at high frequency loading (≥ 0.1 Hz), 1000 mesh elements were used for all calculations. The default time-dependent solver (Direct(UMFPACK)) was used to solve the system of equations. To be confident of long timescale results (2–3 days), particularly while

Table 3. Range of parameters used throughout this study.

Parameter	Value
Loading frequency (f)	0.001–1 Hz
Applied strain (ϵ_0)	0.02
Radius of cartilage disc (r_0)	1 mm
Boundary IGF-I concentration (c_0)	40 nM
Hydraulic permeability (k)	$2 \times 10^{-15} \text{ m}^4/\text{Ns}$
Aggregate elastic modulus (H_A)	0.3 MPa
Diffusion coefficient (D)	$5 \times 10^{-12} \text{ m}^2/\text{s}$
Solvent phase volume fraction (ϕ^f)	0.8
Poisson's ratio (ν)	0

loading at high frequencies, tolerances were set very small (relative tolerance 10^{-9} , absolute tolerance 10^{-10}). These tolerances were maintained for the more forgiving calculations (frequencies < 0.1 Hz). In all cases it was confirmed that the results obtained were independent of these mesh and tolerance settings.

5. Predictions of IGF-I transport at short and long times scales

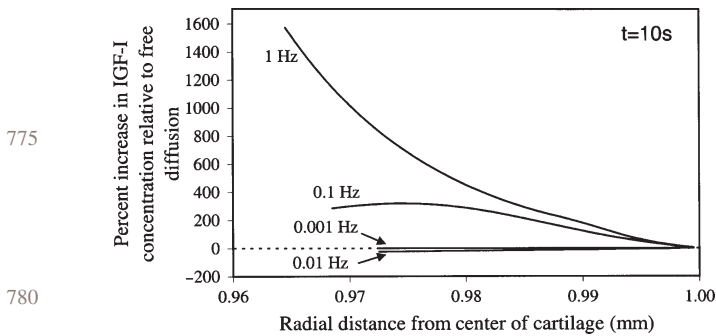
In this section, model predictions are presented for transport of IGF-I into a cyclically-loaded cartilage. First, transport on short time scales of up to 1 h are considered—specifically at time-points of 10, 100, 1000 and 3600 s after the onset of loading, for loading frequencies over the range of 0.001–1 Hz and applied axial strain of 2%. This length of time may be thought of as typical of a burst of physiologic activity such as walking to the shops, around the house, etc. Timescales of approximately 1 h are typically of the majority of experimental studies listed in table 1. Later, results are presented for a longer timescale, 2–3 days, which is sufficient time for average IGF-I concentrations to reach a steady state throughout the cartilage. This long time-span is typical of the majority of previous models. However, past models have also tended towards strains greater than 10%.

5.1 Short time scales

In figures 2–5 the percent increase in the IGF-I concentration (compared with free diffusion) due to dynamic loading is shown as a function of the radial distance from the center of the cartilage and the loading frequency. Each figure displays the increase in IGF-I concentration at one of four time intervals after the onset of loading: 10, 100 and 1000 and 3600 s (1 h). Note each figure only displays curves corresponding to the front of propagation of IGF-I into the cartilage sample. Specifically, curves are truncated at a radial distance corresponding to an IGF-I concentration $c^w = 5 \times 10^{-3}c_0$.

From figures 2–5 it is apparent that there is a significant difference between the IGF-I concentration in the loaded versus static cases. This difference is most pronounced for the highest loading frequency examined and at the shortest time intervals. Note, however that all concentrations tend toward the free diffusion case with increasing time, for the frequencies considered. This long term behavior of solute concentrations has not been reported previously. For the regions in the cartilage where the IGF-I has penetrated into the cartilage, we can see that cyclic strain leads to a 1500% increase in the IGF-I concentration, compared to free diffusion, for the 1 Hz loading after just 10 s of loading. However this enhanced transport soon becomes more modest, with an enhancement of just 4–8% predicted after 1 h of loading at 1 Hz.

Interestingly, we see that dynamic loading does not always enhance the IGF-I uptake. In some instances



775

780

785

Figure 2. The increase in the IGF-I concentration for the cyclically loaded case compared with free diffusion after 10 s, for a range of loading frequencies between 0.001–1 Hz. The dashed line provides a 0% reference. Note curves are truncated when the concentration falls below $5 \times 10^{-3}c_0$.

790

795

800

805

810

(see 0.01 Hz case in figure 2 and 0.001 Hz case in figures 3–5) we see that loading inhibits the transport of IGF-I. In some cases, this inhibition is comparable to the enhancement observed at other higher loading frequencies. For these cases, the cartilage has either not undergone a single complete loading cycle or is in the middle of a cycle, and the loading is such that the solvent is being pushed out of the cartilage, taking any IGF-I with it. For example, at 100 s, the 0.001 Hz cycle is only 1/10th of the way through a cycle and is still undergoing a compression stage, pushing fluid out of the cartilage. Recall from the introductory discussion in Section 2 reported that static compression inhibits cartilage protein production (Grodzinsky *et al.* 2000), although this inhibition is a transient phenomena in the presence of IGF-I. Depending on the timescale of these experiments, perhaps fluid (and therefore IGF-I) is being squeezed out of the cartilage during the experiment. Of some relevance here is the experimental findings of Quinn *et al.* (2002) showing solute concentration profiles after 60 min of loading at 0.001 Hz, which corresponds to 3.6 cycles. That is, results are presented for a timepoint within a completed cycle, which may need to be taken into account when interpreting the observed transport behavior.

815

820

825

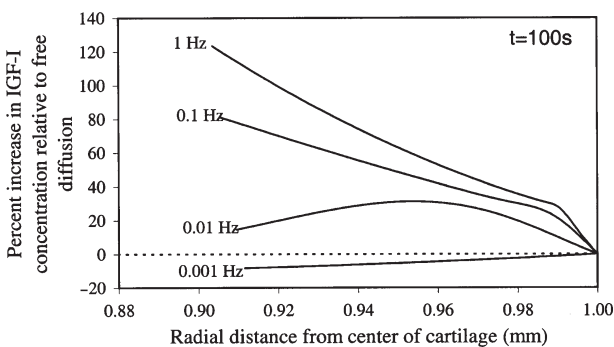
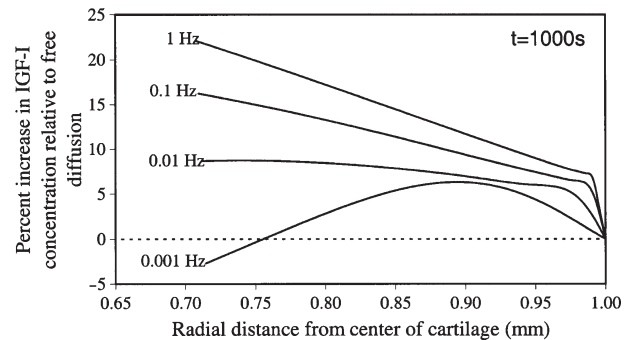


Figure 3. The increase in the IGF-I concentration for the cyclically loaded case compared with free diffusion after 100 s, for a range of loading frequencies between 0.001–1 Hz. Note the reduction in the influence of advection on solute transport compared to figure 2.



830

835

840

5.2 Long time scales

Figure 6 shows the evolution of the IGF-I concentration profile for a cartilage loaded sinusoidally (2% applied strain at 0.1 Hz). It is seen that after approximately 60 h, the IGF-I profile reaches a uniform concentration equal to the concentration imposed on the outside boundary. Consistent with the trends observed in the previous section, the predicted behavior is similar to that expected by free diffusion ($f = 0$). In fact, the predicted behavior for all loading frequencies considered (0.001–0.1 Hz) were almost identical to free diffusion (after 5 h the difference was less than 1% (figure 7)). In other words, it is found here that dynamic loading had essentially no effect on the IGF-I concentration on these longer timescales, compared with free diffusion. Note the higher loading frequency of 1 Hz was not included due to long computation times combined with uncertainty in the size of the cumulative numerical error associated with approximately 3×10^5 loading cycles. However from figures 2–5, we can expect that the 1 Hz case would follow the same trend.

As noted above, the final steady state concentration approaches a uniform profile equal to the imposed constant boundary concentration, consistent with the experiments of Bonassar *et al.* (2001). Mauck *et al.* (2003), also found this

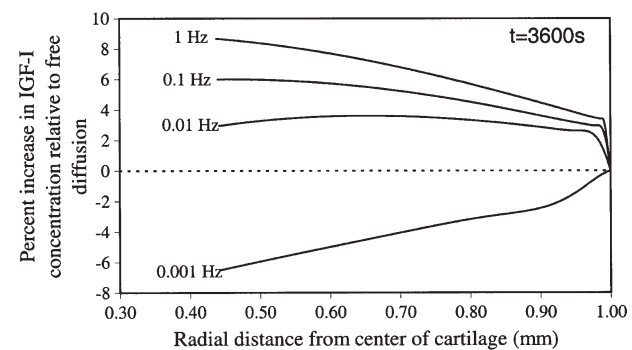


Figure 5. The increase in the IGF-I concentration for the cyclically loaded case compared with free diffusion after 1 h, for a range of loading frequencies between 0.001–1 Hz. Note the relatively strong inhibition of transport for the 0.001 Hz case. At 0.001 Hz s, 3600 s corresponds to 3.6 loading cycles, i.e. an incomplete cycle.

880

885

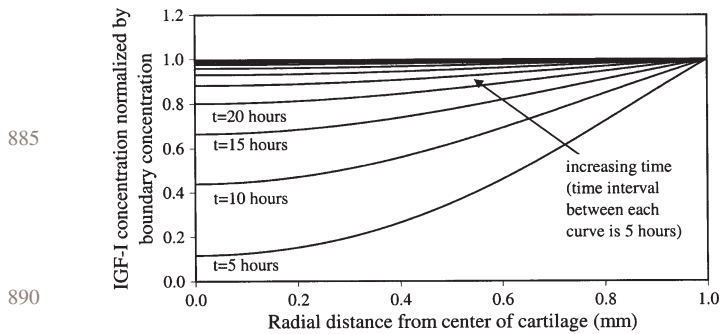


Figure 6. Transport of IGF-I into a cartilage undergoing cyclic deformation of 2% at 0.1 Hz. The vertical axis has been normalized by the boundary concentration c_0 . Time between each curve is 5 h. Although not shown, loading of 0.001 and 0.01 Hz and free diffusion ($f = 0$) produced nearly identical results to those shown here. That is, dynamic loading had only a minor effect on IGF-I transport on these time scales.

behavior for similar range of parameters. However, when Mauck *et al.* increased the applied strain (up to 20%) they found the surprising result that the steady state concentration can be multiple times that of the boundary concentration. Note these large strains are above the experimental range used by Bonassar *et al.* (2000, 2001), Grodzinsky *et al.* (2000) and Li *et al.* (2001) and it could be argued that they also exceed the small strain approximation assumed in their model. The enhanced concentration effect was predicted by Mauck *et al.* (2003) to increase with an increasing value of $(H_A k/D)$. However, the highest value of $(H_A k/D)$ considered by Mauck *et al.* (2003) was 100, which is similar to our value of 108. We therefore question the finding in Mauck *et al.* (2003) and suggest that it is incorrect.

The unexpected result found in Mauck *et al.* (2003) were obtained when the Peclet number (describing the ratio of advective transport to diffusive transport) was high—a situation which is notoriously difficult to solve numerically (for discussion see Chapter 2 of Zienkiewicz and Taylor (2000)). Peclet number is defined using the ratio of a characteristic velocity and length to the diffusion coefficient. In our model the Peclet number does not exceed a value of 1. Based simply on a ten-fold increase in

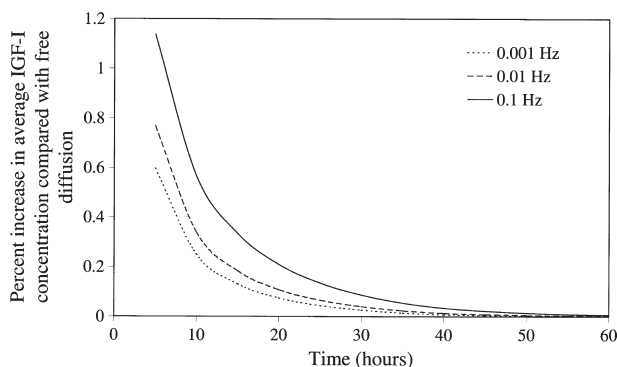


Figure 7. The percent increase in the radially averaged IGF-I concentration for 2% applied deformation at loading frequencies of 0.001–0.1 Hz. After 5 h, for all frequencies examined, cyclic loading had minimal effect ($< 1\%$) on IGF-I transport.

the applied strain, we would expect that the Peclet number in the model of Mauck *et al.* (2003) is of the order of 10. It is our opinion that the unusual predictions found in Mauck *et al.* (2003) are the consequence of the difficulty the FEM technique has in approximating the true solution when advective transport dominates over diffusion. In fact when trying to reproduce the results of Mauck *et al.* (2003) we encountered numerical problems within the region of high fluid velocity gradients near the edge of the cartilage. In any case, a physical mechanism to support the surprising prediction is currently lacking.

6. Darcy velocity—fluid flow profiles

The results found in figures 2–7 can be better understood by examining the spatial variation in the velocity of the solvent phase relative to the solid phase—the Darcy velocity (equation (11)). In the case of free diffusion the Darcy velocity is zero. Hence one should expect the largest modification in IGF-I transport to occur in regions in which the Darcy velocity is the greatest.

A typical variation in the Darcy velocity profile during a deformation cycle is shown in figure 8. From figure 8 it is seen that although the 1 Hz loading regime results in the greatest Darcy velocity, the fluid shear is localized to

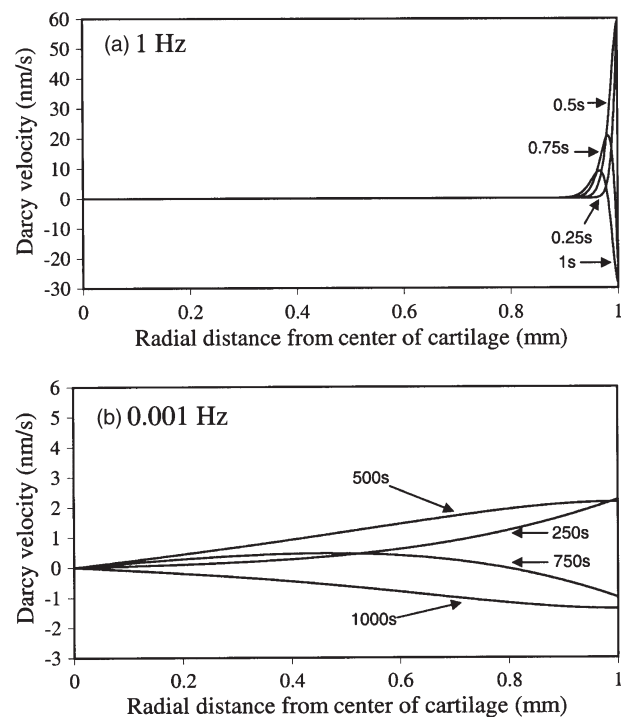


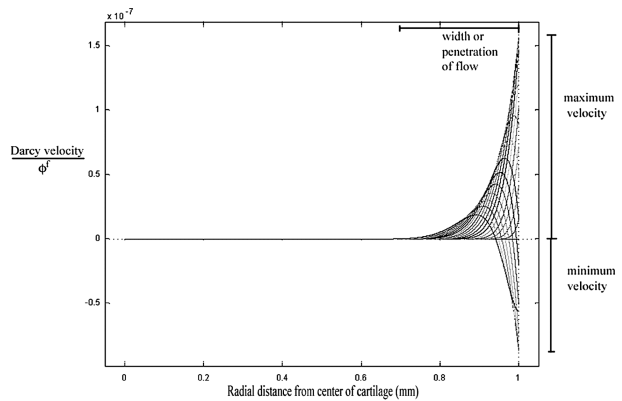
Figure 8. The Darcy velocity at four stages within the first loading cycle for (a) 1 Hz, and (b) 0.001 Hz. Note the vertical axis scale change before comparing the two figures, i.e. the magnitude of the Darcy velocity is strongly dependent on loading frequency. Although the 1 Hz loading results in a larger Darcy velocity than the 0.001 Hz loading, it is highly localized to the edge of the cartilage and its effect on IGF-I transport is limited. On the other hand, the Darcy velocity is not localized in the case of 0.001 Hz, however, its size is relative small, also limiting its contribution to IGF-I transport.

the outside edge of the cartilage disc ($r \sim r_0$). With this combination of low permeability and high frequency there is insufficient time for substantial fluid movement within a loading cycle, deep inside the cartilage. The consequence of this localized velocity is that any enhancement of IGF-I transport due to the Darcy velocity will only occur near the external edge of the cartilage. The majority of the cartilage still undergoes free diffusion with little contribution from the fluid velocity on transport. For the lower frequencies on the other hand, the Darcy velocity is not localized, extending to the center of the cartilage. However, the magnitude of the velocity is less than 10% of that found in the 1 Hz case. Hence, one might expect transport by advection for the lower loading frequency might be commensurately smaller.

That is, dynamic loading at frequencies relevant to a walking pace (approximately, 1 Hz) only induces fluid motion at the very edge of the cartilage, and the cartilage mostly behaves as a constant volume material. Whereas compression at 0.001 Hz (e.g. standing for 20 min), allows the cartilage to act as a compressible (drained) material, with fluid being expelled. Presumably any enhanced solute transport would also follow (more or less) the same spatial range as the fluid shear.

Although figures 2–7 do show the enhanced transport expected from considering the Darcy velocity, i.e. greatest enhancement occurs for highest frequency and close to the cartilage edge (shorter timescales), there are some unexpected predictions. For example, figure 8 shows that the fluid shear (Darcy velocity) in the 1 Hz case is only significant in region 1/10th of a millimeter from the cartilage disc's outer (free) edge. Yet figure 4 clearly shows that cyclic loading still results in enhanced transport for much deeper layers, e.g. 25% enhancement at 3/10ths of a millimeter from the cartilage edge. Of course this anomaly does not exist at greater timescales (or further into the cartilage). An explanation for this result is that enhanced transport of solute into one layer of cartilage, through advection, will also lead to enhanced transport into adjacent layers, through diffusion, as these deeper layer experience an earlier exposure to the transported solute than otherwise would be the case.

Cartilage material parameters, such as its stiffness and permeability, and the range of applied strains and loading frequencies employed, typically vary between experiments and models. It is therefore instructive to examine the effect of cyclic deformation and cartilage properties on the Darcy velocity. Here we define the width of the Darcy velocity as the radial distance from the outside edge into the cartilage for which the Darcy velocity is $\geq 10^{-4} \mu\text{m/s}$ during a complete deformation cycle (figure 9). To gauge the magnitude of the Darcy velocity we record the maximum and minimum Darcy velocity during a complete loading cycle (refer again to figure 9). Note the Darcy velocity changes direction (sign) during a loading cycle and so the maximum and minimum Darcy velocity measure the maximum magnitude of velocity in each flow direction.



Q5 Figure 9. Definition of Darcy velocity characteristics (i.e. maximum and minimum velocity and width) used in figures 10–13. Shown is v_d / ϕ^f as a function of radial distance from the center of the cartilage for a number of timepoints throughout a single loading cycle.

Figure 10 shows that the maximum and minimum Darcy velocity appears to be proportional to the applied strain, however, there is little effect of strain on the penetration (width) of the Darcy flow within the cartilage. Only at small strains is a slight reduction of penetration found. Hence it can be expected that increasing the dynamic strain amplitude may lead to greater enhanced transport from fluid flow. In fact, by comparison with figures 11–13, applied strain amplitude is the dominant determinant of the maximum and minimum Darcy velocity.

It can be seen from figure 11 that the maximum and minimum Darcy velocity increases with the loading frequency in a non-linear fashion, however, the degree of penetration drops rapidly with increasing strain frequency.

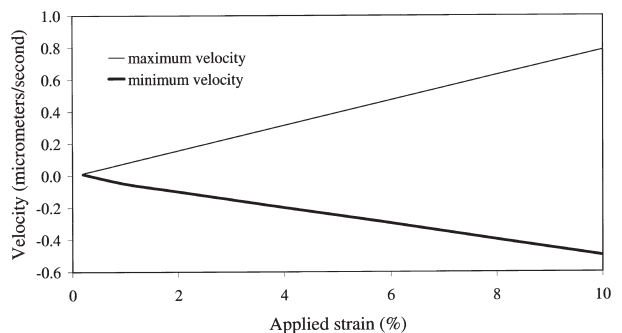
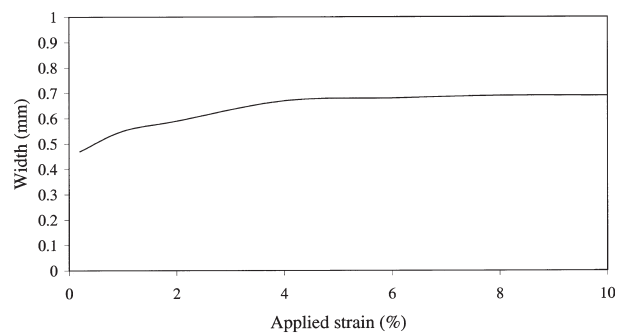


Figure 10. The Darcy velocity characteristics as a function of applied strain. All other variables are held constant at the value given in table 2.

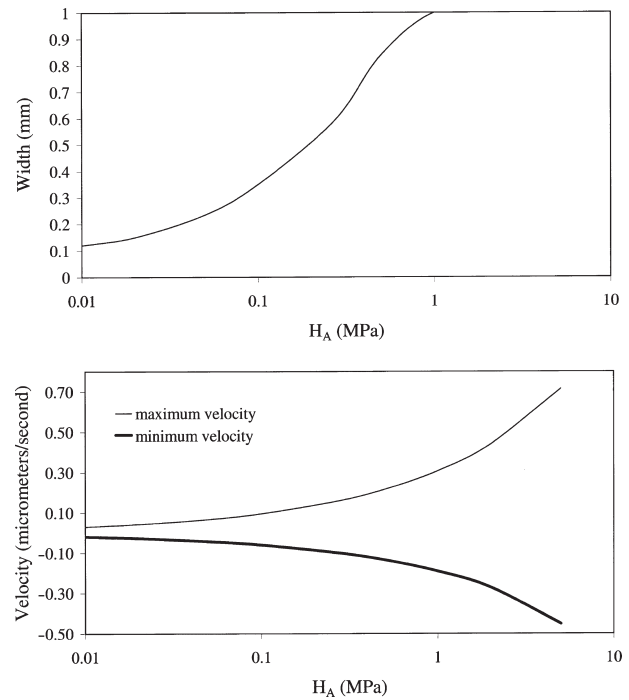
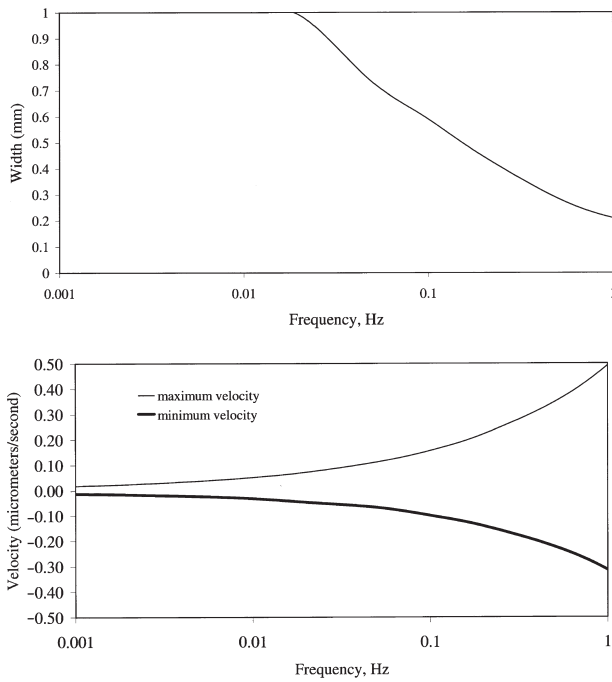


Figure 11. The Darcy velocity characteristics as a function of the loading frequency. All other variables are held constant at the value given in table 2.

Figure 13. The Darcy velocity characteristics as a function of matrix elasticity H_A . All other variables are held constant at the value given in table 2.

A physical interpretation of this result is that insufficient time is available for substantial fluid to flow within a cycle at high frequencies, and the fluid remains trapped within the matrix and absorbs the load. This implies that the benefits gained towards increasing the magnitude of Darcy

velocity through increasing the loading frequency is offset by the reduction in penetration. As a rule, high frequencies lead to greater enhancement of solute transport, but only near a narrow edge of the cartilage.

As can be seen in figures 12 and 13 increasing the hydraulic permeability and the matrix stiffness both leads to an increase in the magnitude of the Darcy velocity and the penetration.

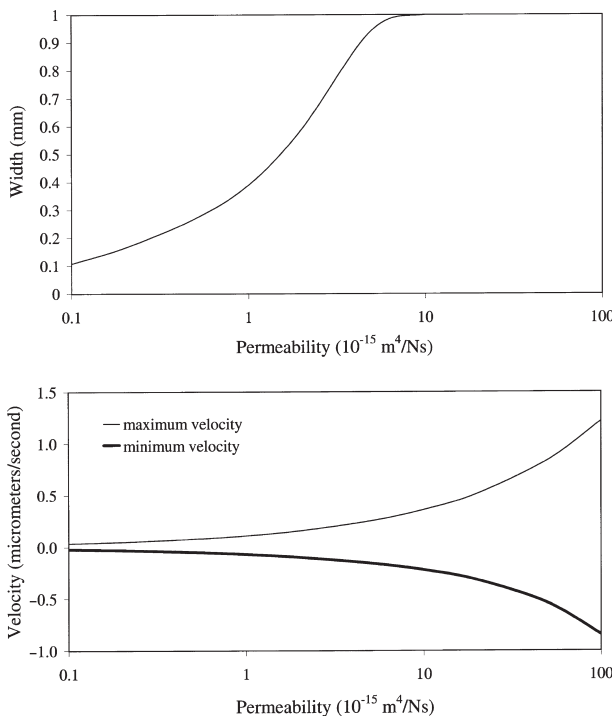


Figure 12. The Darcy velocity characteristics as a function of the hydraulic permeability. All other variables are held constant at the value given in table 2.

7. Discussion

It is important to note that cyclic, symmetric loading alone is insufficient to enhance advective transport over more than one cycle. There needs to be a “symmetry breaking mechanism”. For example, if the timescale for diffusion is large in comparison to the loading period (so advection dominates), the effect of loading is to draw solute into the cartilage and to push it all out again during a complete cycle—with no net increase in solute transport. Diffusion provides a symmetry breaking mechanism. Within a cycle, solute is drawn into the cartilage by advection, diffuses a little further down the concentration gradient, and does not make it back out to the external boundary at the end of the cycle. This results in a net increase in solute transport at the end of a completed cycle. This symmetry breaking through diffusion is greatest near the edge of the cartilage but only at the shortest timescales, as it is only then and there that the concentration gradient is the steepest (and changes most rapidly) (figure 6). At longer timescales, the concentration gradient is small, and changes slowly, hence negligible symmetry breaking in

solute movement can occur, such that IGF-I transport in cyclically-loaded cartilage is similar to the case of free diffusion.

Note, additional symmetry breaking mechanisms may occur and could take the form of a strain dependent material properties (e.g. hydraulic permeability), a concentration dependent source or sink term (e.g. due to capture or release of IGF-I by IGF binding proteins (Bhakta *et al.* 2000)), more complicated cartilage geometry or time-dependent variations in the IGF-I concentrations at the cartilage boundaries and anisotropic material properties. For example, Quinn *et al.* (2001) have presented a model which predicted that the hydraulic permeability decreases more rapidly in a direction perpendicular to the direction of compression (compared to parallel to the direction of compression). This may serve two purposes in a cartilage. First, it would encourage fluid flow to the lubricating surfaces and secondly, it may provide an asymmetric fluid phase flow field leading to enhanced solute transport. These additional symmetry breaking mechanisms are currently the subject of ongoing work and will be reported in subsequent communications.

It is important to emphasize that a number of factors can strongly influence the interpretation of predictions and observations. Obviously, predictions of the degree of enhancement (or inhibition) will be affected if another range of model parameters are chosen, such as occurred in Ferguson *et al.* (2004). For example, larger deformations would increase the fluid movement and increase the fluid penetration distance within the cartilage, thereby increasing the importance of dynamic loading to larger depths and long timescales. Perhaps by considering cartilage plugs with a smaller (larger) diameter reported enhanced transport would be greater (less)? This remains to be elucidated.

Other more subtle influences on interpreting experimental and model results can occur. Mentioned previously (in Section (6.1)) was the confounding effect of observing the transport only midway through a loading cycle, such that one begins to consider transient enhancement/inhibition rather than a “time-averaged” enhancement (figures 2–5).

One often-cited experimental observation supporting load-induced enhanced solute transport, that is at odds with the prediction presented here, is that of Bonassar *et al.* (2001). Using the same applied strain magnitude and loading frequency used in the current study (i.e. 2% at 0.1 Hz) Bonassar *et al.* found significant enhancement of IGF-I transport over timescales of tens of hours, certainly not the <1% enhancement presented in figure 7. A common assumption made in both experiments and models is that the diffusion is much faster in the solvent bath surrounding the cartilage than inside the cartilage, such that the concentration of solute at the cartilage surface can be considered constant. This is sometimes referred to as the “well-mixed bath” assumption. However, in the case of IGF-I, its diffusion coefficient in the bath is comparable to the diffusion coefficient in the

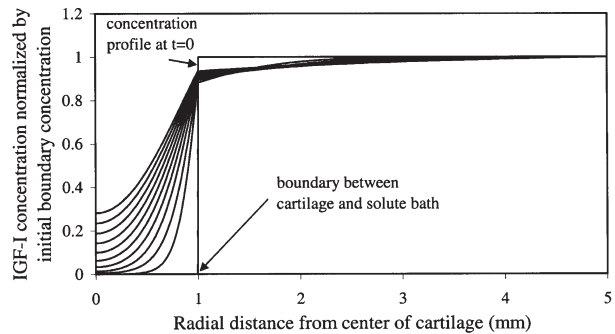


Figure 14. When the diffusion coefficient of a solute is of similar size in both the cartilage and the surrounding solute bath, a concentration gradient can develop near the cartilage-bath boundary. This gradient leads to a reduction in the boundary solute concentration and subsequent reduction in solute transport into the cartilage, compared to a well mixed bath. Here the parameters listed in table 3 have been used, with the additional assumption that the diffusion coefficient in the bath is $3 \times 10^{-11} \text{ m}^2/\text{s}$ as given in Mauck *et al.* (2003) based on arguments provided in Schneiderman *et al.* (1995). Note each curve represents the concentration profile at 1 h intervals.

cartilage, and significant concentration gradients may also develop in the bath (unless steps are taken to ensure the bath is well-mixed). Slower diffusion within the bath effectively results in the concentration at the cartilage boundary changing with time and is generally lower than expected from the well-mixed assumption (figure 14). Cyclic loading may serve to mix the bath, increasing the boundary concentration of IGF-I in comparison to a stagnant bath in a static (free diffusion) experiment. In figures 15 and 16 the transport for a well mixed bath versus a static bath is compared, for two assumed IGF-I-in-solution diffusion coefficients based on either (Mauck *et al.* 2003) (stagnant bath 1) or the Stokes–Einstein relation between the diffusion coefficient, molecular mass and fluid viscosity (stagnant bath 2). The predicted enhanced transport for a well-mixed bath (assumed to correspond to a cyclically loaded cartilage) and a stagnant bath (corresponding to free diffusion) is of the same order

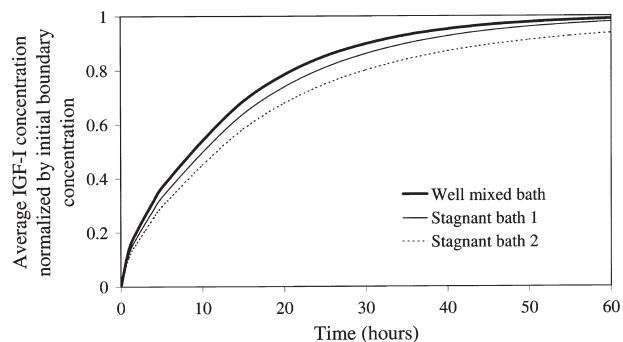


Figure 15. Effect of bath mixing on the transport of IGF-I into an unloaded cartilage. Shown is a well mixed bath, and two stagnant baths in which the IGF-I diffusion coefficient is assumed to be either $3 \times 10^{-11} \text{ m}^2/\text{s}$ (stagnant bath 1) or $11 \times 10^{-11} \text{ m}^2/\text{s}$ (stagnant bath 2). These two diffusion coefficients reflect the number provided in Mauck *et al.* (2003) (figure 14) and an estimate from the Stokes–Einstein law assuming a globular (spherical) molecule of density 1.4 times that of water, respectively. All other model parameters are as for figure 14 and table 2.

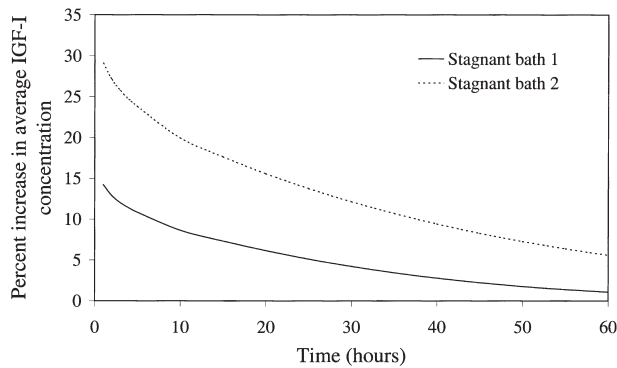


Figure 16. Effect of bath mixing on the transport of IGF-I into an unloaded cartilage. Neglecting the effect of solute diffusion in the bath leads to quite a significant modification of the transport of solute into the cartilage. The percent enhancement of transport by mixing is of similar order, and over similar timescales, as that found in Bonassar *et al.* (2001), suggesting an alternate interpretation of that often cited finding supporting the enhance transport of solutes through cyclic loading. Model parameters are as for figure 15.

and over similar timescales as the experimental observations of Bonassar *et al.* (2001) and suggest an alternate explanation of this observation.

Based on the discussion here, we believe mixing of synovial fluid within an articular joint, through joint movement, should aid the transport of IGF-I over longer timescales and to greater depths than fluid flow within the cartilage due to applied cyclic loading. That is, greater benefits to nutrient transport may be achieved through load free joint motion than cyclic loading of a joint. Depending on the significance of a 10–20% increase in IGF-I concentration on aggrecan synthesis compared with fluid shear, this may be of some consideration for joint rehabilitation.

8. Conclusion

As mention in the introduction, Buschmann *et al.* (1999) observed that the stimulation of aggrecan synthesis by chondrocytes was greatest in regions within the cartilage which experienced the highest fluid shear. That is, with increasing frequency, synthesis occurred closer to the external boundary. Only chondrocytes near the outside edge of the cartilage disc would be able to detect fluid motion for high frequency loading (figure 8). Figures 2–5 show that dynamic loading can enhance solute transport near the outside edge of the cartilage disc, but has limited effect at inner layers. It is then feasible that chondrocytes respond to the combined effect of fluid shear and enhanced nutrient transport within layers close to the edge of the cartilage disc.

Ongoing work is concentrated on the effect of symmetry breaking conditions, as discussed previously. Specifically, we are currently investigating the effect of the kinetics of solute binding to the solid phase, anisotropic material properties such as the hydraulic

permeability, and time dependent boundary concentrations of IGF-I.

Acknowledgements

The authors wish to thank the Australian Research Council for their financial support for this project, Grant:DP50192.

References

- J. Bear and Y. Bachmat, *Introduction to Modeling of Transport Phenomena in Porous Media*, Dordrecht, The Netherlands: Kluwer Academic Publishers, 1991.
- N.R. Bhakta, A.M. Garcia, E.H. Frank, A.J. Grodzinsky and T.I. Morales, “The insulin-like growth factors (igfs) i and ii bind to articular cartilage via the igf-binding proteins”, *J. Biol. Chem.*, 275(8), pp. 5860–5866, 2000.
- M.A. Biot, “General theory of three dimensional consolidation”, *J. Appl. Phys.*, 12, pp. 155–164, 1941.
- L.J. Bonassar, A.J. Grodzinsky, A. Srinivasan, S.G. Davila and S.B. Trippel, “Mechanical and physiochemical regulation of the action of insulin-like growth factor-i on articular cartilage”, *Arch. Biochem. Biophys.*, 379(1), pp. 57–63, 2000.
- L.J. Bonassar, A.J. Grodzinsky, E.H. Frank, S.G. Davila, N.R. Bhaktav and S.B. Trippel, “The effect of dynamic compression on the response of articular cartilage to the insulin-like growth factor-i”, *J. Orthop. Res.*, 19, pp. 11–17, 2001.
- M.D. Buschmann, Y.J. Kim, M. Wong, E.H. Frank, E.B. Hunziker and A.J. Grodzinsky, “Stimulation of aggrecan synthesis in cartilage explants by cyclic loading is localized to regions of high interstitial fluid flow”, *Arch. Biochem. Biophys.*, 366(1), pp. 1–7, 1999.
- E. De Angelis and L. Preziosi, “Advection–diffusion models of solid tumour evolution *in vivo* and related free boundary problem”, *Math. Models Methods Appl. Sci.*, 10, pp. 379–407, 2000.
- FEMLAB—*Multiphysics in MATLAB*, MA, USA: COMSOL, Inc., 2003.
- S.J. Ferguson, K. Ito and L.-P. Nolte, “Fluid flow and convective transport of solutes within the intervertebral disc”, *J. Biomech.*, 37, pp. 213–221, 2004.
- A.J. Grodzinsky, M.E. Levenston, M. Jin and E.H. Frank, “Cartilage tissue remodeling in response to mechanical forces”, *Annu. Rev. Biomed. Eng.*, 2, pp. 691–713, 2000.
- W.Y. Gu, W.M. Lai and V.C. Mow, “A mixture theory for charged-hydrated soft tissues containing multi-electrolytes: passive transport and swelling behaviors”, *J. Biomech. Eng.*, 120, pp. 169–180, 1998.
- W.Y. Gu, H. Yao, C.Y. Huang and H.S. Cheung, “New insight into deformation-dependent hydraulic permeability of gels and cartilage, and dynamic behaviour of agarose gels in confined compression”, *J. Biomech.*, 36, pp. 593–598, 2003.
- Y.J. Kim, R.L.Y. Sah, A.J. Grodzinsky, A.H.K. Plaas and J.D. Sandy, “Mechanical regulation of cartilage biosynthetic behavior: physical stimuli”, *Arch. Biochem. Biophys.*, 311(1), pp. 1–12, 1994.
- S.M. Klisch, S.S. Cheng, R.L. Sah and A. Hoger, “A growth mixture theory for cartilage with application to growth-related experiments on cartilage explants”, *J. Biomech. Eng.*, 125, pp. 169–179, 2003.
- S.M. Klisch, R.L. Sah and A. Hoger, “A cartilage growth mixture model for infinitesimal strains: solutions of boundary-value problems related to *in vitro* growth experiments”, *Biomech. Model. Mechanobiol.*, 3, pp. 209–223, 2005.
- R. Krishnan, S. Park, F. Eckstein and G.A. Ateshian, “Inhomogeneous cartilage properties enhance superficial interstitial fluid support and frictional properties, but do not provide a homogeneous state of stress”, *J. Biomech. Eng.*, 125, pp. 569–577, 2003.
- W.M. Lai, J.S. Hou and V.C. Mow, “A triphasic theory for the swelling and deformation behaviors of articular cartilage”, *J. Biomech. Eng.*, 113, pp. 245–258, 1991.
- G. Lemon, J.R. King, H.M. Byrne, O.E. Jensen and K.M. Shakesheff, “Mathematical modelling of engineered tissue growth using a multiphase porous flow mixture theory”, *J. Math. Biol.*, 52, pp. 571–594, 2006.

- K.W. Li, Y.H. Falcovitz, J.P. Nagraj, A.C. Chen, L.M. Lottman, J.Y.-J. Shyy and R.L. Sah, "Mechanical compression of transplanted chondrocytes", *J. Orthop. Res.*, 18, pp. 374–382, 2000.
- 1435 K.W. Li, A.K. Williamson, A.S. Wang and R.L. Sah, "Modulators of cartilage biology: growth response of cartilage to static and dynamics compression", *Clin. Orthop. Relat. Res.*, 391S, pp. S34–S48, 2001.
- L.P. Li, M.D. Buschmann and A. Shirazi-Adl, "The asymmetry in transient response in compression versus release for cartilage in unconfined compression", *J. Biomech. Eng.*, 123, pp. 519–522, 2001.
- 1440 R.L. Mauck, C.T. Hung and G.A. Ateshian, "Modeling of neutral solute transport in a dynamically loaded porous permeable gel: implications for articular cartilage biosynthesis and tissue engineering", *J. Biomech. Eng.*, 125, pp. 602–614, 2003.
- V.C. Mow, S.C. Kuei, W.M. Lai and C.G. Armstrong, "Biphasic creep and stress relaxation of articular cartilage in compression: theory and experiments", *J. Biomech. Eng.*, 102, pp. 73–84, 1980.
- B.P. O'Hara, J.P. Urban and A. Maroudas, "Influence of cyclic loading on the nutrition of articular cartilage", *Ann. Rheum. Dis.*, 49, pp. 536–539, 1990.
- 1445 K.D. Osborn, S.B. Trippel and H.J. Mankin, "Growth factor stimulation of adult articular cartilage", *J. Orthop. Res.*, 7(1), pp. 35–42, 1989.
- G.P. Peters and D.W. Smith, "Solute transport through a deforming porous medium", *Int. J. Numer. Anal. Methods Geomech.*, 26, pp. 683–717, 2002.
- 1450 T.M. Quinn, A.J. Grodzinsky, M.D. Buschmann, Y.-J. Kim and E.B. Hunziker, "Mechanical compression alters proteoglycan deposition and matrix deformation around individual cells in cartilage explants", *J. Cell Sci.*, 111, pp. 573–583, 1998.
- T.M. Quinn, P. Dierickx and A.J. Grodzinsky, "Glycosaminoglycan network geometry may contribute to anisotropic hydraulic permeability in cartilage under compression", *J. Biomech.*, 34, pp. 1483–1490, 2001.
- 1455 T.M. Quinn, C. Studer, A.J. Grodzinsky and J.J. Meister, "Preservation and analysis of nonequilibrium solute concentration distributions within mechanically compressed cartilage explants", *J. Biochem. Biophys. Methods*, 52, pp. 83–95, 2002.
- V.R. Sara and K. Hall, "Insulin-like growth factors and their binding proteins", *Physiol. Rev.*, 70(3), pp. 591–614, 1990.
- R. Schneiderman, E. Snir, O. Popper, J. Hiss, H. Stein and A. Maroudas, "Insulin-like growth factor-i and its complexes in normal human articular cartilage: studies of partition and diffusion", *Arch. Biochem. Biophys.*, 324(1), pp. 159–172, 1995.
- A.C. Shieh and K.A. Athanasiou, "Principles of cell mechanics for cartilage tissue engineering", *Ann. Biomed. Eng.*, 31, pp. 1–11, 2003.
- F.H. Silver and G. Bradica, "Mechanobiology of cartilage: how do internal and external stresses affect mechanochemical transduction and elastic energy storage?", *Biomech. Model. Mechanobiol.*, 1, pp. 219–238, 2002.
- 1495 D.W. Smith, "One-dimensional contaminant transport through a deforming porous medium: theory and a solution for a quasi-steady state problem", *Int. J. Numer. Anal. Methods Geomech.*, 24, pp. 693–722, 2000.
- K. Terzaghi, *Theoretical Soil Mechanics*, New York, USA: Wiley, 1943.
- 1500 A. Verruijt, *Computational Geomechanics*, Dordrecht, The Netherlands: Kluwer Academic Publishers, 1995.
- A.K. Williamson, A.C. Chen and R.L. Sah, "Compressive properties and function-composition relationships of developing bovine articular cartilage", *J. Orthop. Res.*, 19(6), pp. 1113–1121, 2001.
- L. Zhang and A.Z. Szeri, "Transport of neutral solute in articular cartilage: effects of loading and particle size", *Proc. R. Soc. A*, 461, pp. 2021–2042, 2005.
- 1505 O.C. Zienkiewicz and R.L. Taylor, "The finite element method", *Fluid Dynamics*, 5th ed., Oxford, United Kingdom: Butterworth-Heinemann, 2000, vol. 3.
- W.B. van den Berg, P.M. van der Kraan, A. Scharstuhl and H.M. van Beuningen, "Tissue engineering, cells, scaffolds, and growth factors: growth factors and cartilage repair", *Clin. Orthop. Relat. Res.*, 391S, pp. S244–S250, 2001.
- 1510
- 1460
- 1515
- 1465
- 1520
- 1470
- 1525
- 1475
- 1530
- 1480
- 1535
- 1485
- 1540

L. Zhang, B. Gardiner, D. Smith, **P. Pivonka**, A. Grodzinsky. The effect of cyclic deformation and solute binding on solute transport in cartilage. *Archives of Biochemistry and Biophysics*, **457** (1), pp 47-56, 2007.

The effect of cyclic deformation and solute binding on solute transport in cartilage

Lihai Zhang^{a,*}, Bruce S. Gardiner^a, David W. Smith^a, Peter Pivonka^a, Alan Grodzinsky^b

^a Department of Civil and Environmental Engineering, The University of Melbourne, Vic. 3010, Australia

^b Center for Biomedical Engineering, Department of Electrical Engineering and Computer Science, Department of Mechanical Engineering, Massachusetts Institute of Technology, Cambridge, MA, USA

Received 6 October 2006
Available online 30 October 2006

Abstract

Diffusive transport must play an important role in transporting nutrients into cartilage due to its avascular nature. Recent theoretical studies generally support the idea that cyclic loading enhances large molecule transport through advection. However, to date, reactive transport, i.e. the effects of solute binding, has not yet been taken into consideration in cyclically deformed cartilage. In the present study, we develop a reactive transport model to describe the potential role of binding of solute within cyclically deformed cartilage. Our results show that binding does have a significant effect on transport, particularly for the low IGF-I concentrations typical of synovial fluid. A dynamic loading regime of high strain magnitudes (up to 10%) in combination with high frequencies (e.g. 1 Hz) was seen to produce the most dramatic results with enhanced total uptake ratio as high as 25% averaged over the first 5 h of cyclic loading.

© 2006 Elsevier Inc. All rights reserved.

Keywords: IGF-I; Binding proteins; Transport; Cartilage; Dynamic loading

The ability of cartilage to withstand physiological mechanical loading depends on the structural integrity of its extra-cellular matrix (ECM), which in turn requires chondrocyte-mediated synthesis of collagens, glycoproteins, and other matrix molecules [1]. Both nutrients (e.g. growth factors) and mechanical loading are known inducers of matrix synthesis in cartilage explants in culture, and so are presumably required to maintain functional cartilage [2]. Among the various growth factors, the insulin-like growth factors (IGFs)¹ appear to be among the more important molecules for cartilage maintenance [3]. Several experiments [4–6] have found that the concentration levels of IGF (in all its forms) are very low in normal human cartilage—but are high in osteoarthritic cartilage. IGF-I not

only interacts with chondrocytes by binding to cell surface receptors, resulting in increased production of cartilage matrix, but also appears to have an anti-catabolic effect on cartilage, inhibiting or counteracting catabolic agents or processes which normally result in tissue degradation [2,7]. Due to the avascular nature of articular cartilage, growth factors in synovial fluid are transported by diffusion to the chondrocytes, but under cyclic loading of the cartilage, growth factors are transported by advection too.

Recently, increasing attention has focused on the ability of cells and tissues to respond to their mechanical environment. Experiments have shown that compression of cartilage causes deformation of cells and matrix, hydrostatic pressure gradients, interstitial fluid flow, and physicochemical changes including altered matrix water content, and osmotic pressure [8]. Numerous experiments [9–11] report that static loads (or strains) decrease matrix synthesis and cell proliferation. In contrast, a synergistic relationship between the presence of IGF-I and dynamic compression on cartilage matrix protein synthesis was reported by

* Corresponding author.

E-mail address: l.zhang@civenv.unimelb.edu.au (L. Zhang).

¹ Abbreviations used: IGFs, insulin-like growth factors; IGFs, IGF binding proteins; REV, representative element volume; SPR, surface plasmon resonance.

Grodzinsky et al. [1]. Kim et al. also reported an increase in biosynthesis as a result of dynamic compression of calf cartilage explants [9]. Furthermore, Buschmann et al. reported greater stimulation at the periphery compared to the centre in chondrocyte disks, and associated this enhanced protein synthesis spatial profile with the fluid shear profiles developed by the applied cyclic loading [11]. A few studies have shown that cyclic loading can enhance the transport of solutes, compared with free diffusion [12,13] and could potentially explain some of the increase in matrix synthesis in cartilage undergoing this loading regime [1]. The current paper belongs to a group of recent quantitative studies designed to test this postulate.

In recent years, porous media theory has been used to describe the mechanical behavior of hydrated soft tissues [12–14]. Mauck et al. [12] presented an advanced theoretical model based on the theory of incompressible mixtures to examine the effect of dynamic loading on nutrient transport in various porous media—including articular cartilage. The tissue was modeled as a mixture of three phases: a solid phase representing the ECM; a fluid phase representing the interstitial solvent and a neutral solute phase. The specific problem examined was solute transport through the lateral surface of a cylindrical tissue, held between frictionless impermeable platens, while the tissue underwent axial unconfined dynamic loading. Dynamic strains up to 20% at 0.01–1 Hz were considered. Their results suggested that dynamic loading can concentrate solute inside a cartilage.

Zhang and Szeri [13] also developed a porous media transport model for solute transport in cartilage. A distinct feature of their model is the inclusion of strain-dependent diffusion coefficients and hydraulic permeabilities. Their main conclusion was that dynamic loading enhanced the transport of large solutes more than small solutes, and the beneficial effect of dynamic loading on solute transport was stronger in the surface layer than deeper layers. For small solute (e.g. around 400 Da), the effect of dynamic compression was found to be more noticeable within the top layers but negligible in the bottom layers. For large molecules (e.g. around 400 kDa), the enhancement by dynamic loading was more obvious, even in deeper layers.

Our recent work [14] concluded that before dynamic loading can enhance the transport of solutes by advection there needs to be some sort of ‘symmetry breaking’ mechanism, otherwise solute can advectively move both into and out of the cartilage within each loading cycle with equal facility. Diffusion provides one symmetry breaking mechanism, however its importance is restricted spatially and temporally to where there are relatively steep solute concentration gradients (in which case the diffusional transport is significant anyway). Other symmetry breaking mechanisms have been suggested in our previous paper [14]. One of the more promising potential symmetry breaking mechanisms that is as yet unexplored theoretically is solute binding within the articular cartilage (e.g. IGFs binding to

IGF binding proteins). In one half of a loading cycle the solute is drawn into the cartilage along with pore fluid as the cartilage expands. The solute may then bind to the cartilage, effectively trapping it in the cartilage, providing dissociation takes longer than association of the solute with its binding site(s). In this case, the solute is no longer free to be expelled by advection in the 2nd (compressive) half of the loading cycle. This would arguably lead to a net enhancement of solute transport, in comparison to free diffusion. To date the effects of solute binding within articular cartilage have not yet been taken into consideration. The purpose of this paper is to investigate quantitatively the effect of including IGF binding on its transport into cartilage undergoing dynamic loading.

There are at least six IGF binding proteins (IGFBPs) governing the ‘free concentrations’ of IGFs (and consequently their bioactivity) [2,15–17]. It is suggested that the major functions of these binding proteins are to prolong the half-life of IGFs in cartilage and to regulate the bioavailability of IGFs in their interaction with cell surface receptors [2,18,19]. There are few studies that directly investigate the influence of IGF binding proteins on the IGF concentrations in cartilage. However, of particular relevance to the present study is the work by Bhakta et al. [20]. They investigated the specific binding of growth factors to articular cartilage discs, recording the uptake of radio-labeled IGF-I into cartilage discs as a function of the bath concentration of IGF-I. Importantly, the tissues used in their experiments had an architecture largely assembled *in vivo* to ensure that the tissue characteristics (including its porosity, three-dimensional molecular structures and interactions, local ionic character), closely resemble the physiological situation. They showed that the IGF uptake into the cartilage was a non-linear function of the bath concentration. In a related diffusive transport experiment by Garcia et al. [21], radio-labeled IGF-I was added to an upstream bath compartment and allowed to diffuse across a 400 μm thick cartilage disk. The resulting downstream concentration was continuously measured as a function of time. It was observed that the transport of IGF-I across the cartilage disk was dramatically slowed by binding of the growth factor to sites within the tissue. Together, the studies of Bhakta et al. [20] and Garcia et al. [21] provide strong evidence that the specific binding of IGFs to cartilage, (i.e. through IGF binding proteins) regulate the IGF-I transport through cartilage. The study of Bhakta et al. [20] is described in more detail in Free diffusion, where their findings are compared with our model predictions. We note here that based on the available equilibrium binding data [20], Garcia et al. [21] also developed a theoretical model to relate free and bound IGF-I based on the Langmuir isotherm by fitting the dissociation constant and binding site density to predict the equilibrium binding behavior of IGF-I, however they did not model time-dependent, non-equilibrium binding, with advection as described here, nor did they include cyclic loading.

To investigate the potential role of non-equilibrium binding of IGF-I within cartilage in enhancing the transport of IGF-I through cartilage undergoing cyclic loading, in the present study, we develop a coupled transport and mechanical deformation model based on porous media theory. We implement the law of mass action to model the reversible time-dependent binding of IGF-I to binding proteins [22]. The following section presents the general porous media model used to describe the deformation of the cartilage and the solute transport. Radial solute transport in cartilage applies the general model developed in Methods to the specific geometry of a cylindrical cartilage disc undergoing unconfined axial loading with radial transport of IGF. Results and discussion then presents and discusses model predictions.

Methods

The proposed model will be based on an upscaled porous media theory, in which the heterogeneity of the material on the micro-scale is ignored and only the relative volume ratios of the various phases are taken into account, along with a general form of their interactions [23–25]. The use of porous media theory to model cartilage mechanical behavior (and other biological tissues) is not a recent idea [26–28], however its use to model the transport nutrients through a cyclically loaded cartilage is relatively new [12–14].

In the framework of the theory of porous media, articular cartilage is treated as a mixture of a solid matrix, a liquid and a solute. In past models, the solute phase is invariably treated as an unbound (free) solute. In the present study however, we acknowledge that the total solute concentration (c^w) is comprised of both free and bound solute, so

$$c^w = c_F + c_B \quad (1)$$

where c_F is the concentration of unbound solute and c_B represents the concentration of solute bound onto the solid phase (e.g. via binding proteins). Both concentrations are given with respect to the fluid phase volume.

The volume fraction of solid, fluid and solute may be defined respectively as follows,

$$\phi^s = \frac{V^s}{V} \quad (2a)$$

$$\phi^f = \frac{V^f}{V} \quad (2b)$$

$$\phi^w = \frac{V^w}{V} \quad (2c)$$

where V^s , V^f and V^w are the volume of the solid, fluid and solute in the mixture volume V , respectively. As the volume of the solute phase is relatively small compared with other phases and does not add to the overall volume of the mixture (or the solid-phase volume in the case of bound solute), ϕ^w can be assumed to be zero. By definition the sum of all volume fractions is equal to 1, so we may assume

$$\phi^s + \phi^f \approx 1 \quad (3)$$

Conservation of mass

The governing equations are based on the mass balance of each component in the mixture. Conservation of mass of the solid phase may be expressed as

$$\frac{\partial(\phi^s \rho^s)}{\partial t} + \nabla \bullet (\phi^s \rho^s \mathbf{v}^s) = 0 \quad (4)$$

where ρ^s is the density of the solid phase and \mathbf{v}^s the velocity of the solid particles relative to a fixed representative element volume (REV). Similarly, conservation of mass for the fluid phase may be expressed as

$$\frac{\partial(\phi^f \rho^f)}{\partial t} + \nabla \bullet (\phi^f \rho^f \mathbf{v}^f) = 0 \quad (5)$$

where ρ^f is the density of the fluid phase and \mathbf{v}^f the true fluid velocity related to a fixed REV.

If we assume that the solid and fluid phases are incompressible, Eqs. (4) and (5), along with Eq. (3) lead to

$$\nabla \bullet [(1 - \phi^f) \mathbf{v}^s + \phi^f \mathbf{v}^f] = 0 \quad (6)$$

The fluid velocity relative to the solid-phase velocity is assumed to be proportional to the gradient of fluid pressure (i.e. Darcy's law), and is referred to here as the Darcy velocity (\mathbf{v}_d).

$$\mathbf{v}_d = \phi^f (\mathbf{v}^f - \mathbf{v}^s) = -\kappa \nabla p \quad (7)$$

where κ is the hydraulic permeability tensor. Substituting Eq. (7) into Eq. (4), we find that

$$\nabla \bullet (\mathbf{v}^s - \kappa \nabla p) = 0 \quad (8)$$

Eq. (8) is the first of our governing equations and links the cartilage matrix deformation to the interstitial fluid motion.

To derive solute transport equation, we extend the theory of contaminant transport in a deforming porous medium developed by Smith [29,30] to simulate solute transport in cartilage. Conservation of the mass of the solute in fluid phase can be expressed as

$$\frac{\partial(\phi^f c_F)}{\partial t} + \nabla \bullet \mathbf{J}_F = -s \quad (9)$$

where \mathbf{J}_F is the mass flux of solute in the fluid phase and $-s$ represents the solute mass sink. This solute sink is due to the binding of unbound solute to binding proteins attached to the solid phase, which may then be transported with the solid phase (as a bound complex). The conservation of mass of the bound solute in the solid phase is then described by

$$\frac{\partial[(1 - \phi^f) c_B]}{\partial t} + \nabla \bullet \mathbf{J}_B = s \quad (10)$$

where \mathbf{J}_B is the mass flux of solute binding complex in solid phase.

Summing Eqs. (9) and (10) leads to conservation of mass of solute in both the fluid and solid phases,

$$\frac{\partial(\phi^f c_F)}{\partial t} + \frac{\partial[(1 - \phi^f) c_B]}{\partial t} = -\nabla \bullet \mathbf{J}_F - \nabla \bullet \mathbf{J}_B \quad (11)$$

The basic form of diffusion is molecular diffusion, which is due to random motions molecules undergo in solvents (i.e. Brownian motion). Classically, diffusion problems have been analyzed using Fick's laws of diffusion. In this study, a modified form of Fick's law (to take into account the porous media) provides a way of relating fluid and solute phase velocities. With consideration of solute in porous media, the solute mass flux in the fluid phase is given by

$$\mathbf{J}_F = -\phi^f D \nabla c_F + \phi^f \mathbf{v}^f c_F \quad (12)$$

where D is the effective diffusion coefficient of the solute in the cartilage including the tortuosity factor for the cartilage matrix.

Assuming that bound solute transport through the solid phase via diffusion is negligible, the solute binding complex mass flux in the solid phase is equal to

$$\mathbf{J}_B = (1 - \phi^f) \mathbf{v}^s c_B \quad (13)$$

Then substituting Eqs. (12) and (13) into Eq. (11) leads to the transport equation for the solute in the cartilage

$$\frac{\partial(\phi^f c_F)}{\partial t} + \frac{\partial[(1 - \phi^f) c_B]}{\partial t} = -\nabla \bullet (-\phi^f D \nabla c_F + \phi^f \mathbf{v}^f c_F) - \nabla \bullet [(1 - \phi^f) \mathbf{v}^s c_B] \quad (14)$$

Further, substituting Eq. (7) into Eq. (14) leads to

$$\frac{\partial(\phi^f c_F)}{\partial t} + \frac{\partial[(1-\phi^f)c_B]}{\partial t} = -\nabla \bullet \left[-\phi^f D \nabla c_F + \phi^f c_F \left(\mathbf{v}^s - \frac{\kappa}{\phi^f} \nabla p \right) \right] - \nabla \bullet [(1-\phi^f)\mathbf{v}^s c_B] \quad (15)$$

Note that Eqs. (5) and (7) provide the following relationship

$$\frac{\partial(\phi^f)}{\partial t} + \nabla \bullet (\phi^f \mathbf{v}^s - \kappa \nabla p) = 0 \quad (16)$$

Using Eq. (16), we can simplify Eq. (15) to

$$\phi^f \frac{\partial c_F}{\partial t} + (1-\phi^f) \frac{\partial c_B}{\partial t} - \phi^f D \nabla^2 c_F + [\phi^f \mathbf{v}^s - \kappa \nabla p - \nabla(\phi^f D)] \bullet \nabla c_F + [(1-\phi^f)\mathbf{v}^s] \bullet \nabla c_B = 0 \quad (17)$$

Eq. (17) is the general transport governing equation for the solute in the deformable cartilage with consideration of binding of solute to the solid matrix. Eq. (17) is the second of our governing equations in the system of equations.

Conservation of linear momentum

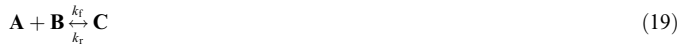
Assume the total stress tensor inside the cartilage is the sum of the interstitial fluid pressure and the ECM elastic stress. The balance of linear momentum equation yields [12,14]

$$-\nabla p + (\lambda_s + \mu_s) \nabla(\nabla \bullet \mathbf{u}^s) + \mu_s \nabla^2 \mathbf{u}^s = 0 \quad (18)$$

where \mathbf{u}^s is the solid-phase displacement vector, λ_s and μ_s are the Lamé constants. Eq. (18) together with Eqs. (8) and (17), are our governing equations to describe the mechanical and transport properties of a three-dimensional porous media. To close this system of equations we can introduce a model for solute binding (i.e. to relate c_F to c_B).

The law of mass action

Suppose a solute molecule (A) can combine with a binding protein molecule (B) to form a complex (C) and that the complex can also break into its original constituents.



where k_f is the rate constant for the association reaction (binding) and k_r is rate constant for the dissociation reaction. These chemical reactions can be described using the law of mass action [22,31,32]. It can be assumed that the concentration of bound solute (c_B) is jointly proportional to the concentration of solute (c_F) and (free or unbound) binding protein (c_{BP}). In addition, the rate at which the complex molecules break apart is assumed to be proportional to the concentration of solute complex (bound solute) that is present. These assumptions lead to the following set of equations which are collectively (with the assumptions) known as the law of mass action.

$$\frac{dc_B}{dt} = k_f c_F c_{BP} - k_r c_B \quad (20a)$$

$$\frac{dc_F}{dt} = -k_f c_F c_{BP} + k_r c_B \quad (20b)$$

$$\frac{dc_{BP}}{dt} = -k_f c_F c_{BP} + k_r c_B \quad (20c)$$

By adding Eqs. (20a) and (20c), we can obtain

$$\frac{dc_{BP}}{dt} + \frac{dc_B}{dt} = 0 \quad (21)$$

Thus, $c_{BP}(t) + c_B(t) = \text{constant}$. The integration constant can be obtained using the initial condition, leading to

$$c_{BP}(t) + c_B(t) = c_{BP0} + c_{B0} \quad \text{where } c_{BP}(t=0) = c_{BP0}, \quad c_B(t=0) = c_{B0} \quad (22)$$

Eliminating the binding protein concentration c_{BP} from Eq. (20a), through substitution of Eq. (22), we can obtain

$$\frac{dc_B}{dt} = k_f(c_{BP0} + c_{B0} - c_B)c_F - k_r c_B \quad (23)$$

Eq. (23) provides a relationship between c_F and c_B , and so closes our previous set of governing equations.

Radial solute transport in cartilage

Consider the case of a homogenous cylindrical disc of cartilage undergoing axisymmetric unconfined loading by an impermeable, frictionless barrier as shown in Fig. 1. Under this geometry we may assume the following.

- The axial strain is independent of the radial coordinate.
- There is no gradient of solute concentration (and therefore diffusion) in the axial direction.
- Due to symmetry, $\frac{\partial(\cdot)}{\partial \theta} = 0$ and furthermore we can assume $u_\theta = 0$.
- The strain in the axial direction is homogeneous—a condition only obtainable if the two impermeable plates are perfectly frictionless.

Thus, $p = p(r, t)$, $u_r^s = u_r(r, t)$, $u_z^s = u_z^s(z, t)$, $v_r = v_r(r, t)$, $c_F = c_F(r, t)$ and $c_B = c_B(r, t)$, where r and z are the radial and axial coordinates, respectively. Furthermore, it is assumed that the solid-phase velocity (and displacement) is equivalent to the cartilage velocity (and displacement), such that $\partial u_z^s / \partial z = \partial u_z / \partial z = \varepsilon(t)$, where $\varepsilon(t)$ is the applied strain, and the superscript s can be dropped from the velocity and displacement terms in the governing equations.

Hence, with consideration of infinitesimal strain, the governing Eqs. (8), (17) and (18) can be rewritten in radial coordinates as,

$$\frac{v_r}{r} + \frac{\partial v_r}{\partial r} + \frac{\partial \varepsilon_z}{\partial t} - \kappa_r \left(\frac{\partial^2 p}{\partial r^2} + \frac{1}{r} \frac{\partial p}{\partial r} \right) = 0 \quad (24)$$

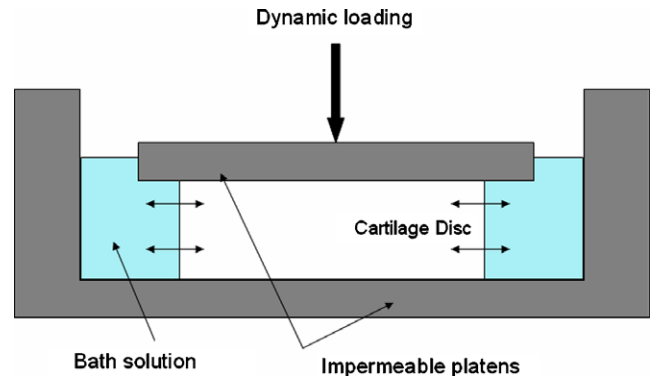


Fig. 1. A schematic diagram of a cylindrical cartilage tissue construct between frictionless impermeable platens in a bath containing a solute (e.g. IGF-I) undergoing unconfined axial sinusoidal dynamic loading.

$$\begin{aligned} \phi^f \frac{\partial c_F}{\partial t} + (1 - \phi^f) \frac{\partial c_B}{\partial t} - \phi^f D \left(\frac{\partial^2 c_F}{\partial r^2} + \frac{1}{r} \frac{\partial c_F}{\partial r} \right) \\ + \left(\phi^f v_r - \kappa_r \frac{\partial p}{\partial r} \right) \frac{\partial c_F}{\partial r} + (1 - \phi^f) v_r \frac{\partial c_B}{\partial r} = 0 \end{aligned} \quad (25)$$

$$-\frac{\partial p}{\partial r} + H_A \left(-\frac{u_r}{r^2} + \frac{1}{r} \frac{\partial u_r}{\partial r} + \frac{\partial^2 u_r}{\partial r^2} \right) = 0 \quad (26)$$

where

$$\frac{\partial u_r}{\partial t} = v_r \quad (27)$$

The first and second terms in Eq. (25) are the change of concentration of both unbound and bound solute complex with respect to time; the 3rd term is the unbound solute transported by free diffusion; the 4th and 5th terms are the contribution of mechanical loading and advection in the deforming porous media. Eqs. (24)–(27) together with Eq. (23) form the set of governing equations in the cylindrical coordinates.

If the porous material is deformable, but without binding, the governing Eq. (25) can be simplified to

$$\phi^f \frac{\partial c_F}{\partial t} - \phi^f D \left(\frac{\partial^2 c_F}{\partial r^2} + \frac{1}{r} \frac{\partial c_F}{\partial r} \right) + \left(\phi^f v_r - k_r \frac{\partial p}{\partial r} \right) \frac{\partial c_F}{\partial r} = 0 \quad (28)$$

Eq. (28) is consistent with our previous study [14].

Boundary conditions

The assumed applied strain is in the axial direction and is of sinusoidal form, that is

$$\varepsilon_z = \frac{\varepsilon_0}{2} [1 - \cos(2\pi f t)] \quad (29)$$

where ε_0 is the peak-to-peak strain amplitude and f is the loading frequency. Consequently, transport of a solute is purely in the radial direction. It is also assumed that the bath surrounding the cartilage is well-mixed, such that the solute concentration at the cartilage surface ($r = r_0$) is constant. In this study, boundary conditions are required at $r = 0$ and $r = r_0$. All velocities are zero at $r = 0$ (due to axisymmetric conditions). This leads to,

$$\begin{aligned} u_r(0, t) = 0, \quad \left(\frac{\partial u_r}{\partial r} \right)_{r=0} = 0, \\ \left(\frac{\partial c_F}{\partial r} \right)_{r=0} = 0, \quad \left(\frac{\partial c_B}{\partial r} \right)_{r=0} = 0, \quad \left(\frac{\partial p}{\partial r} \right)_{r=0} = 0 \end{aligned} \quad (30)$$

At the boundary interface ($r = r_0$), the quantities ϕ^f and ϕ^s each exhibit a discontinuity across the interface. The requirement that the traction traction should be continuous across this boundary [33] leads to

$$\left(\frac{\partial u_r}{\partial r} \right)_{r=r_0} = -\frac{v}{1-v} \left(\frac{u_r|_{r=r_0}}{r_0} + \varepsilon_z \right) \quad (31)$$

where v is Poisson's ratio.

Numerical solution

The commercial Finite Element software FEMLAB was employed to solve the governing equations numerically. The applied strain protocol is discretized into fixed time steps. At each time step, the unbound solute concentration c_F , bound solute complex concentration c_B , solid-phase displacement u_r , solid-phase velocity v_r , and interstitial fluid pressure p are calculated.

Results and discussion

Before presenting model results, it is useful to first define the total solute uptake ratio (R_u), the free solute uptake ratio (R_F) and the bound solute uptake ratio (R_B). These parameters provide a measure of the solute concentration in the cartilage compared to the bath concentration. Simply stated the total solute uptake ratio is the sum of free solute uptake ratio (R_F) and bound solute uptake ratio (R_B), viz,

$$R_u = R_F + R_B \quad (32)$$

where

$$R_F = \frac{c_F}{c_0} \quad \text{and} \quad R_B = \frac{c_B}{c_0} \quad (33)$$

and c_0 is the solute bath concentration.

Since the solute concentration is generally non-uniform in the radial direction, average solute uptake ratios can also be defined. The average total (\bar{R}_u), the average free \bar{R}_F and the average bound \bar{R}_B uptake ratios are provided below in Eq. (34)

$$\bar{R}_u = \bar{R}_F + \bar{R}_B \quad (34)$$

where

$$\bar{R}_F = \frac{\int_0^{r_0} 2\pi r R_F dr}{\int_0^{r_0} 2\pi r dr} \quad \text{and} \quad \bar{R}_B = \frac{\int_0^{r_0} 2\pi r R_B dr}{\int_0^{r_0} 2\pi r dr} \quad (35)$$

Free diffusion

The objective of this initial free diffusion (no applied strain) study is to validate our model by comparing the numerical predictions with Bhakta et al's experimental data of equilibrium binding of IGF-I to cartilage [20]. Numerical predications of free diffusion in the absence of binding are also presented to investigate the role of binding on the transport of solute within cartilage tissue.

In Bhakta et al's experimental study [20], adult bovine articular cartilage disks (3 mm diameter \times 0.4 mm thick) were examined. The disks were equilibrated in solutions containing ^{125}I -IGF-I (~ 0.033 nM) and graded amounts of unlabeled IGF-I for 48 h. The radioactive counts in each disk were normalized to the tissue water weight (cpm/mg) and divided by the radioactive counts per volume (cpm/ml) of the equilibrating solution.

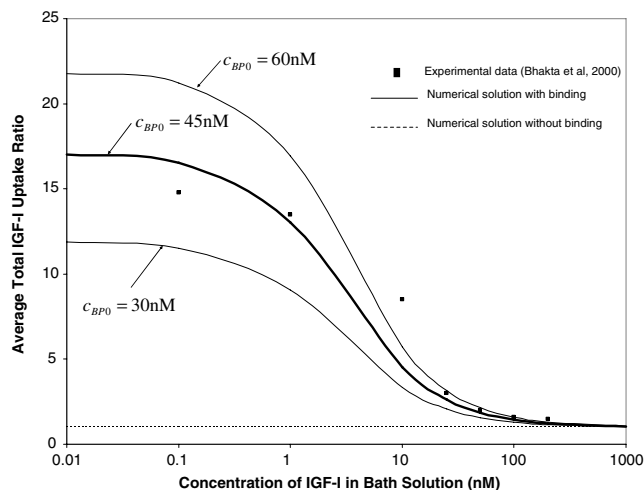


Fig. 2. Comparison of average total IGF-I uptake ratio (\bar{R}_u) as a function of concentration of IGF-I in the bath solution, at various binding protein concentrations (c_{BPO}) after 48 h of free diffusion.

The numerical predictions of free diffusion with and without consideration of binding are compared with experimental data [20] in Fig. 2. The average total uptake ratio (\bar{R}_u) is calculated after 48 h free diffusion and equilibrium binding. The parameters used in our theoretical predictions are listed in Table 1. In vivo, IGF-I may interact with various types of binding proteins, as well as cartilage cell surface receptors (resulting in signal generation) [34]. In this study, however, to simplify the problem, we only take into account the interaction between IGF-I and IGFBP-3 because the most abundant binding protein in serum is IGFBP-3 and IGF-I is mostly found in a complex formed with IGFBP-3 [18]. In the past years, many experimental efforts have been done to determine the binding rate constants in protein systems [16,17,22,35,36]. Recently, Cassion [37] reviewed previous experimental studies and performed experiments using surface plasmon resonance (SPR) to determine the association and dissociation constants for the binding of IGF-I and IGFBP-3 at pH 7.4 and pH 5.8, respectively. In this study, we adopt the values for the association and dissociation constants obtained by Cassion, specifically the results at pH 7.4 (see Tables 1 and 2). Clearly the above assumptions may not be appropriate for cartilage, that is IGF-I may not be binding (only) to IGFBP-3 or if it is the available binding constants for

Table 1
Material parameters used for comparison with Bhakta et al's experimental data [20]

Parameter	Value	Ref.
Radius of cartilage disc (r_0)	1.5 mm	[20]
Hydraulic permeability (κ_r)	$2 \times 10^{-15} \text{ m}^4/\text{Ns}$	[44]
Aggregate elastic modulus (H_A)	0.27 MPa	[45]
Diffusion coefficient (D)	$4.1 \times 10^{-11} \text{ m}^2/\text{s}$	[20]
Fluid phase volumetric fraction (ϕ^f)	0.8	[44,45]
Association rate constant (k_f)	$3.67 \times 10^5 \text{ M}^{-1} \text{ s}^{-1}$	[37]
Dissociation rate constant (k_r)	0.001 s^{-1}	[37]

Table 2
Range of parameters used throughout this study

Parameter	Value	Ref.
Radius of cartilage disc (r_0)	1 mm	
Boundary IGF-I concentration (c_0)	40 nM	
Hydraulic permeability (κ_r)	$2 \times 10^{-15} \text{ m}^4/\text{Ns}$	[44]
Aggregate elastic modulus (H_A)	0.27 MPa	[45]
Diffusion coefficient (D)	$5 \times 10^{-12} \text{ m}^2/\text{s}$	[45]
Fluid phase volumetric fraction (ϕ^f)	0.8	[44,45]
Binding protein concentration (c_{BPO})	50.1 nM	[21]
Association rate constant (k_f)	$3.67 \times 10^5 \text{ M}^{-1} \text{ s}^{-1}$	[37]
Dissociation rate constant (k_r)	0.001 s^{-1}	[37]

association and dissociation at a pH 7.4 are not relevant to the pH in cartilage. However the values used for the binding constants and the assumption of a single binding protein interaction with IGF-I should be thought of as a first estimate.

As Morales et al. [38] suggested that the IGF-BP concentration in bovine cartilage approximately ranged from 30 to 150 nM, the numerical results at various IGF-BP concentrations (c_{BPO}) are also presented in Fig. 2. From Fig. 2 we can see that theoretical results with binding fit well with the experimental data when the IGF-BP concentration is around 45 nM. However, if the binding effects are not accounted for, the numerical predictions severely underestimate the \bar{R}_u at very low solute bath concentrations. Only at high bath concentration can the effect of binding on transport be neglected. This trend is consistent with the trends of a previous experimental and theoretical study by Garcia et al. [21]. Experimental investigations discovered that IGF-I concentration was low (around 20–50 ng/ml) in both human normal synovial fluid and cartilage [4–6]. Therefore we can conclude from the results presented in Fig. 2 that it is important to include binding effects into solute transport mathematical models.

Diffusion with cyclic deformation

The mechanical response of cartilage is strongly tied to the ability of fluid to flow through the cartilage matrix. Some observations suggest that cartilage behaves like a sponge, albeit one that does not allow fluid to flow through it easily [39]. In normal articular cartilage, advective transport is potentially an important transport mechanism. Thus, the effects of dynamic loading on both unbound solute and bound solute complex need critical investigation. Here parameters given in Table 2 are adopted to enable direct comparison with our previous work [14].

The percent increase of \bar{R}_u , \bar{R}_F and \bar{R}_B relative to the free diffusion case is plotted in Fig. 3 for various initial bath concentrations, and as a function of time. It demonstrates that under the same dynamic loading conditions, lower bath solute concentration results in higher percent increase of both the unbound solute and bound solute uptake ratio, compared to free diffusion. That is, the enhanced transport due to dynamic loading is most pronounced when the bath

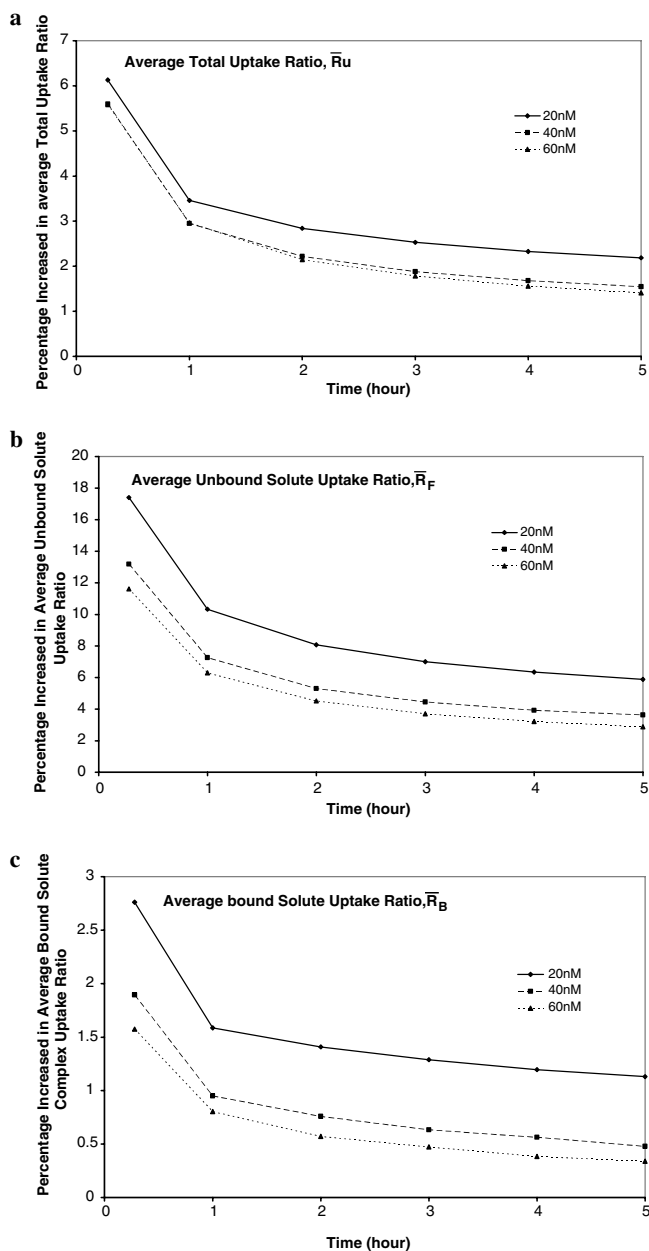


Fig. 3. Percent increase in average total solute uptake ratio (\bar{R}_u), average unbound solute uptake ratio (\bar{R}_F) and average bound solute uptake ratio (\bar{R}_B) as a function of time, at various solute bath concentrations ($f = 0.1$ Hz, $\varepsilon_0 = 2\%$).

solute concentration is the lowest. However for all bath concentrations the benefits of cyclic loading are lost after ~ 5 h, with the concentrations of bound and unbound solutes being indistinguishable from the free diffusion case. This transient nature of the enhanced transport is consistent with our previous findings [14] when binding is neglected. Moreover, loading frequency has more of a significant effect on the unbound solute concentration within the tissue, rather than the bound solute concentration—although both show enhancement when compared to the free diffusion case.

It has been hypothesized that the ECM associated IGFbps could act as a reservoir for IGF-I, sequestering

it for later release and transport, and consequently promote controlled localized delivery of IGF-I [40]. A study of IGFbps in human articular cartilage [41] reported an increase in IGFBP-3 during osteoarthritis with an auto-crine IGFBP-3 production in the diseased cartilage. Moreover, it has been reported that the surface zone of normal cartilage produced more IGFBP-3 than the deep zone [42]. Thus, the interactions between IGF-I and IGFbps together with the concentration level of IGFbps may impact upon IGF-I transport. To investigate this hypothesis, the percent increase in average total solute uptake ratio (\bar{R}_u), average unbound solute uptake ratio (\bar{R}_F) and average bound solute uptake ratio (\bar{R}_B) as a function of concentration of IGF-I in the bath solution, for various binding protein concentrations (c_{BP0}), are shown after 20 min of dynamic compression in Fig. 4. Note the range of binding protein concentrations examined 30–150 nM is consistent with those reported by Morales [7]. The results presented in Fig. 4 suggest that, if IGF-I concentration is low in the synovial fluid, high IGFBP concentration together with cyclic loading significantly increases both unbound and bound solute concentration. However, the influence of the concentration level of IGFBP becomes negligible if the solute bath concentration is high, due to the saturation of a finite number of binding sites.

In vivo, the binding behavior of IGF-I in cartilage is a complex phenomenon and still remains unclear to date. In particular, the affinity constants of IGF–IGFBP interactions may vary due to various types of IGFBP, pH values, experimental methods etc. To further understand the kinetics of binding interactions between IGF-I and IGFbps, parametric studies are carried out based on the available experimental data [16,17,22,35–37,43]. Fig. 5 shows the percent increase in average total solute uptake ratio (\bar{R}_u), average unbound solute uptake ratio (\bar{R}_F) and average bound solute uptake ratio (\bar{R}_B) as a function of concentration of IGF-I in the bath solution, at various normalized association rate constants (k_f/k_{f0}) ranging from 0.1 to 10, after 20 min dynamic compression ($f = 0.01$ Hz, $\varepsilon_0 = 2\%$, $k_{r0} = 0.001$ s $^{-1}$, $k_{f0} = 3.67 \times 10^5$ M $^{-1}$ s $^{-1}$). It can be seen that a high association rate constant (e.g. $k_f/k_{f0} = 10$), together with the dynamic compression, results in the greatest increment of unbound and bound IGF-I concentration within the cartilage, but only in very low IGF-I bath concentration (e.g. <10 nM). In contrast, for a low association rate constant (e.g. $k_f/k_{f0} = 0.1$), the enhancement is very small and independent of IGF-I bath concentration.

Fig. 6 shows the effect of frequency on solute uptake. Frequencies range from 0.01 to 1 Hz. Consistent with other research investigations [12–14], it indicates that increasing the loading frequency enhances solute transport. There is some indication that the bound solute concentration enhancement is more sensitive to frequency than the unbound concentration. From Fig. 6, we see that the transport enhancement for all frequencies declines with time.

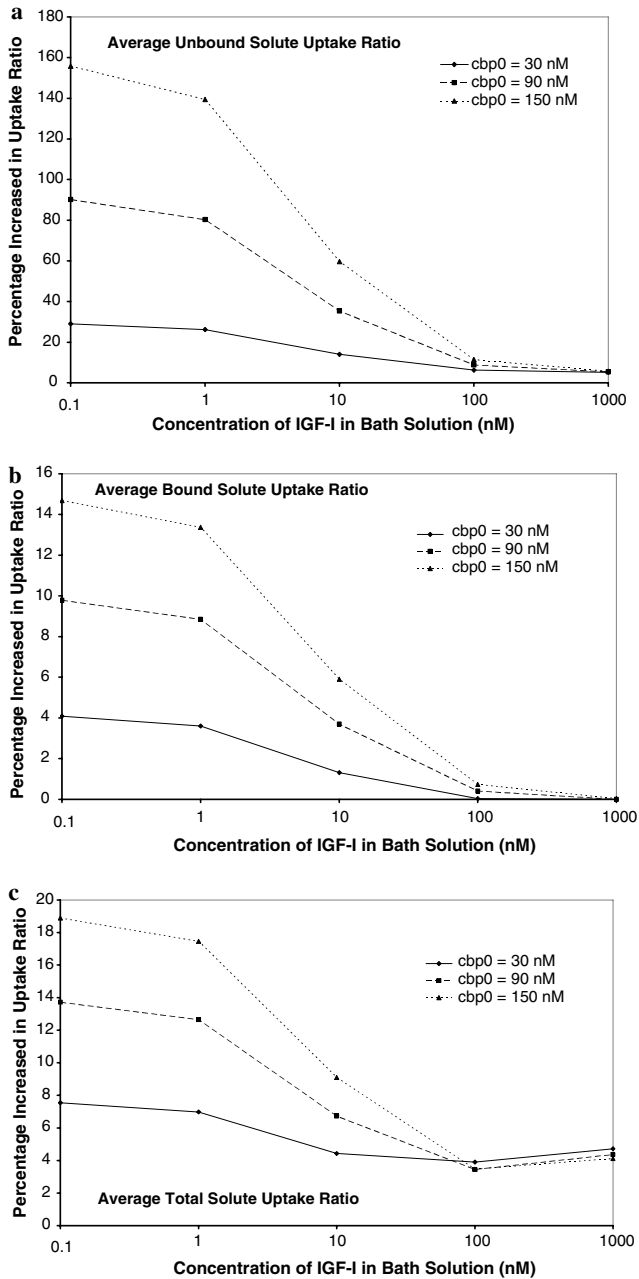


Fig. 4. Percent increase in average total solute uptake ratio (\bar{R}_T), average unbound solute uptake ratio (\bar{R}_F) and average bound solute uptake ratio (\bar{R}_B) as a function of concentration of IGF-I in the bath solution, at various binding protein concentrations (c_{BP0}) after 20 min dynamic compression ($f = 0.01$ Hz, $\varepsilon_0 = 2\%$, $k_{r0} = 0.001$ s $^{-1}$, $k_{f0} = 3.67 \times 10^5$ M $^{-1}$ s $^{-1}$).

The effects of the various peak to peak strain magnitudes on total solute concentration as a function of time are presented in Fig. 7. As expected, the high strain magnitudes (e.g. 6% and 10%) produce the greatest enhancement in total solute concentration. Although not shown, the high strain magnitudes increase both average unbound and bound solute concentration and the beneficial effects on unbound solute are seen to be more dramatic.

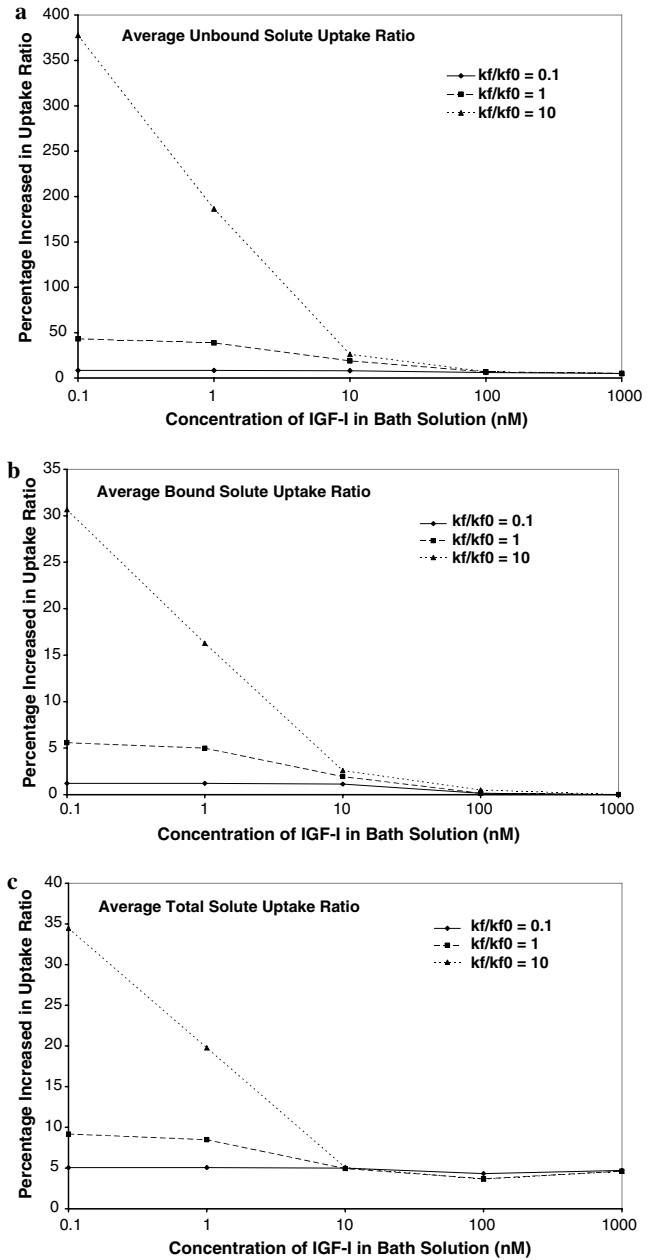


Fig. 5. Percent increase in average total solute uptake ratio (\bar{R}_T), average unbound solute uptake ratio (\bar{R}_F) and average bound solute uptake ratio (\bar{R}_B) as a function of concentration of IGF-I in the bath solution, at various normalized association rate constants (k_f/k_{f0}) after 20 min dynamic compression ($f = 0.01$ Hz, $\varepsilon_0 = 2\%$, $k_{r0} = 0.001$ s $^{-1}$, $k_{f0} = 3.67 \times 10^5$ M $^{-1}$ s $^{-1}$).

From the above, the optimal loading regime to enhance solute transport should correspond to high strains and high loading frequency. To test this hypothesis the strain amplitudes ranging from 2% to 10% are combined with frequencies ranging from 0.01 to 1 Hz. The average percent increase in total solute uptake ratio in comparison to free diffusion is calculated after 5 h of cyclic loading. Predictions are shown in Table 3. It can be seen that the combination of 10% strain and 1 Hz frequency leads to

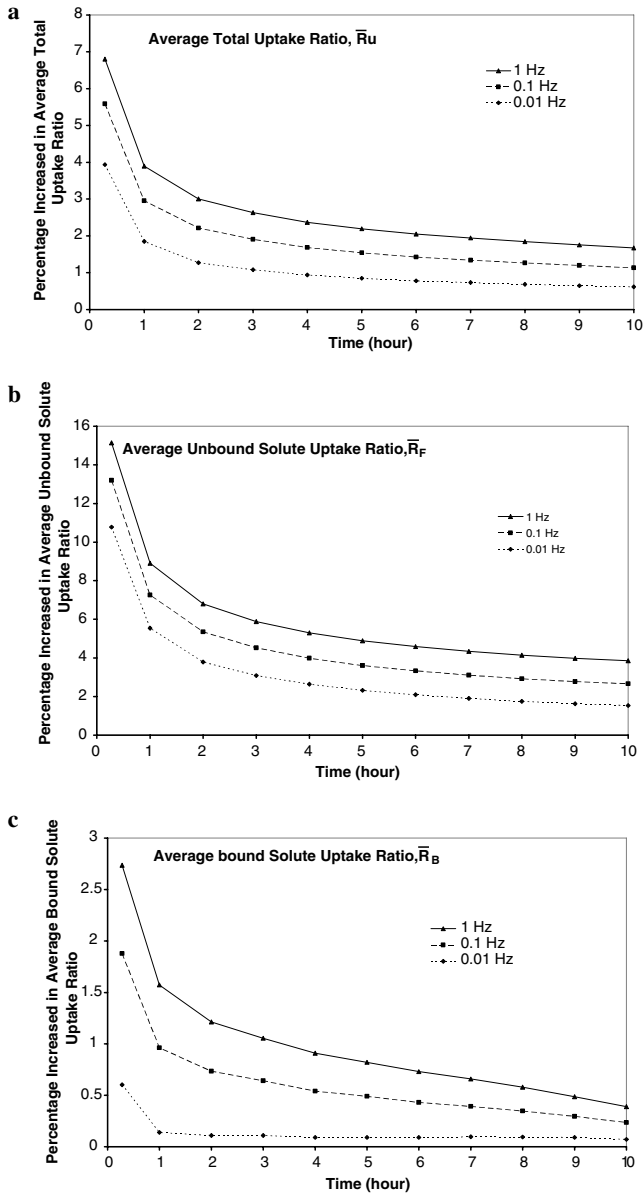


Fig. 6. Percent increase in the average total solute uptake ratio (\bar{R}_u), average unbound solute uptake ratio (\bar{R}_f) and average bound solute uptake ratio (\bar{R}_b) as a function of time, at various dynamic loading frequencies ($\epsilon_0 = 2\%$, $c_0 = 40$ nM).

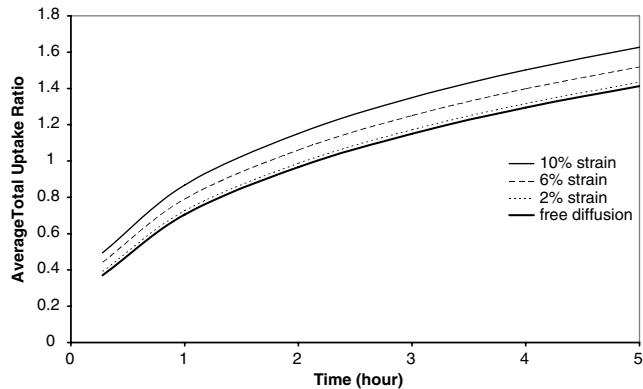


Fig. 7. Average total solute uptake ratio (\bar{R}_u) as a function of time, at various peak-to-peak strain amplitudes ($f = 0.1$ Hz, $c_0 = 40$ nM).

Table 3

Average percent increase in total solute uptake ratio (in comparison to free diffusion) after 5 h of applied cyclic loading

Cycle frequency (Hz)	2% Strain	6% Strain	10% Strain
0.01	1.7	6.5	11.7
0.1	2.6	10.9	20.7
1	3.5	16.1	28.0

the greatest total solute enhancement, with 20–30% increment compared to free diffusion.

Conclusion

This paper describes solute transport through articular cartilage under cyclic loading and with solute binding to the extra-cellular matrix. A quantitative model was developed based on porous media theory, and it was used to describe the coupled solute transport and the mechanical behavior of cartilage. The model was used to explore the system behaviour for solute transport with free diffusion and advective-diffusion, and particular attention was given to the role of bath concentration, applied loading frequency and strain. A summary of the main findings are as follows

- At low initial solute bath concentrations, neglecting binding leads to a significant underestimation of the total solute concentration in the cartilage for both the case of free diffusion and cyclic deformation. However the effect of binding is negligible when bath concentration is high due to the finite number of binding sites. It is suggested that as the typical concentration of IGF-I is low in healthy human synovial fluid and cartilage, the binding effects cannot generally be ignored in mathematical models of IGF transport in cartilage.
- Dynamic compression generally enhances both unbound and bound solute concentration within the cartilage tissue, in comparison to free diffusion.
- Increasing loading frequency increases total solute concentration.
- Higher peak to peak strain magnitudes (e.g. 6% and 10% strain) lead to the greatest enhancement in the total solute concentration.
- The combination of high loading frequencies (e.g. 1 Hz) and high strain amplitude (up to 10%) leads to the greatest increase in the solute concentration (e.g. approximately 20–30% average increment within the first 5 h).

Finally we conclude that solute binding to the cartilage solid-phase is an efficient symmetry breaking mechanism enhancing solute transport into cartilage.

Acknowledgments

The authors thank The Australian Research Council (DP50192) and The University of Melbourne for their support.

References

- [1] A.J. Grodzinsky, M.E. Levenston, M. Jin, E.H. Frank, *Annual Review of Biomedical Engineering* 2 (2000) 691–713.
- [2] J.I. Jones, D.R. Clemmons, *Endocrine Reviews* 16 (1995) 3–34.
- [3] F.P. Luyten, V.C. Hascall, S.P. Nissley, T.I. Morales, A.H. Reddi, *Archives of Biochemistry and Biophysics* 267 (1988) 416–425.
- [4] R. Schneiderman, E. Snir, O. Popper, J. Hiss, H. Stein, A. Maroudas, *Archives of Biochemistry and Biophysics* 324 (1995) 159–172.
- [5] R. Schneiderman, N. Rosenberg, J. Hiss, P. Lee, F. Liu, R.L. Hintz, A. Maroudas, *Archives of Biochemistry and Biophysics* 324 (1995) 173–188.
- [6] C. Tavera, T. Aribat, P. Reboul, S. Dore, P. Brazeau, J.-P. Pelletier, J. Martel-Pelletier, *Osteoarthritis and Cartilage* 4 (1996) 263–274.
- [7] T.I. Morales, *Archives of Biochemistry and Biophysics* 315 (1994) 190–198.
- [8] M.L. Gray, A.M. Pizzanelli, A.J. Grodzinsky, R.C. Lee, *Journal of Orthopaedic Research* 6 (1988) 777–792.
- [9] Y.-J. Kim, R.L. Sah, A.J. Grodzinsky, A.H. Plaas, J.D. Sandy, *Archives of Biochemistry and Biophysics* 311 (1994) 1–12.
- [10] Y.-J. Kim, L.J. Bonassar, A.J. Grodzinsky, *Journal of Biomechanics* 28 (1995) 1055–1066.
- [11] M.D. Buschmann, Y.A. Gluzband, A.J. Grodzinsky, E.B. Hunziker, *Journal of Cell Science* 108 (1995) 1497–1508.
- [12] R.L. Mauck, C.T. Hung, G.A. Ateshian, *Journal of Biomechanical Engineering* 125 (2000) 602–614.
- [13] L. Zhang, A.Z. Szeri, *Proceedings of the Royal Society* 461 (2005) 2021–2042.
- [14] B.S. Gardiner, D.W. Smith, P. Pivonka, A.J. Grodzinsky, E.H. Frank, L. Zhang, Submitted for publication (2006).
- [15] W.F. Blum, E.W. Jenne, F. Reppin, K. Kietzmann, M.B. Ranke, J.R. Bierich, *Endocrinology* 125 (1989) 766–772.
- [16] Y. Dubaquié, H.B. Lowman, *Biochemistry* 38 (1999) 6386–6396.
- [17] M.-S. Wong, C.-C. Fong, M. Yang, *Biochimica et Biophysica Acta* 1432 (1999) 293–301.
- [18] P.F. Collett-Solberg, P. Chen, *Endocrine* 12 (2000) 121–136.
- [19] T. Arai, A. Parker, J. Walker Busby, D.R. Clemmons, *The Journal of Biological Chemistry* 269 (1994) 20388–20393.
- [20] N.R. Bhakta, A.M. Garcia, E.H. Frank, A.J. Grodzinsky, T.I. Morales, *The Journal of Biological Chemistry* 275 (2000) 5860–5866.
- [21] A.M. Garcia, N. Szasz, S.B. Trippel, T.I. Morales, A.J. Grodzinsky, E.H. Frank, *Archives of Biochemistry and Biophysics* 415 (2003) 69–79.
- [22] C.-C. Fong, M.-S. Wong, W.-F. Fong, M. Yang, *Analytica Chimica Acta* 456 (2002) 201–208.
- [23] N. Mills, *International Journal of Engineering Science* 4 (1966) 97–112.
- [24] R.E. Craine, *International Journal of Engineering Science* 9 (1971) 1177–1192.
- [25] R.M. Bowen, *International Journal of Engineering Science* 18 (1980) 1129–1148.
- [26] G.A. Ateshian, M.A. Soltz, R.L. Mauck, I.M. Basalo, C.T. Hung, W.M. Lai, *Transport in Porous Media* 50 (2003) 5–33.
- [27] V.C. Mow, S.C. Kuei, W.M. Lai, C.G. Armstrong, *Journal of Biomechanical Engineering* 102 (1980) 73–84.
- [28] W.Y. Gu, W.M. Lai, V.C. Mow, *Journal of Biomechanical Engineering* 120 (1998) 169–180.
- [29] D.W. Smith, *International Journal for Numerical and Analytical Method in Geomechanics* 24 (2000) 693–722.
- [30] G.P. Peters, D.W. Smith, *International Journal for Numerical and Analytical Method in Geomechanics* 26 (2002) 683–717.
- [31] A.S. Lee, *Modeling Dynamic Phenomena in Molecular and Cellular Biology*, Cambridge University Press, Cambridge, 1984.
- [32] S. Stumm, J.M. James, *Aquatic Chemistry*, John Wiley & Sons, Inc, New York, 1996.
- [33] J.S. Hou, M.H. Holmes, W.M. Lai, V.C. Mow, *Journal of Biomechanical Engineering* 111 (1989) 78–87.
- [34] D.A. Lauffenburger, J.J. Linderman, *Receptors: Models for Binding, Trafficking and Signaling*, Oxford University Press, New York, 1993.
- [35] P. Vorwerk, B. Hohmann, Y. Oh, R.G. Rosenfeld, R.M. Shymko, *Endocrinology* 143 (2002) 1677–1685.
- [36] A. Heding, R. Gill, Y. Ogawa, P.D. Meyts, R.M. Shymko, *The Journal of Biological Chemistry* 271 (1996) 13948–13952.
- [37] T.R. Cassino, Quantification of the binding of Insulin-like growth factor-I (IGF-I) and IGF binding protein-3 (IGFBP-3) using surface plasmon resonance, Master of Science thesis, Department of Chemical Engineering, Virginia Polytechnic Institute and State University (2002).
- [38] T.I. Morales, *Archives of Biochemistry and Biophysics* 343 (1997) 164–172.
- [39] A. Maroudas, P. Bullough, *Nature* 219 (1968) 1260–1261.
- [40] J.M.D. Paye, K. Forsten-Williams, *Annals of Biomedical Engineering* 34 (2006) 618–632.
- [41] T.I. Morales, *Arthritis & Rheumatism* 46 (2002) 2358–2367.
- [42] T. Eviatar, H. Kauffman, A. Maroudas, *Arthritis & Rheumatism* 48 (2003) 410–417.
- [43] M. Galanis, S.M. Firth, J. Bond, A. Nathanielsz, A.A. Kortt, P.J. Hudson, R.C. Baxter, *Journal of Endocrinology* 169 (2001) 123–133.
- [44] V.C. Mow, J.S. Hou, J.M. Owens, A. Ratcliffe, *Biphasic and quasilinear viscoelastic theories for hydrated soft tissues Biomechanics of Diarthrodial Joints*, Springer-Verlag, New York, 1990, 215–260.
- [45] L.J. Bonassar, A.J. Grodzinsky, A. Srinivasan, S.G. Davila, S.B. Trippel, *Archives of Biochemistry and Biophysics* 379 (2000) 57–63.

Conclusions and Perspectives

Hierarchical modeling of transport processes through (deformable) porous materials is essential in many fields of engineering including civil-, geotechnical-, geo-environmental, and biomedical engineering. Whereas the application of microscale models allows investigation of detailed processes at lower scales most engineering problems are concerned with the investigation of macroscale phenomena. The major advantage of using macroscopic equations based on up-scaling procedures is that detailed information from the microscale is incorporated into the macroscale governing equations. Hence once a model is calibrated for a particular experimental setup, variations of the experimental boundary conditions can be investigated without running further experiments. On the other hand, macroscopic parameters used in phenomenological equations have to be calibrated for each experiment separately, which is expensive and time consuming.

Hierarchical models don't only apply to different spatial scales but also to different time scales. In particular most biological systems are characterized by a vast range of different spatial scales (10^{-9} m-1m) and temporal scales (10^{-6} s- 10^9 s). They play a most fundamental role from gene up-regulation, to protein synthesis, to the final cell response. Currently, our group focuses on multiscale modeling of coupled phenomena in charged porous materials. Insight gained into swelling will help to better understand transport behaviour through clay materials and cartilage which are both characterized by a large swelling capacity. One important aspect in my biomedical research is to include biophysical and biochemical phenomena of tissue into engineering models. For example, in cartilage mechanics it is essential to incorporate chondrocyte biosynthesis into general reactive transport models (such as the one described above). Biosynthesis leads to production of proteoglycans and other proteins which results in changes in pore morphology of the cartilage matrix which are intrinsically linked to macroscopic properties such as permeability and stiffness of the material. Changes of these properties will then influence the transport and deformation behaviour of the cartilage. Hence, it is important to fully couple biological and mechanical aspects.. Another research interest of mine is related to bone biology and in particular to bone remodeling. Bone remodeling is the continuous process of bone resorption and bone formation executed by different types of bone cells.

The long term perspective of hierarchical models for cartilage, bone and other tissues is that they can be used for patient-specific monitoring of disease states and for development of new therapeutic strategies. However, an important aspect in the development of such models is to not only incorporate mechanical features, but also to include the biological characteristics of the specific tissue. Hence, collaborations between engineers and biologists may be essential in achieving this goal. Such approaches will lead to significant improvements in current clinical practice. It is hoped that patient-specific information can reduce to a minimum of risk factors, that are usually related to a whole population. .

Bibliography

- Atkins, P., and J. de Paula. 2002. Physical chemistry, 7th edition. Oxford University Press, New York.
- Auriault, J.-L., and J. Lewandowska. 1996. Diffusion/adsorption/advection macrotransport in soils. *European Journal of Mechanics, A/Solids* **15**:681-704.
- Bear, J., and Y. Bachmat. 1991. Introduction to modeling of transport phenomena in porous materials. Kluwer, Dordrecht.
- Cassman, M., A. Arkin, F. Doyle, F. Katagiri, D. Lauffenburger, and C. Stokes. 2005. WTEC Panel Report on International Research and Development in Systems Biology. World Technology Evaluation Centre (WTEC).
- Cushman, J. H. 1997. The physics of fluids in hierarchical porous media: angstroms to miles. Kluwer, Dordrecht.
- Evans, D. F., and H. Wennerstroem. 1999. The colloidal domain. Wiley-VCH, New York.
- Fletcher, H. R., D. W. Smith, and P. Pivonka. 2006. Modeling the Sorption of Fluoride onto Alumina. *Journal of Environmental Engineering* **132**:229-246.
- Gardiner, B., D. Smith, P. Pivonka, A. Grodzinsky, E. Frank, and L. Zhang. 2007. Solute transport in cartilage undergoing cyclic deformation. *Computer Methods in Biomechanics and Biomedical Engineering*. (in print)
- Grodzinsky, A. J. 2000. Fields, forces and flows in biological systems. Course notes Massachusetts Institute of Technology.
- Helfferich, F. G. 1962. Ion exchange. Dover Publications, New York.
- Hunter, R. J. 2002. Foundations of colloid science, 2nd edition. Oxford University Press, New York.
- Mauck, R. L., C. T. Hung, and G. A. Ateshian. 2003. Modeling of neutral solute transport in a dynamically loaded porous permeable gel: implications for articular cartilage biosynthesis and tissue engineering. *J. Biomech. Eng.* **125**:602-614.
- Mitchell, J. K., and K. Soga. 2005. Fundamentals of soil behavior, 3rd edition. John Wiley & Sons, New Jersey.
- Narsilio, G. A., R. Li, P. Pivonka, and D. Smith. 2007. Comparative study of methods used to determine ionic diffusion coefficients using migration tests. *Cement and Concrete Research*. (accepted for publication)
- Pivonka, P., C. Hellmich, and D. Smith. 2004. Microscopic effects on chloride diffusivity of cement pastes - a scale transition analysis. *Cement and Concrete Research* **34**:2251-2260.
- Pivonka, P., and D. Smith. 2005. Investigation of nanoscale electrohydrodynamic transport phenomena in charged porous materials. *International Journal for Numerical Methods in Engineering* **63**:1975-1990.
- Pivonka, P., D. Smith, and B. Gardiner. 2007. Investigation of Donnan equilibrium in charged porous materials—a scale transition analysis. *Transport in porous media*. (in print)
- Pivonka, P., D. W. Smith, and B. S. Gardiner. 2005. Upscaling of the Poisson-Nernst-Planck equations using the volume averaging method. Pages 443-446 *in* T. E.

- Simos, G. Psihoyios, and C. Tsitouras, editors. International Conference on Numerical Analysis and Applied Mathematics 2005. Wiley-VCH, Rhodes, Greece.
- Revil, A. 1999. Ionic diffusivity, electrical conductivity, membrane and thermodynamic potentials in colloids and granular porous materials. *J. Colloid Interface Sci.* **212**:503-522.
- Sen, P. N. 1989. Unified model of conductivity and membrane potential of porous media. *Phys. Rev. B* **39**:9508-9517.
- Smith, D., P. Pivonka, C. Jungnickel, and S. Fityus. 2004. Theoretical analysis of anion exclusion and diffusive transport through platy-clay soils. *Transport in porous media* **57**:251-277.
- Whitaker, S. 1999. *The method of volume averaging*. Kluwer Academic Publishers, Dordrecht.
- Zaoui, A. 1997. *Structural morphology and constitutive behaviour of micro-heterogeneous materials*. Springer, New York.